APPLICATIONS OF RETAINING WALLS FOR SOLVING

GEOTECHNICAL PROBLEMS

Artit Udomchai

A Thesis Submitted in Partial Fulfillment of the Requirements for

the Degree of Doctor of Philosophy of Engineering in Civil

Transportation and Geo-resources Engineering

Suranaree University of Technology

Academic Year 2020

การประยุกต์ใช้กำแพงกันดินในการแก้ปัญหาทางวิศวกรรมปฐพี

นายอาทิตย์ อุดมชัย

APPLICATIONS OF RETAINING WALLS FOR SOLVING

GEOTECHNICAL PROBLEMS

Suranaree University of Technology has approved this thesis submitted in partial fulfillment of the requirements for the Degree of Doctor of Philosophy.

Thesis Examining Committee

_____
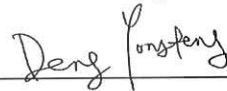
(Prof. Dr. Yongfeng Deng)
Chairperson

_____

(Prof. Dr. Suksun Horpibulsuk)
Member (Thesis Advisor)

_____

(Prof. Dr. Arul Arulrajah)
Member (Thesis Co-Advisor)

_____

(Asst. Prof. Dr. Runglawan Rachan)
Member

_____

(Asst. Prof. Dr. Cherdsak Suksiripattanapong)
Member

_____

(Dr. Apichat Suddeepong)
Member

_____

(Dr. Menglim Hoy)
Member

_____
(Assoc. Prof. Flt. Lt. Dr. Kontorn Chamniprasart)
Vice Rector for Academic Affairs
and Innovation
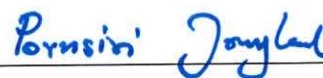
_____
(Assoc. Prof. Dr. Pornsiri Jongkol)
Dean of Institute of Engineering

อาทิตย์ อุดมชัย : การประยุกต์ใช้กำแพงกันดินในการแก้ปัญหาทางวิศวกรรมปฐพี
(APPLICATIONS OF RETAINING WALLS FOR SOLVING GEOTECHNICAL
PROBLEMS) อาจารย์ที่ปรึกษา : ศาสตราจารย์ ดร.สุขสันติ์ หอพิบูลสุข, 185 หน้า.

งานวิจัยนี้ประกอบด้วย 3 บทหลัก บทที่ 3 แสดงการประยุกต์กำแพงกันดินเหล็กเสริมแบก
ทานเป็นท่าเทียบรถบรรทุก ของโรงย่อยถ่านหินในเหมืองแม่เมาะ การไฟฟ้าฝ่ายผลิตประเทศไทย
วัสดุเสริมกำลังที่ใช้ในกำแพงดันดินเป็นชนิดที่ไม่สามารถยืดได้ ที่เรียกว่าเหล็กเสริมแบกทาน ซึ่ง
ประกอบด้วย เหล็กข้ออ้อยเป็นเหล็กตามยาว และเหล็กฉากเป็นเหล็กตามขวาง ความต้านทานแรง
ฉุดเสียดทานของเหล็กเสริมแบกทานคำนวณได้จากแฟคเตอร์หน่วยแรงยึดเกาะ (α) ระหว่างดินกับ
เหล็กเสริม ซึ่งมีค่าลดลงเป็นเชิงเส้นตรงตามปริมาณดินเม็ดละเอียด (F) ความต้านทานแรงฉุดแบก
ทานขึ้นกับระนาบวิบัติของเหล็กตามขวาง (β) และอิทธิพลของการรบกวนของเหล็กตามขวาง
(IF) ปริมาณความชื้นต่อความชื้นเหมาะสม w/w_{OWC} และปริมาณดินเม็ดละเอียด (F) เป็นปัจจัย
สำคัญในการควบคุมทั้ง β และ IF β มีค่าลดลงจาก $\pi/2$ ถึง $\pi/3$ เมื่อ w/w_{OWC} และ F มีค่าเพิ่มขึ้น
นอกจากนี้ ผลการศึกษาพบว่า โซนรบกวนของเหล็กตามขวาง มีขนาดเพิ่มขึ้น เมื่อ w/w_{OWC} และ F
มีค่าลดลง ผลสัมฤทธิ์ของงานวิจัยนี้ คือการพัฒนาสมการทั่วไปสำหรับการคำนวณหาความ
ต้านทานแรงฉุด ในพจน์ของความเค้นในแนวดิ่ง พารามิเตอร์ของกำลังต้านทานแรงเฉือน ปริมาณ
ดินเม็ดละเอียด และปริมาณความชื้น ซึ่งมีประโยชน์อย่างมากในการวิเคราะห์เสถียรภาพภายในของ
กำแพงกันดินเหล็กเสริมแบกทานทั้งก่อนและหลังการก่อสร้าง บทที่ 4 แสดงผลการตรวจวัด
ประสิทธิภาพของกำแพงกันดินเหล็กเสริมแบกทาน หลังสิ้นสุดการก่อสร้างและขณะเปิดใช้งาน
เป็นท่าเทียบรถบรรทุก ในพจน์ของการทรุดตัว ความเค้นในมวลดินทั้งในแนวดิ่งและแนวราบ การ
เคลื่อนตัวด้านข้าง และแรงดึงในเหล็กเสริม ความสัมพันธ์ของสัมประสิทธิ์ความดันดินด้านข้าง
(K) กับความลึก ได้ถูกนำเสนอขึ้นโดยการวิเคราะห์ย้อนกลับของข้อมูลผลตรวจวัดแรงดึงสูงสุดใน
เหล็กเสริม เสถียรภาพภายในของกำแพงกันดินเหล็กเสริมแบกทาน (การต้านทานการฉีกขาดและ
ต้านทานแรงฉุด) ออกสามารถประมาณได้โดยใช้ค่า K และระนาบวิบัติสูงสุดที่นำเสนอ ท้ายสุด
วิธีการออกแบบกำแพงกันดินเหล็กเสริมแบกทานที่ใช้หินเคลย์เป็นดินถมในงานเหมืองได้ถูก
นำเสนอ บทที่ 5 เสนอกรณีศึกษาการวิบัติของกำแพงกันดินป้องกันตลิ่ง ที่บริเวณโค้งน้ำด้านนอก
ของแม่น้ำป่าสัก จังหวัดสระบุรี ประเทศไทย กำแพงนี้ถูกออกแบบและทำการแก้ไขถึง 2 ครั้ง แต่ยัง

มีเสถียรภาพไม่เพียงพอ รวมทั้งยังไม่สามารถทราบสาเหตุของการวิบัติอย่างแน่ชัด งานวิจัยนี้จึงได้ทำการตรวจสอบในสนาม และทำการวิเคราะห์ด้วยไฟไนท์อิลลิเมนต์พร้อมกับเสนอแนวทางการแก้ไข สาเหตุหลักของการวิบัติเกิดจากน้ำจากพื้นที่เกษตรได้ไหลลงสู่แม่น้ำ โดยไหลผ่านเข้าสู่ดินถมด้านหลังของกำแพงกันดินป้องกันตลิ่ง แรงเนื่องจากการซึมผ่านของน้ำส่งผลให้เสถียรภาพของโครงสร้างกันดินลดลง นอกจากนี้ การไหลของกระแสน้ำในแม่น้ำยังกัดเซาะลาดดินธรรมชาติที่ด้านหน้าของกำแพง ส่งผลให้ดินหน้ากำแพงพังทลาย และเกิดการวิบัติของกำแพงในที่สุด การแก้ปัญหาทำโดยการใช้เสาเข็มเจาะร่วมกับวัสดุใยสังเคราะห์และหินทิ้งด้านหน้าเขื่อน โดยวัสดุสังเคราะห์จะทำหน้าที่เป็นระบบระบายน้ำด้านหลังเขื่อน และหินทิ้งจะติดตั้งที่บริเวณหน้าเขื่อนเพื่อป้องกันดินถูกกัดเซาะจากกระแสน้ำ ผลการวิเคราะห์ด้วยไฟไนท์อิลลิเมนต์ แสดงให้เห็นว่าเขื่อนที่ออกแบบมีความปลอดภัย

สาขาวิชาวิศวกรรมโยธา
ปีการศึกษา 2563

ลายมือชื่อนักศึกษา_____
ลายมือชื่ออาจารย์ที่ปรึกษา_____
ลายมือชื่ออาจารย์ที่ปรึกษาร่วม_____

ARTIT UDOMCHAI : APPLICATIONS OF RETAINING WALLS FOR

SOLVING GEOTECHNICAL PROBLEMS. THESIS ADVISOR :

PROF. SUKSUN HORPIBULSUK, Ph.D., 185 PP.

RETAINING WALL/CAUSE OF FAILURE/REMEDIAL APPROACH/ FINITE

ELEMENT/EROSIONS/PLAXIS

This thesis consists of three main chapters. The evaluation of pullout resistance

of the Bearing Reinforcement Earth (BRE) wall as an alternative retaining structure to

support truck ramp for an onsite crusher in the Mae Moh mine, Thailand is presented

in Chapter 3. Bearing reinforcement is an inextensible reinforcement type, which is

manufactured by welding strongly between steel deformed bar (a longitudinal member)

and a set of equal angle steel (transverse member). The pullout friction resistance can

be calculated by utilizing the soil-reinforcement interaction factor, α, which reduced

linearly with fines content (F). The bearing pullout resistance is controlled in the failure

plane during the pullout of a single transverse member (β) and transverse members

interference factor (IF). The water content to optimum water content ratio, w/w_{OWC} and

F are found to be dominant factors controlling both β and IF. The β reduced from $\pi/2$

to $\pi/3$ with the increase in w/w_{OWC} and F. The transverse members interference zone is

larger for lower w/w_{OWC} and F. The significant outcome of this research work is to

inventively develop the generalized pullout resistance equations in terms of normal

stress, shear strength parameters, fine content and water content, which are useful for

the internal stability analysis of BRE walls during and post-construction. Chapter 4

presents the performance of the BRE wall after the end of construction as well as during

The service state was evaluated in terms of settlement, bearing stress, lateral movement, lateral earth pressure and tension force in the reinforcements. The coefficients of lateral earth pressure, K and depth relationship were proposed based on the analysis of measured maximum tensile force in the reinforcements. Using the proposed K and maximum tension plane, the internal stability of the BRE wall which includes factors of safety against rupture and pullout failure was examined. As a result, an effective method of designing the BRE wall with claystone backfill in mining applications was proposed. The case study of a collapsed riverbank protection structure, located in the curvature of the watershed along the Pasak river in Saraburi province, Thailand is presented in Chapter 5. Although efforts have been made to twice rehabilitate this collapsed structure, the rebuilt protection structures were unstable to prevent progressive collapse damage and the cause of their failure remained elusive. This research was engaged to carried out the site investigation and finite element analysis prior to providing the remedial approach on the collapsed structure. This study reveals that the natural disaster events cause seepage forces and soil erosion in the passive zone were the main causes of the structure failure. Based on these two causes of failure, a remedial solution was devised using a new bored pile riverbank protection structure with the usage of geocomposites and ripraps. An adequate factor of safety against the external and internal failure of the new riverbank protection structure was verified by finite element modeling and the results confirmed that the structure was safe.

School of <u>Civil Engineering</u>

Academic Year 2020

Student's Signature _____

Advisor's Signature _____

Co-Advisor's Signature _____

STATEMENT OF ORIGINALITY

This work has not previously been submitted for a degree or diploma in any university. To the best of my knowledge and belief, the thesis contains no material previously published or written by another person except where due reference is made in the thesis itself.

(Signed) _____

Artit Udomchai

ACKNOWLEDGMENTS

Last but not least, I would like to thank my family for their love, comfortable, and supporting me spiritually throughout my Ph.D. studies and my life.

Artit Udomchai

TABLE OF CONTENTS

TABLE OF CONTENT (Continued)

TABLE OF CONTENT (Continued)

TABLE OF CONTENT (Continued)

TABLE OF CONTENT (Continued)

Page

TABLE OF CONTENT (Continued)

Page

APPENDIX

LIST OF FIGURES

LIST OF FIGURES (Continued)

LIST OF FIGURES (Continued)

LIST OF FIGURES (Continued)

LIST OF FIGURES (Continued)

LIST OF TABLES

SYMBOLS AND ABBREVIATIONS

K_o = is at-rest earth pressure coefficient

K_a = is active earth pressure coefficient

K_p = is passive earth pressure coefficient

$K = K_o = \dfrac{\sigma'_{v0}}{\sigma'_h}$ = at-rest earth pressure coefficient

ϕ' = is drained friction angle

γ_d = is actual compacted dry unit weight of the sand behind

the wall

$\gamma_{d(\min)}$ = is dry unit weight of the sand in the loosest state

CD = radius of the failure circle = $\dfrac{\sigma'_o - \sigma'_a}{2}$

q = load per unit length of the surcharge

v = is the velocity of water flow

δ = is the angle of water flow

m = is the weight of the buffering object

c_f = is the stiffness of the wall

K_{air} = 100 kN/m^2 for air under atmospheric pressure

V = velocity of the river flow

SYMBOLS AND ABBREVIATIONS (Continued)

C	=	coefficient of the river flow
g	=	gravity acceleration, (g = 9.81)
s	=	specific gravity of riprap, and
Ω	=	side slope correction factor
ϕ'	=	drained friction angle
$OCR = \dfrac{\sigma'_{vo}}{\sigma'_{y}}$	=	overconsolidation ratio
M	=	material stiffness matrix
E	=	young's modulus
E_{oed}	=	oedometer modulus
ν	=	poisson's ratio
G	=	shear modulus
K	=	bulk modulus
P_w	=	pore water pressure
P_{excess}	=	excess pore pressure
S_u	=	undrained shear strength
σ_v	=	vertical stress
σ_h	=	horizontal stress

CHAPTER I

INTRODUCTION

1.1   Background and problem statement

Retaining wall structures are practically built to support foundation, excavation and stabilize slopes. Retaining wall structures have many types and patterns, which are used depending on construction purposes and/or construction constraints in civil engineering, transportation engineering, geotechnical engineering, and related fields. However, a retaining wall may lose its stability due to various influence factors such as variations in temperature or humidity, material degradation, and load variation. Furthermore, the serious loss of stability leads to collapse of the retaining wall and the surrounding infrastructures.

Therefore, the studies of the stability of retaining walls have been investigated by many researchers. The performance studies of the retaining wall commonly divided into two assessments: external stability and internal stability. The external stability of the retaining wall structure is carried out based on the modes of failure, including sliding, overturning, bearing capacity and deep sated stability failure. While, the internal failure mode deals with in bending moment resistance, shear resistance, axial force resistance and cracking. Generally, the studied influence factor included wall height, wall width, uniform loads, and the cohesion and internal friction angle of the backfill of retaining walls are performed.

Technically, the design of these walls must satisfy two major requirements. First, the wall must have adequate external stability, which means it must remain stable in the desired location (except for small movements required to mobilize the active or passive pressures). Second, it must have sufficient internal stability (or structural integrity), which is able to carry the necessary internal stresses without rupture failure. Walls that have insufficient external stability experience failure in the soil, while those that have insufficient internal stability experience structural failure. These are two separate requirements, and each must be satisfied independently. Extra effort in one does not compensate for a shortcoming in the other. For example, adding more rebar (improving the internal stability) does not compensate for a footing that is too short (a deficiency in external stability) (Coduto, 2011).

The drawback of the retaining wall design can sometimes lead to overdesigned structures that are poorly suited to the local environment (Kondolf et al., 2001). Some stabilization concepts use synthetic or manufactured materials such as walls, mattresses, interlocking blocks hexagonal structures and vegetation and often involve interventions on the site condition (Abbe et al., 2011; Hare, 2008; Tilton, 2003).

To better understand the mechanical performance of these types of walls, the comparison performance features between the predictions using design method in accordance with AASHTO (2014) such as force-based limit-equilibrium methods and empirical-based reinforcement stiffness methods and numerical methods are carried out (Allen et al., 2003, 2004 and Bathurst et al., 2008).

Numerical modeling of mechanical stabilized earth (MSE) walls with hard facings using the finite element method (FEM) has been reported by Bathurst et al. (1992), Cai and Bathurst (1995), and Yoo et al. (2011). The finite difference methods

have been used to model MSE walls with hard and wrapped facings by Hatami and Bathurst (2005, 2006), Huang et al. (2009, 2010), and Yu et al. (2015a, 2015b).

Vijayakumer et al. (2015) analyzed the static stability of retaining walls at Dewarwadi of Belagavi, India. They found that the existing walls were safe but uneconomical and oversized. To save materials, optimal dimensions of retaining walls were proposed.

Liu and Chen (2013) analyzed the stability of a new type of walls with relieving plates by the FEM. The width of the relieving plates influenced the stability of the walls, and a reasonable value of relieving-plate width should be considered in real engineering.

This research presents the innovative development of bearing reinforced earth (BRE) wall as an alternative retaining structure of track ramp support for onsite crusher in Mae Moh mine, Thailand. It demonstrates quick and easy construction technique and consider to be cost-effective construction. The various studied factors in this study, including the wall height, surcharge load, reinforcement vertical spacing, reinforced soil properties, retained/backfill soil properties, and foundation soil properties. The current common design practice of reinforced soil retaining walls, which is based on coherent gravity and lateral earth pressure approach, was used for the analyses. In addition, the case study of the collapsed retaining wall in riverbank Saraburi Province, Thailand is investigated, and the appropriate remedial approach is developed and employed to safely rebuild the retaining wall. Numerical results are compared to the measured data obtained from the site investigation, as well as the behavior of walls in order to confirm the factor of safety of the retaining wall. Finally,

the retaining wall is designed using the AASHTO standard, American Concrete Institute standard (ACI 530) and rebuilt to replace the existed one.

The outcome of this research will lead to the practical design method useful for geotechnical engineers and practitioners.

1.2   Research objectives and scope

The three main objectives of this research are to address as following outlines:

1. To predicting pullout resistance of bearing reinforcement embedded in cohesive-frictional soils.

2. To study the performance of mechanical stabilized earth walls (MSE) for mining application. The performance of the MSE wall included tensile force of reinforcement, lateral movement, and vertical settlement.

3. To analyze the case of failure of a collapsed riverbank protection structure, located in the curvature of the watershed along the Pasak river in Saraburi province, Thailand. The remedial method is also proposed.

1.3   Structure of dissertation

This thesis consists of three main chapters and divides according to the following outlines:

Chapter I is the introduction part that presents the objective and scope of the study.

Chapter II presents the literature review of the recent research papers related to type of retaining walls, lateral earth pressure, surcharge load on retaining wall, water load, basic of finite element analysis, and the aspects of case studies on the retaining wall with the finite element analysis of retaining wall.

Chapter III presents the predicting pullout resistance of bearing reinforcement embedded in cohesive-frictional soils.

Chapter IV presents performance of bearing reinforcement earth walls (BSE) for mining application. The performance of the MSE wall included tensile force of reinforcement, lateral movement, and vertical settlement. This study confirm that BRE wall can be for mining application.

Chapter V presents the case study of a collapsed riverbank protection structure, located in the curvature of the watershed along the Pasak river in Saraburi province, Thailand. Although efforts have been made to twice rehabilitate this collapsed structure, the rebuilt protection structures were unable to prevent progressive collapse damage and the causes of their failure remained elusive. The site investigation and finite element analysis were carried prior to providing the remedial approach on the collapsed structure. A remedial solution was devised using a new bored pile riverbank protection structure with the usage of geocomposites and ripraps. Geocomposites and ripraps were installed at the back and front of the bored pile walls to relieve the structure from seepage forces and to prevent soil erosion, respectively.

Chapter VI concludes the research work, innovative equations useful for the internal stability analysis of bearing reinforcement earth walls during and post-construction as well as provides the suggestion and recommendation on the retaining wall with the finite element analysis of retaining wall.

1.4   References

Abbe, T., Bjork, J., Zehni, A., Park, J., 2011. **New innovative, habitat-creating bank protection method.** In: Proceedings of the 2011 World Environmental and Water Resources Congress 2011: Bearing Knowledge for Sustainability, pp. 2011–2021.

ACI 530, **Building Code Requirements for Masonry Structures.**, 2005 (ACI 530-05/ASCE 5- 05/TMS 402-05), American Concrete Institute, Farmington Hills, MI.

Allen, T.M., Bathurst, R.J., Walters, D.L., Holtz, R.D., Lee, W.F., 2003. **A new working stress method for prediction of reinforcement loads in geosynthetic walls.** Can. Geotech. J. 40 (5), 976-994.

Allen, T.M., Bathurst, R.J., Holtz, R.D., Lee, W.F., Walters, D.L., 2004. **A new working stress method for prediction of loads in steel reinforced soil walls.** ASCE J. Geotech. Geoenvironmental Eng. 130 (11), 1109 -1120.

American Association of State Highway and Transportation Officials (AASHTO), 2014. **LRFD Bridge Design Speci fi cations, seventh ed.** Washington, DC.

Bathurst, R.J., Karpurapu, R.G., Jarrett, P.M., 1992. **Finite element analysis of a geo-grid reinforced soil wall.** In: Borden, Holtz, Juran (Eds.), Grouting, Soil Improvement and Geosynthetics, vol. 2. ASCE Geotechnical Special Publication No. 30, pp. 1213-1224.

Cai, Z., Bathurst, R.J., 1995. **Seismic response analysis of geosynthetic reinforced soil segmental retaining walls by finite element method.** Comput. Geotech. 17 (4), 523-546 .

Coduto, D. P., 2011. **Foundation design: principles and practices,** Prentice Hall, New Jersey.

Hare, M.E., 2008. **Stream restoration and channel repair.** Eros. Control 15 (May (3)), 36–45, 9p.

Hatami, K., Bathurst, R.J., 2005. **Development and verification of a numerical model for the analysis of geosynthetic reinforced soil segmental walls under working stress conditions.** Can. Geotech. J. 42 (4), 1066-1085.

Hatami, K., Bathurst, R.J., 2006. **Numerical model for reinforced soil segmental walls under surcharge loading.** ASCE J. Geotech. Geoenvironmental Eng. 132 (6), 673-684.

Huang, B., Bathurst, R.J., Hatami, K., 2009. **Numerical study of reinforced soil segmental walls using three different constitutive soil models.** ASCE J. Geotech. Geoenvironmental Eng. 135 (10), 1486-1498.

Huang, B., Bathurst, R.J., Hatami, K., Allen, T.M., 2010. **In fluence of toe restraint on reinforced soil segmental walls.** Can. Geotech. J. 47 (8), 885-904.

S. Vijayakumer, A. B. Subhash, T. P. Sumant, M. B. Venkatesh, and L. K. Yallappa, **"A case study on statics ability analysis of retaining wall at dewarwadi,"** International Journal of Innovative Research in Science, Engineering and Technology,vol.4,pp. 2319-8753, 2015.

Yoo, C., Jang, Y.S., Park , I.J., 2011. **Internal stability of geosynthetic-reinforced soil walls in tiered configuration.** Geosynth. Int. 18 (2), 74-83.

CHAPTER II

LITERATURE REVIEW

2.1 TYPE OF RETAINING WALLS

The type of retaining wall is practically selected based on many important factors including desing loading, soil profile and geograhy, environmental issues, constructibiltiy and constraints of the site, and cost of construction and maintenance.

2.1.1 Rigid gravity and semi-gravity walls

Rigid gravity walls is often built of sandstone masonry, unreinforced concrete, or reinforced concrete (Coduto, 2001). Rigid gravity walls are also used in earth applications such as cut and fill works. These walls have comparatively tight base widths and notused once the deep foundations are required. The rigid gravity walls are considerd as economical with low wall heights.

Semi-gravity cantilever, counterfort and buttress walls (Figure 2.1) are built using reinforced concrete with the narrow based-widths. These walls might be used for cut and fill works. These walls can be constructed using either shallow or deep foundations. They can be used as sound barrier walls, traffic and roadway sign structures. These walls are used for supporting drainage constructions and utilities and span existing drainage structures and load sensitiveutilities. They are the most economical at low to medium barrier heights.

As the gravity walls and semi-gravity walls are rigid and heavy weight, they might be suitable for the construction site, whereby the foundations can be constructed to limit the totally and partially settlements within appropriate values.

Figure 2.1 Typical semi-gravity retaining walls

2.1.2 Non-gravity cantilevered walls

Non-gravity cantilevered walls (Figure 2.2) are constructed of vertical structural members consisting of partially embedded soldier piles or continuous sheet piles. Soldier piles may be constructed with driven steel piles, treated timber, precast concrete or steel piles placed in drilled holes and backfilled with concrete or cast-in-place reinforced concrete. Continuous sheet piles may be constructed with driven precast prestressed concrete sheet piles or steel sheet piles. Soldier piles are faced with either treated timber, reinforced shotcrete, reinforced cast-inplace concrete, precast concrete or metal elements.

This type wall is suitable for both cut and fill applications but is the most suitable for cut applications. Because of the narrow base width of this type wall, it is suitable for situations with tight space constraints or right of way constrain.

Figure 2.2 Typical Non-gravity cantilevered retaining walls

2.1.3 Anchored walls

Anchored walls (Figure 2.3) are commonly constituted of similar components as non-gravity cantilevered walls but acquire further horizontal resistance from one or more levels of anchors. The anchors can be ground anchors (tiebacks) comprising of bored holes with prestressing steel tendons expanding from the wall face to an anchor area placed behind possible failure planes in the preserved earth weight. The structural anchors are comprised of ground anchors, reinforced concrete anchors or driven vertical pile anchors. They are applicable for circumstances involving one or more quantities of anchors when the anchors tie rods are restricted

conditions compelling a specific level of anchors. The ground anchor tendons and tie rods are supplied with deterioration shield. The group of driven piles contains the tattered compressive piles and vertical tension piles linked with a reinforced concrete cap. They are located behind possible failure planes within the retained soil and are constructed to the wall by horizontal tie rods.

The circulation of horizontal earth-pressure on anchored walls is affected by the structure and process of wall construction and the anchor pre-stressing. Ground anchors are usually pre-stressed to a high rate of their design tension force whereas anchors with tie rods are attached to the wall with small prestress force.

Anchored walls are normally built in cut conditions where construction proceeds from the top-down to the base of the wall. For situations where fill is placed behind the wall, special consideration in the design and construction is required to protect the ground anchors failure from construction damage due to fill placement and fill settlement.

The vertical wall elements should extend below potential failure plane associated with the retained soil or rock mass. The stable foundation material is located at the base of the wall face, and only minimal embedment of the wall may be required (soldier pileless design).

The prolonged creep behavior of the anchors is taken into design. Anchors are avoid to be located in soft soil layer. Anchored walls are used to improve unstable soil conditions. Providing groundwork material occurs at the location for the anchors, economical wall heights up to 20 m.

Figure 2.3 Typical semi-gravity retaining wall

2.1.4 Mechanically stabilized earth walls

Mechanically stabilized earth (MSE) walls (Figure 2.4) use both steel or geosynthetic reinforced soil materials, and upright or near vertical facing components. MSE walls act as a gravity wall, taking the horizontal force throughout the dead load of the reinforced soil mass behind the facing.

MSE walls are typically utilized where conventional reinforced concrete retaining walls are not considered, which are particularly well suited for sites where substantial total and differential settlements are expected. The acceptable differential displacement is limited by the deformability of the wall facing elements within the plane of the wall face. In the case of precast concrete panels, deformablitiy is relied on the panel size and shape and the width of the joints between

panels. These wall also use in the application of cut and fill works. As its base width is greater than that of conventional reinforced concrete walls, they are the most cost effective in fill applications.

MSE walls are not practical used where floodplain erosion or scour may weaken the reinforced soil weight or the wall is constructed at sufficient depth or adequate scour protection is required to avoid the erosion or scour. MSE walls are not suitable for supporting bridge abutments with shallow foundations or pile supported bridge abutments where seismic movements of the abutment may impose enormous load on the wall face panels and the soil reinforcement to face panel connections. MSE walls are used in front of pile supported bridge abutments where the seismic forces from the bridge super structure are limited by elastomeric bearing pads supporting the bridge super structure. These limited seismic forces shall be considered in the design of the MSE wall. The design service life shall be approximately 75 years for MSE walls in front of pile supported bridge abutments.

MSE walls are not recommended to use with aggressive environmental conditions unless environment specific studies of the long-term corrosion or degradation of the soil reinforcement are conducted.

MSE walls with steel reinforced soil might be applicable when defrosting salts are used if an impervious cap is constructed at the ground surface above the soil reinforcement and adequate control of surface run off is provided

Figure 2.4 Typical semi-gravity retaining walls

2.1.5 Prefabricated modular walls

Prefabricated sectional walls (Figure 2.5) use stacked or interconnected structural elements with backfill to withstand earth pressures by acting as gravity retaining walls. Structural components comprising of preserved timber, or precast reinforced concrete are used to form a cellular system. In addition, the backfill is constructed as a crib wall or steel segments are bolted together to form a similar system to construct a bin wall. Rock filled wire gabion baskets are used to construct a gabion wall. Solid precast concrete units or segmental concrete masonry units are stacked to form a gravity block wall.

Prefabricated modular walls may be used where conventional reinforced concrete walls are not considered. Steel modular systems shall not be used where aggressive industrial pollutants or other environmental conditions such as use of deicing salts or cathodic protection of nearby pipelines are present at a given site.

The aesthetic appearance of some of these type walls is governed by the nature of the structural elements used. Those elements consisting of precast concrete, may incorporate various aesthetic treatments. This type wall is most economical for low to medium height walls.
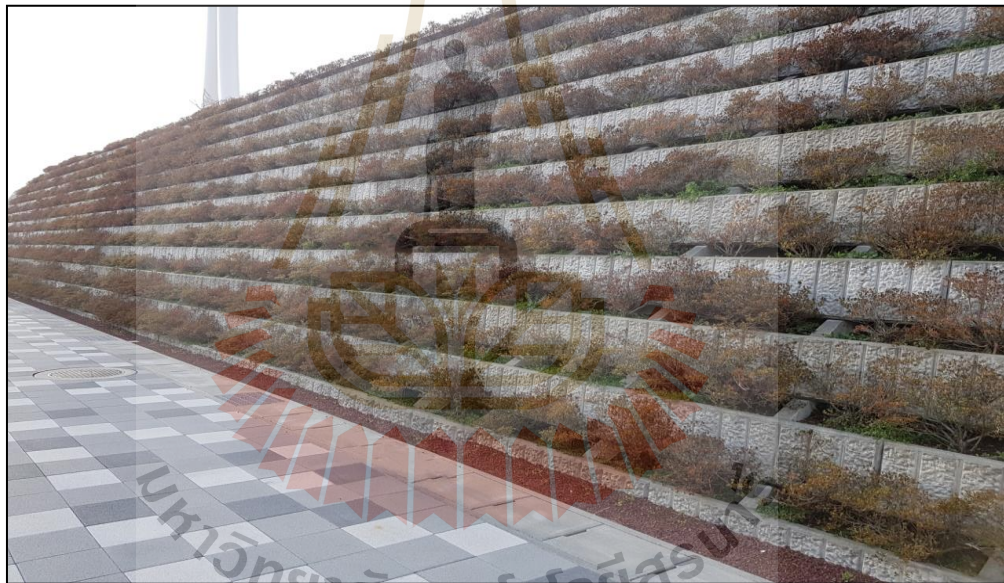
Figure 2.5 Typical prefabricated modular walls

2.2 EARTH PRESSURE

The loads governing the design of retaining wall arise primarily from the soil and water surrounding the wall and from other influences such as surface surcharges and external loads applied directly to the piling. Current methodologies for evaluating these loads are discussed in the following paragraphs.

2.2.1 Lateral Earth pressures

Retaining walls such as rigid gravity walls, cantilevered walls, anchored walls, MSE walls and pre-fabricated modular walls are generally constructed in foundation suitable. Suitable design and construction of the wall structures require a comprehensive understanding of the lateral forces that act between the structures and soil masses. These lateral forces are caused by lateral earth pressure. This chapter aims to review the various earth pressure theories.

Earth pressures reflect the state of stress in the soil mass. The concept of an earth pressure coefficient, K is often used to describe this state of stress (Budhu, 2000). The earth pressure coefficient is defined as the ratio of horizontal stresses to the vertical stresses at any depth below the soil surface:

$$K = \frac{\sigma_h}{\sigma_v} \qquad (2.1)$$

Earth pressures for any given soil-structure system have 3 types of the following from: an initial state of stress referred to as at-rest, a minimum limit state referred to as active, or a maximum limit state referred to as passive.
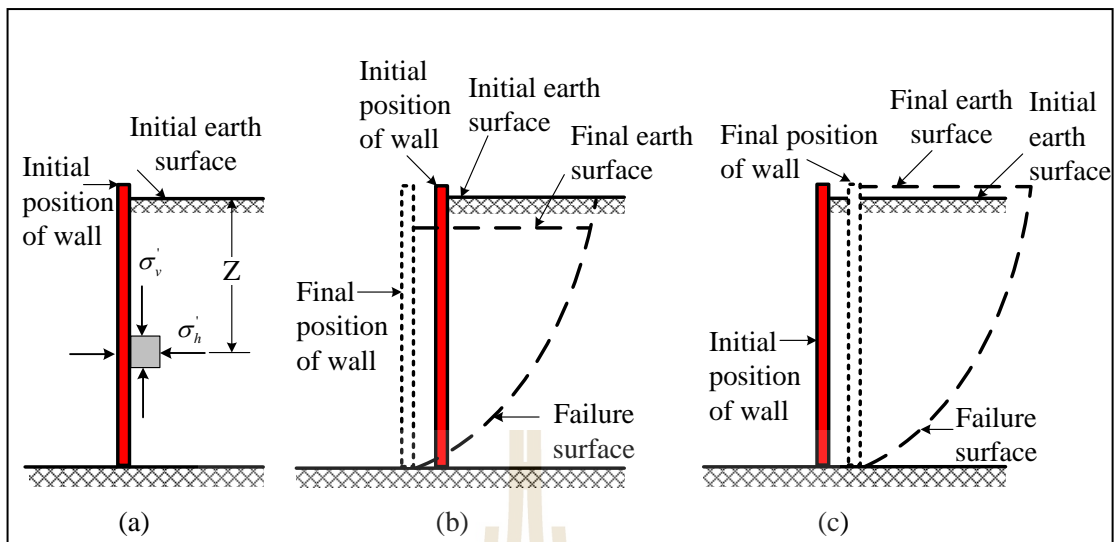
Figure 2.6 Definition of at-rest, active, and passive pressures

a. At-rest pressures: At-rest pressure refers to a state of stress where there is no lateral movement or strain in the soil mass. In this case, the lateral earth pressures are those that are existed in the ground prior to installation of a wall (Brooker, 1965). This state of stress is shown in Figure 2.6a or Eq. 2.2

$$K = K_o = \frac{\sigma'_{v0}}{\sigma'_h} \qquad (2.2)$$

Where

K_0 is at-rest earth pressure coefficient

b. Active pressures: Active soil pressure is the minimum possible value of horizontal earth pressure at any depth. This pressure develops when the walls move or rotate away from the soil allowing the soil to expand horizontally in

the direction of wall movement. The state of stress resulting in active pressures is shown in Figure 2.6b or Eq. 2.3

$$K = K_a = \frac{\sigma'_h}{\sigma'_{v0}} = \frac{\sigma'_a}{\sigma'_{v0}}$$ (2.3)

Where

K_a is active earth pressure coefficient.

c. Passive pressures: Passive (soil) pressure is the maximum possible horizontal pressure that can be developed at any depth from a wall moving or rotating toward the soil and tending to compress the soil horizontally. The state of stress resulting in passive pres-sures is shown in Figure 2.6c or Eq. 2.4

$$K = K_p = \frac{\sigma'_h}{\sigma'_{v0}} = \frac{\sigma'_p}{\sigma'_{v0}}$$ (2.4)

Where

K_p is passive earth pressure coefficient.

Figure 2.7 shows the nature of variation of lateral earth pressure with the wall tilt. Typical values of $\Delta L_a / H$ and $\Delta L_p / H$ for attaining the active and passive states in various soils are given in Table 2.1
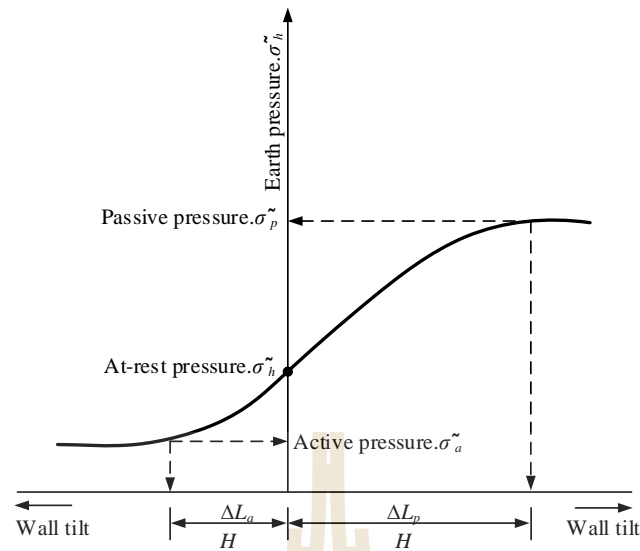
Figure 2.7 Variation of the magnitude of lateral earth pressure with wall tilt

Table 2.1 Typical Values of $\Delta L_a/H$ and $\Delta L_p/H$

Soil type	$\Delta L_a/H$	$\Delta L_p/H$
Loose sand	0.001-0.002	0.01
Dense sand	0.0005-0.001	0.005
Soft clay	0.02	0.04
Stiff clay	0.01	0.02

2.2.2 Earth pressure at rest

The fundamental concept of earth pressure at rest was discussed in the previous part. In order to define the earth pressure coefficient K_o at rest, we refer to Figure 2.8, which shows the wall retaining a dry soil with a unit weight of γ. The wall is static (Das, 1987, 1994). At a depth z, where vertical effective stress $\sigma'_0 = \gamma z$ the horizontal effective stress : $\sigma'_h = K_o \gamma z$.

$$K_o = \frac{\sigma'_h}{\sigma'_{vo}} = \text{at-rest earth pressure coefficient}$$

For coarse-grained soils, the coefficient of earth pressure at rest can be approximated by using the empirical relationship (Jaky, 1944)

$$K_o = 1 - \sin\phi' \qquad (2.5)$$

Where ϕ' is drained friction angle

When designing a wall under the lateral earth pressure at rest, it must consider of estimating the value of K_o. Sherifret al. (1984) conducted laboratory tests and indicated that Jaky's equation for K_o (Eq.2.5) provides reasonable results for loose sand backfill material. However, for dense sand backfill, Eq. (2.6) might grossly underestimate the lateral earth pressure at rest. This is due to the resulted from the process of soil compaction. Hence, the recommendation for the design can be found as follows:

$$K_o = (1 - \sin\phi) + \left[\frac{\gamma_d}{\gamma_{d(\min)}} - 1\right]5.5 \qquad (2.6)$$

Where

γ_d is actual compacted dry unit weight of the sand behind the wall

$\gamma_{d(\min)}$ is dry unit weight of the sand in the loosest state
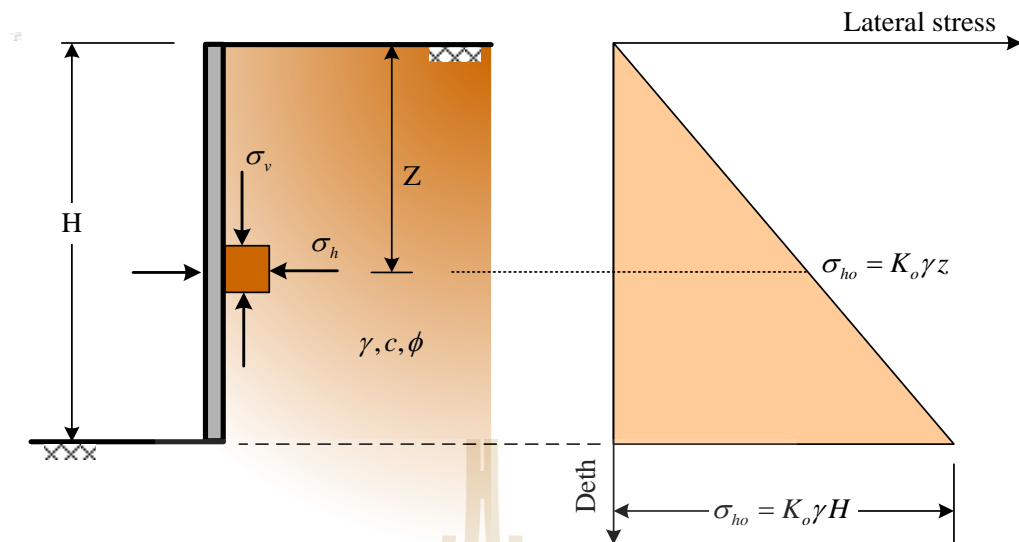
Figure 2.8 Earth pressure at rest

For fine grained, normally consolidated soils, Massarsch (1979) suggested the following equation for K_o,

$$K_o = 0.44 + 0.42 \left[\frac{PI(\%)}{100} \right] \tag{2.7}$$

For overconsolidated clays, the coefficient of earth pressure at rest can be approximated as

$$K_{o(overconsolidated)} = K_{o(normally\ consolidated)} \sqrt{OCR} \tag{2.8}$$

Where OCR is overconsolidation ratio

The overconsolidation ratio is defined as

$$OCR = \frac{\sigma'_{vo}}{\sigma'_{y}} \tag{2.9}$$

Figure 2.8 shows the distribution of lateral earth pressure at rest on a wall of height H retaining a dry soil having a unit weight of γ. The total force per unit length of the wall, P_o is equal to the area of the pressure diagram, so

$$P_o = \frac{1}{2} K_o \gamma H \tag{12.10}$$

2.2.3 Earth pressure at rest for partially submerged soil

Figure 2.9a indicates a wall of height H. The groundwater table is at a depth H_1 below the ground surface, and there is no compensating water on the other side of the wall. For $z \leq H_1$, the lateral earth pressure at rest can be given as $\sigma'_h = K_o \gamma z$. The difference of σ'_h with depth is given by triangle ACE in Figure 2.9a. However, for $z \leq H_1$ (i.e., below the groundwater table), the pressure on the wall is found from the effective stress and pore water pressure components via the equation

$$\sigma'_{vo} = \gamma H + \gamma' (z - H_1) \tag{2.11}$$

Where

$$\gamma' = \gamma_{sat} - \gamma_w \tag{2.12}$$

So the effective lateral pressure at rest is

$$\sigma_h' = K_o \sigma_v' = K_o \left[\gamma H_1 + \gamma(z - H_1) \right] \tag{2.13}$$

The variation of σ_h' with depth is shown by CEG B in Figure 2.9a. Again the lateral pressure from pore water is

$$u = \gamma_w \left(z - H_1 \right) \tag{2.14}$$

The variation of a with depth is shown in Figure 2.9b

Hence, the total lateral pressure from earth and water at any depth $z \geq H_1$, is equal to

$$\sigma_h = \sigma_h + u$$

$$= K_o \left[\gamma H_1 + \gamma'(z - H_1) \right] + \gamma_w (z - H_1) \tag{2.15}$$

The force per unit length of the wall can be found from the sum of the areas of the pressure diagrams in Figures 2.9a and 2.9b and is equal to (Figure 2.9c)

$$P_o = \tfrac{1}{2} K_o \gamma H_1^2 + K_o \gamma H_1 H_2 + \tfrac{1}{2} \left(K_o \gamma' + \gamma_w \right) H_2^2 \tag{2.16}$$
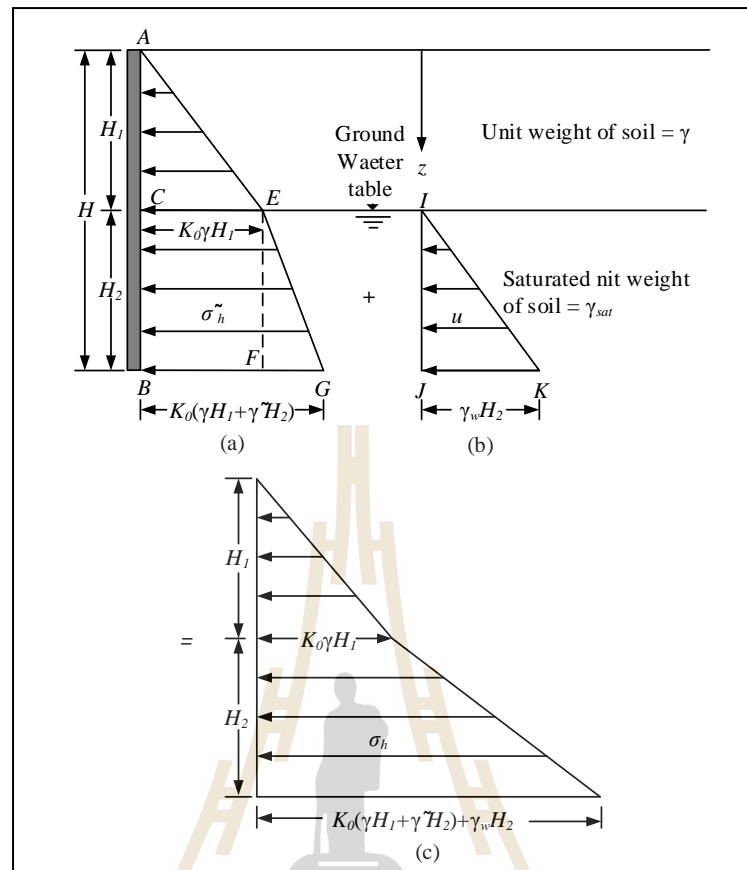
Figure 2.9 Distribution of earth pressure at rest for partially submerged soil

2.2.4   Rankine's theory of active pressure

The phrase plastic equilibrium in soil refers to the condition where every point in a soil mass is on the verge of failure. Rankine (1857) investigated the stress conditionsin soil at a state of plastic equilibrium.
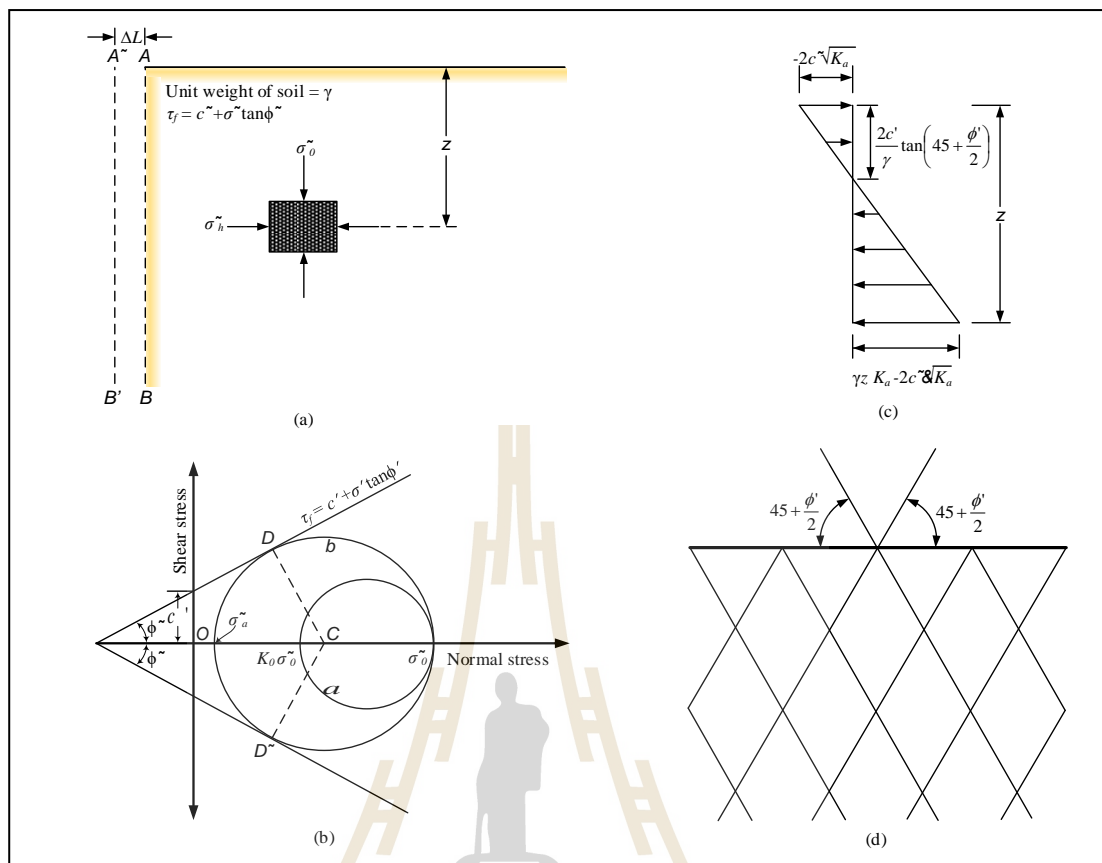
Figure 2.10 Rankine's active earth pressure

Figure 2.10a shows a soil mass that is bounded by a frictionless wall, AB, that extends to an infinite depth. The vertical and horizontal effective principal stresses on a soil element at a depth z are σ'_o and σ'_h, respectively. If the wall AB is not allowed to move, then $\sigma'_h = k_o \sigma'_o$. The stress condition in the soil element can be represented by the Mohr's circle a in Figure 2.10b. However, if the wall AB is allowed to moveaway from the soil mass gradually, The horizontalprincipal stress wil l decrease. Ultim lately a state will be reached when the resscondition in the soil ele- ment can be represented by the circle b, the state of plastic quilibrium, and failure of the soil will occur. This situation represents Rankine's active state, and the

effective pressure σ'_a on the vertical plane (which is a principal plane) is Rankine's

active earth pressure. We next derive σ'_a in terms of γ, z, c', and ϕ' from Figure

2.10b

$$\sin\phi' = \frac{CD}{AC} = \frac{CD}{AO+OC}$$

Chapter 12 Lateral Earth Pressure: At-Rest, Rankine, and Coulomb

But

$$CD = radius \ of \ the \ failure \ circel = \frac{\sigma'_o - \sigma'_a}{2}$$
$$AO = c' \cot\phi'$$

And

$$OC = \frac{\sigma'_o + \sigma'_a}{2}$$

So

$$\sin\phi' = \frac{\dfrac{\sigma'_o - \sigma'_a}{2}}{c' \cot\phi' + \dfrac{\sigma'_o + \sigma'_a}{2}}$$

Or

$$c' \cos\phi' + \frac{\sigma'_o + \sigma'_a}{2}\sin\phi' = \frac{\cos\phi'}{1+\sin\phi'}$$

Or

$$\sigma_a^{'} = \sigma_o^{'} \frac{1 - \sin\phi^{'}}{1 + \sin\phi^{'}} - 2c^{'} \frac{\cos\phi^{'}}{1 + \sin\phi^{'}} \qquad (2.17)$$

But

$\sigma_a^{'}$ = vertical effective overburden pressure = γz

$$\frac{1 - \sin\phi^{'}}{1 + \sin\phi^{'}} = \tan^2\left(45 - \frac{\phi^{'}}{2}\right)$$

And

$$\frac{\cos\phi^{'}}{1 + \sin\phi^{'}} = \tan\left(45 - \frac{\phi^{'}}{2}\right)$$

Substituting the preceding values into Eq. (2.17), we get

$$\sigma_a^{'} = \gamma z \tan^2\left(45 - \frac{\phi^{'}}{2}\right) - 2c^{'} \tan\left(45 - \frac{\phi^{'}}{2}\right) \qquad (2.18)$$

The variation of $\sigma_a^{'}$ with depth is shown in Figure 2.10c. For cohesionless soils, $c^{'} = 0$ and

$$\sigma_a^{'} = \sigma_o^{'} \tan^2\left(45 - \frac{\phi^{'}}{2}\right) \qquad (2.19)$$

The ratio of σ'_a to σ'_o is called the coefficient of Rankine's active earth pressure and is given by

$$K_a = \frac{\sigma'_a}{\sigma'_o} = \tan^2\left(45 - \frac{\phi'}{2}\right) \tag{2.20}$$

Again, from Figure 2.10b, it is seen that the failure planes in the soil make $\pm(45 + \phi,/2)$ degree angles with the direction of the major principal plane that is, the horizontal. These are called potential slip planes and are shown in Figure 2.10d.

It is important to realize that a similar equation for σ_a could be derived based on the total stress shear strength parameters - that is, $\tau_f = c + \sigma \tan\phi$. For this case,

$$\sigma_a = \gamma z \tan\left(45 - \frac{\phi}{2}\right) - 2c \tan\left(45 - \frac{\phi}{2}\right) \tag{2.21}$$

2.2.5   Rankine's theory of passive pressure

Rankine's passive statee can be explained with the aid of Figure 2.11 A B is a frictionless wall that extends to an infinite depth (Figure 2.11a). The initial stress condition on a soil element is represented by the Mohr's circle a in Figure 2.11b. When the wall is gradually pushed in to the soil mass, the effective principal stress σ'_h will increase. Ultimately, the wall will attain a situation where the stress condition for the soil element can be expressed by the Mohr's circle b. At this time, failure of the soil will occur. This situation is referred to as Rankine's passive state. The lateral

earth pressure $\sigma_p^{'}$ which is the major principal stress, is called Rankine's passive earth pressure. From figure 2.11b, it be shown that

$$\sigma_p^{'} = \sigma_o^{'} \tan^2\left(45 - \frac{\phi^{'}}{2}\right) + 2c^{'} \tan\left(45 - \frac{\phi^{'}}{2}\right)$$

$$= \gamma z \tan^2\left(45 - \frac{\phi^{'}}{2}\right) + 2c^{'} \tan\left(45 - \frac{\phi^{'}}{2}\right) \tag{2.22}$$

The derivation is like that for Rankine's active state.

Figure 2.10 illustrates the difference of passive pressure with depth. For cohesion-less soils $\left(c^{'} = 0\right)$,

$$\sigma_p^{'} = \sigma_o^{'} \tan^2\left(45 + \frac{\phi^{'}}{2}\right)$$

Or

$$\frac{\sigma_p^{'}}{\sigma_o^{'}} = K_p = \tan^2\left(45 + \frac{\phi^{'}}{2}\right) \tag{2.23}$$

K_p (the ratio of effective stresses) in the preceding equation is referred to as the coefficient of Rankine's passive earth pressure.
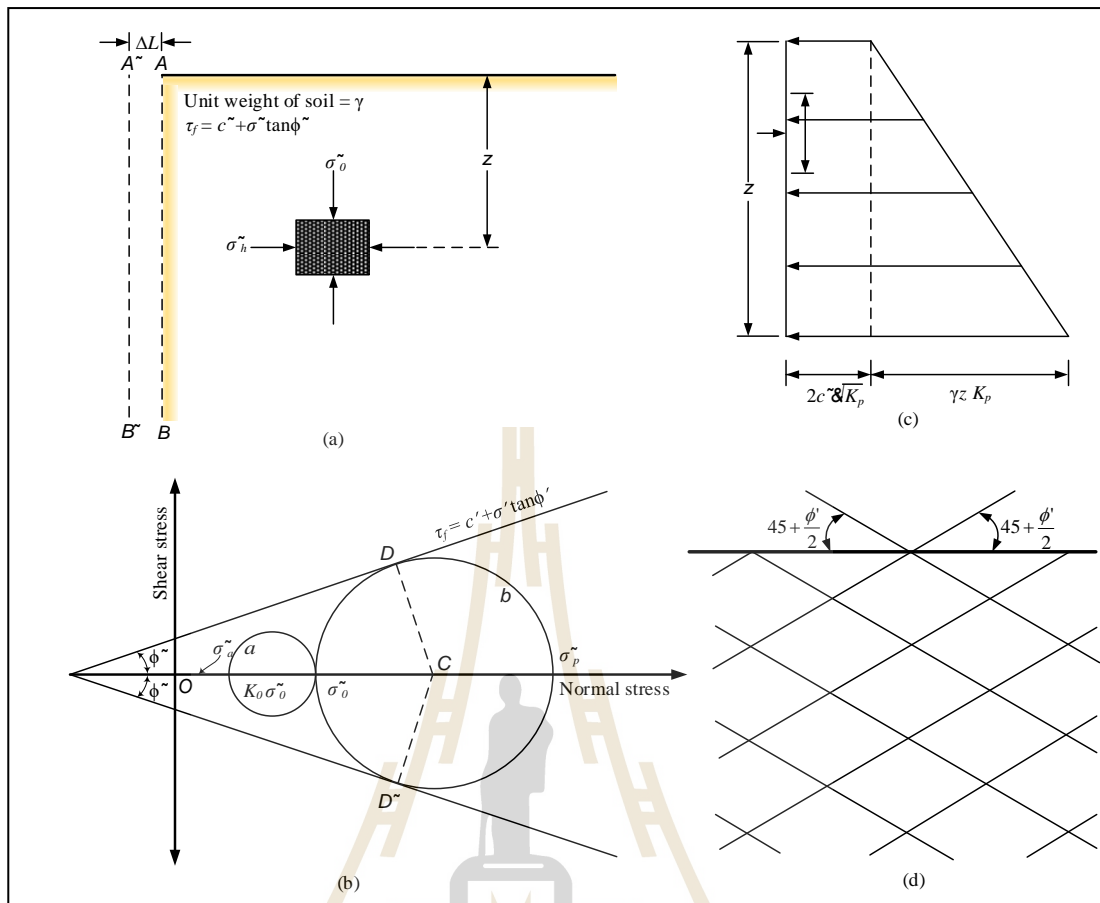
Figure 2.11 Rankine's passive earth pressure

The points D and D' on the failure circle (see Figure 2.11b) directly relate to the slip planes in the soil. For Rankine's passive state, the slip planes make $\pm(45+\phi/2)$ - degree angles with the direction of the minor principal plane - that is, in the horizontal direction. Figure 2.11d indicates the distribution of slip planes in the soil mass.

2.2.6 Rankine active and passive pressure with sloping backfill

In Sections 2.3.4 through 2.3.5, the retaining walls with vertical and horizontal backfills are considered. In some cases, however, the backfill may be continuously sloping at an angle a with the horizontal as shown in Figure 2.12 for

active pressure case. In such cases, the direction of Rankine's active or passive pressures is no longer horizontal. Furthermore, they are inclined at an angle a with the horizontal. If the backfill is a granular soil with a drained friction angle ϕ', and $c' = 0$, then

$$\sigma'_a = \gamma z K_a \tag{2.24a}$$

Where

$$K_a = \cos\alpha \frac{\cos\alpha - \sqrt{\cos^2\alpha - \cos^2\phi'}}{\cos\alpha + \sqrt{\cos^2\alpha - \cos^2\phi'}} \tag{2.24b}$$

The active force per unit length of the wall can be given as

$$P_a = \frac{1}{2}K_a\gamma H^2 \tag{2.25}$$

The line of action of the resultant acts at a distance of H/3 measured from the bottom of the wall.

Similarly, the Rankine passive earth pressure for a wall of height H with a granular sloping backfill can be represented by the expression

$$P_p = \frac{1}{2}\gamma H^2 K_p \tag{2.26}$$

Where

$$K_p = \cos\alpha \frac{\cos\alpha + \sqrt{\cos^2\alpha - \cos^2\phi'}}{\cos\alpha - \sqrt{\cos^2\alpha - \cos^2\phi'}} \qquad (2.27)$$

is the passive earth pressure coefficient.

For the active force case, the resultant force P_P is decreased at an angle with the horizontal and intersects the wall at a distance of H/3 determined from the bottom of the wall.
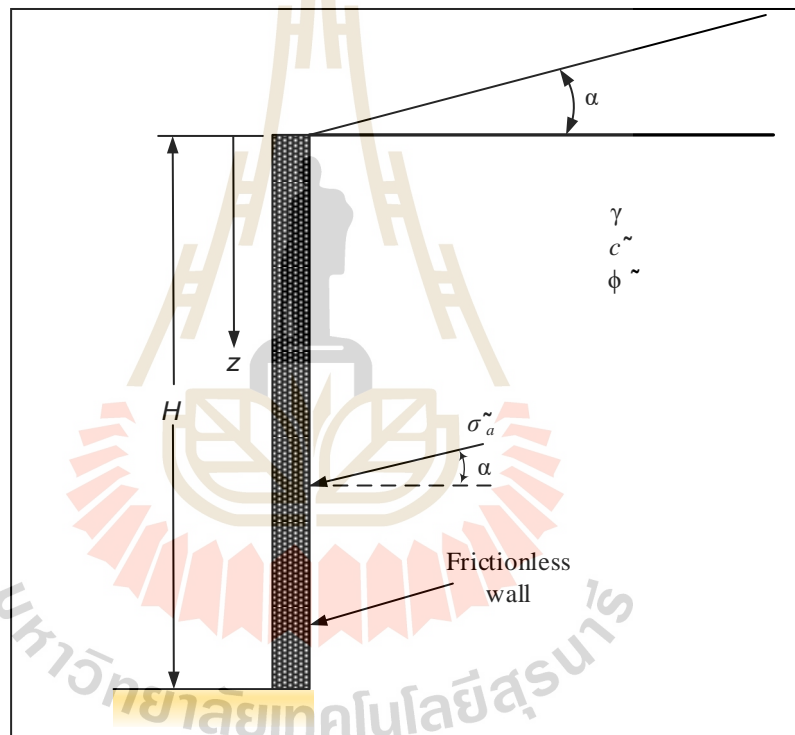
Figure 2.12 Frictionless vertical retaining wall with sloping backfill

COULOMB'S EARTH PRESSURE THEORY

Since 200 years ago, Coulomb (1776) presented a concept for active and passive earth pressures against retaining walls. In this theory, Coulomb presumed that the failure surface is a plane. The wall friction was taken into consideration. The

following sections discuss the general principles of the derivation of Coulomb's earth pressure theory for a cohesionless backfill (shears trength defined by the equation $T_f = \sigma' \tan \phi'$).

2.2.7 Coulomb's Active Pressure

Let *AB* (Figure 2.13a) be the back face of a wall supporting agranular soil, the surface of which is constantly sloping at an angle a with the horizontal. BC is a trial failure surface. In the stability consideration of the probable failure wedge ABC, the following forces are involved (per unit length of the wall):
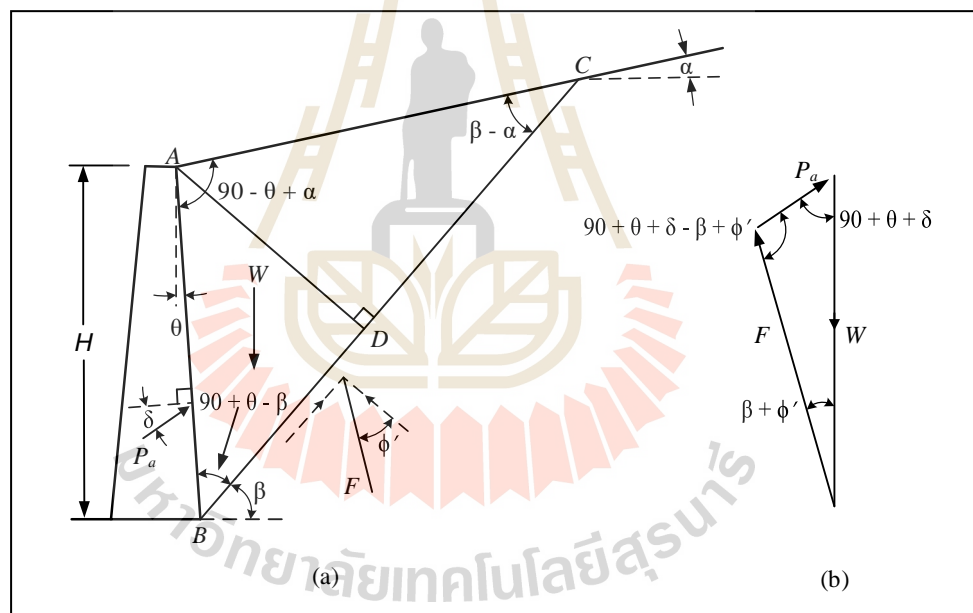
Figure 2.13 Coulomb's active pressure: (a) trial failure wedge, (b) force polygon

l. *W*, the weight of the soil wedge.

2. *F*, the resultant of the shear and normal forces on the surface of failure. BC. This is inclined at an angle of ϕ to the normal drawn to the plane BC.

3. P_a, the active force per unit length o1'the wall. The direction of P_a is inclined a tan angle δ to the normal drawn to the face of the wall that supports the soil. δ is the angle of friction between the soil and the wall.

The force triangle for the wedge is shown in Figure 2.13b. From the law of sines, we have

$$\frac{W}{\sin(90+\theta+\delta-\beta+\phi')} = \frac{P_a}{\sin(\beta-\phi')} \tag{2.28}$$

Or

$$P_a = \frac{\sin(\beta-\phi')}{\sin(90+\theta+\delta-\beta+\phi')}W \tag{2.29}$$

The preceding equation can be written in the form

$$P_a = \frac{1}{2}\gamma H^2[\frac{\cos(\theta-\beta)\cos(\theta-a)\sin(\beta-\phi')}{\cos^2\theta\sin(\beta-a)\sin(90+\theta+\delta+\phi')}] \tag{2.30}$$

where γ = unit weight of the backfill. The values of γ, H, θ, a, ϕ', and δ are constants, and β is the only variable. To determine the critical value of β for maximum P_a, we have

$$\frac{dP_a}{d\beta} = 0 \tag{2.31}$$

After solving Eq. (2.31), when the relationship of β is substituted into Eq. (2.30), we obtain Coulomb's active earth pressure as

$$P_a = \frac{1}{2} K_a \gamma H^2 \tag{2.32}$$

where K_a is Coulomb's active earth pressure coefficient and is given by

$$K_a = \frac{\cos^2(\phi'-\theta)}{\cos^2\theta\cos(\delta+0)\left[1+\sqrt{\dfrac{\sin(\delta+\phi')\sin(\phi'-a)}{\cos(\delta+\theta)\cos(\theta-a)}}\right]^2} \tag{2.33}$$

Note that when $a=0°$, $\theta=0°$ and $\delta=0°$, Coulomb's active earth pressure coefficient be comes equal to $(1-\sin\phi')/(1+\sin\phi')$, which is the same as Rankine's earth pressure coefficient given earlier in this chapter.

2.2.8 Coulomb's passive pressure

Figure 2.14a shows a retaining wall with a sloping cohensionless backfill like that illustration in Figure 2.13a. The force polygon for equilibrium of the wedge *ABC* for the passive state is shown in Figure 2.14b. P_p represents the passive force. Other notations used are the same as that for the active case (Section 2.10). In a simiral procedure the active case [Eq. (2.32)],

$$P_p = \frac{1}{2} K_p \gamma H^2 \tag{2.34}$$

Where

$\quad K_p \quad$ is Coulomb's passive earth pressure coefficient, or

$$K_p = \frac{\cos^2(\phi' - \theta)}{\cos^2\theta \cos(\delta + \theta)\left[1 - \sqrt{\dfrac{\sin(\phi' - \delta)\sin(\phi' + \alpha)}{\cos(\delta - \theta)\cos(\alpha + \theta)}}\right]^2} \qquad (2.35)$$

For a frictionless wall with the vertical back face supporting granular soil backfill with a horizontal surface (that is, $\theta = 0°$, $\alpha = 0°$, and $\delta = 0°$), Eq.(2.35)

$$K_p = \frac{1 + \sin\phi'}{1 - \sin\phi'} = \tan^2(45 + \frac{\phi'}{2}) \qquad (2.36)$$
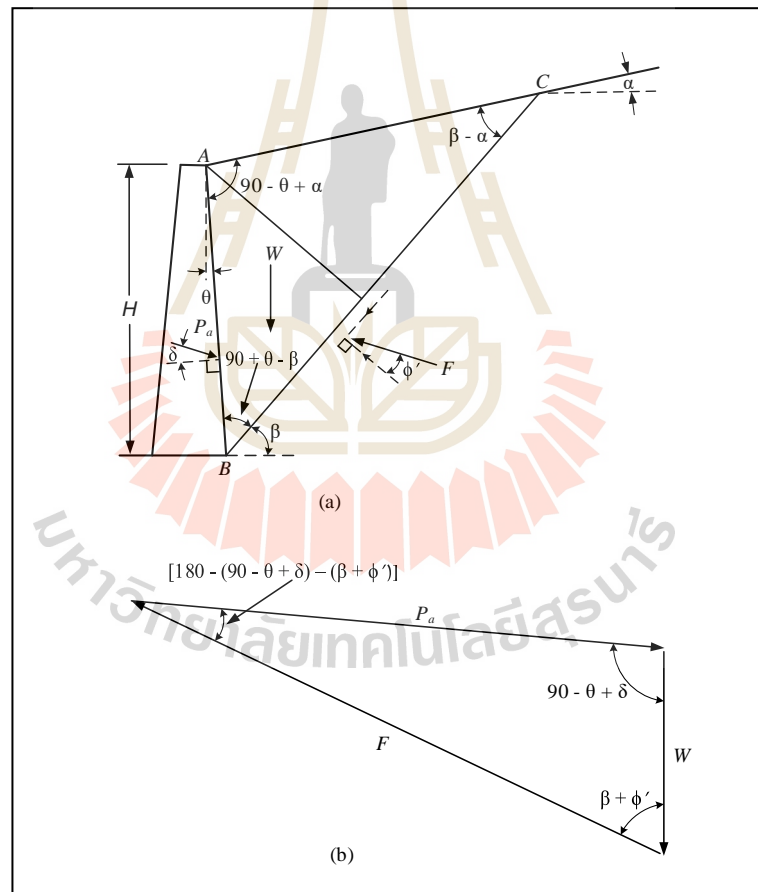
Figure 2.14 Coulomb's passive pressure: (a) trial failure wedge; (b) force polygon

2.3   SURCHARGE LOADS ON RETAINING WALLS

2.3.1   Point-load surcharge

Boussinesq (1985) solved the problem stresses produced at any point in a homogeneous, elastic, and isotropic medium produced from a point load on the surface were given in [Eq. (2.37), (2.38) and (2.39)].

$$\Delta\sigma_x = \frac{P}{2\pi}\left\{\frac{3x^2z}{L^5} - (1-2\mu)\left[\frac{x^2-y^2}{Lr^2(L+z)} + \frac{y^2z}{L^3r^2}\right]\right\} \tag{2.37}$$

$$\Delta\sigma_x = \frac{P}{2\pi}\left\{\frac{2y^2z}{L^5} - (1-2\mu)\left[\frac{y^2-x^2}{Lr^2(L+z)} + \frac{x^2z}{L^3r^2}\right]\right\} \tag{2.38}$$

And

$$\Delta\sigma_x = \frac{3P}{2\pi}\frac{z^3}{L^5} = \frac{3P}{2\pi}\frac{z^3}{(r^2+z^2)^{5/2}} \tag{2.39}$$

Where

$$r = \sqrt{x^2+y^2}$$
$$L = \sqrt{x^2+y^2+z^2} = \sqrt{r^2+z^2}$$
$$\mu = Poisson's\ ratio$$
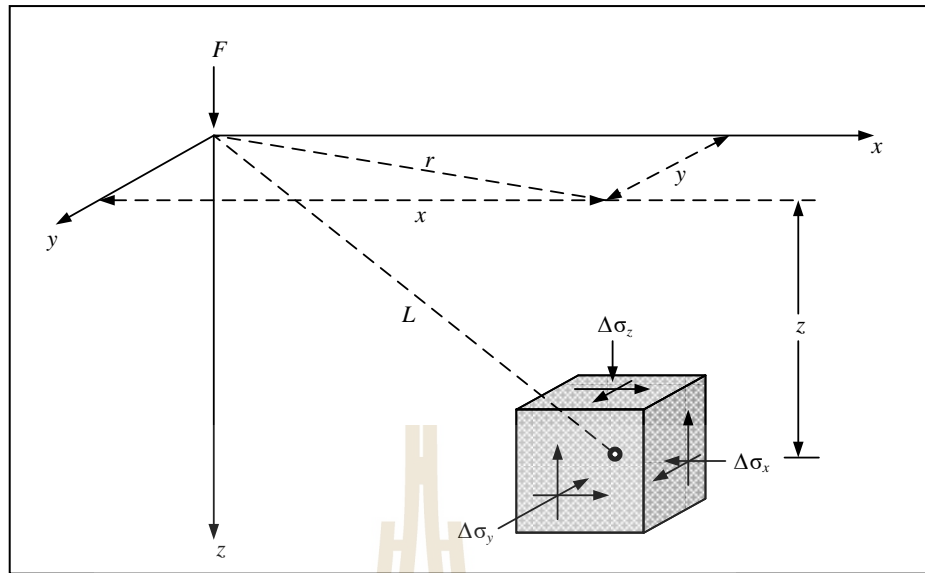
Figure 2.15 Stresses in an elastic medium caused by a point load

It is now to apply Eq. (2.37) to compute the lateral pressure on a retaining wall caused by the point load Q located at the surface of the backfill as shown in Figure 2.16a. If the load Q is placed on the plane of the section shown, y can be substituted as 0 in Eq. (2.37). Also, assuming that $\mu = 0.5$,

$$\sigma_{h}^{'} = \frac{Q}{2\pi}\left(\frac{3x^2 Z}{L^5}\right) \tag{2.40}$$

Where

$L = \sqrt{X^2 + Z^2}$. Substituting

$x = mH$ and

$z = nH$ into Eq. (2.40), we have

$$\sigma^{'}_{h} = \frac{3Q}{2\pi H^2} \frac{m^2 n}{\left(m^2 + n^2\right)^{5/2}}$$ (2.41)

The horizontal stress expressed by Eq. (2.41) does not include the restraining effect of the wall. This expression was investigated by Gerber (1929) and Spangler (l938) with large-scale tests. On the basis of the experimental findings, Eq. (2.41) has been modified as follows to agree with the real conditions:

For $m > 0.4$,

$$\sigma^{'}_{h} = \frac{1.77Q}{H^2} \frac{m^2 n^2}{\left(m^2 + n^2\right)^3}$$ (2.42)

For $m \le 0.4$,

$$\sigma^{'}_{h} = \frac{0.28Q}{H^2} \frac{n^2}{\left(0.16 + n^2\right)^3}$$ (2.43)
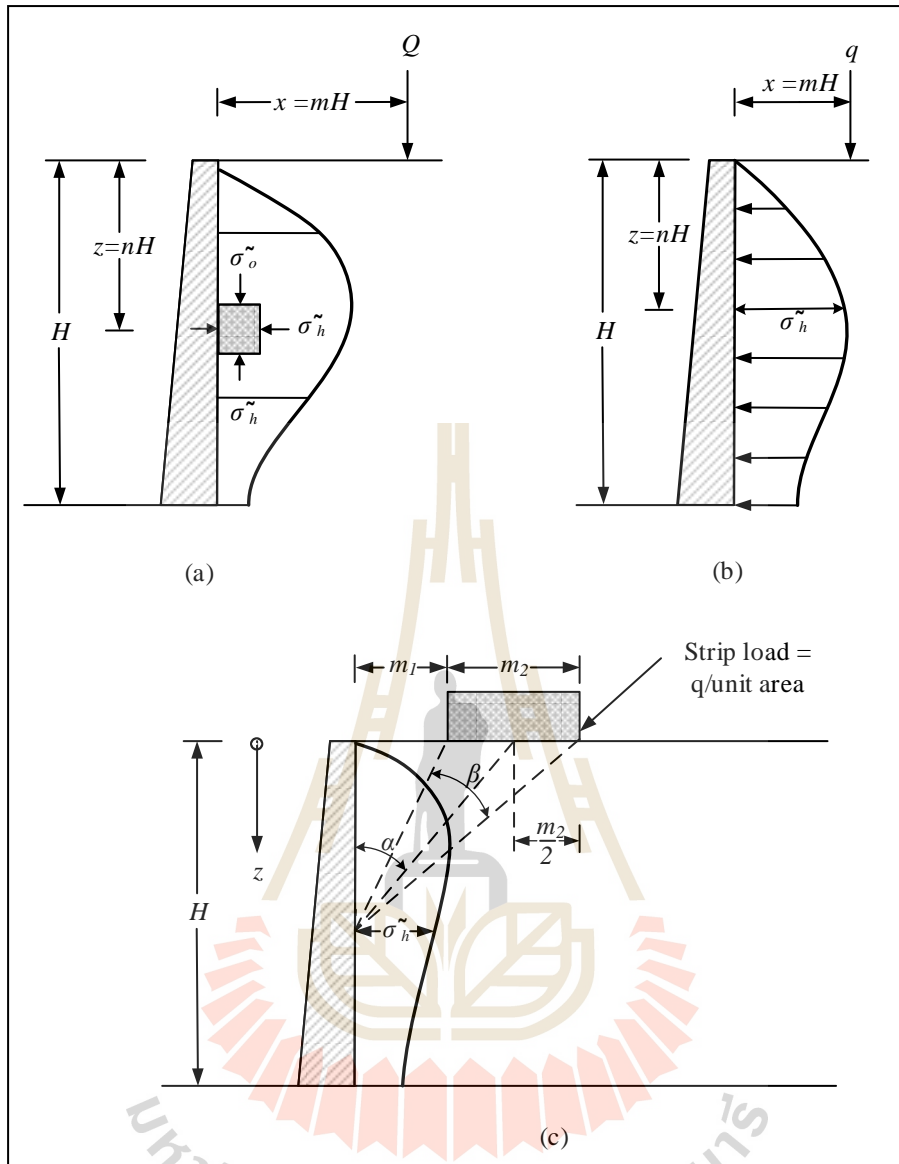
Figure 2.16 Lateral pressure on a retaining wall due to a (a) point load, (b) line load,

and (c) strip load

2.3.2   Line-load surcharge

Figure 2.16b shows the distribution of lateral pressure against the

vertical back face of the wall caused by a line-load surcharge placed parallel to the

crest. The modified forms of the equations [similar to Eq. (2.42) and (2.43) for the case of point load surcharge] for line-load surcharges are, respectively,

$$\sigma_h' = \frac{4q}{\pi H} \frac{m^2 n}{\left(m^2 + n^2\right)^2} \qquad (for \ m > 0.4) \qquad (2.44)$$

And

$$\sigma_h' = \frac{0.203q}{H} \frac{n}{\left(0.16 + n^2\right)^2} \qquad (for \ m \le 0.4) \qquad (2.45)$$

Where

$q =$ load per unit length of the surcharge.

2.3.3 Strip-load surcharge

Figure 2.16c shows a strip load surcharge with an intensity of q per unit area located at a distance m_1, from a wall of height H. On the basis of the theory of elasticity, the horizontal stress at a depth z on a retaining structure can be given as

$$\sigma_h' = \frac{q}{H}(\beta - \sin\beta\cos 2\alpha) \qquad (2.46)$$

The angles α and β are defined in Figure 2.16c. For actual soil behavior (from the wall restraining effect). the preceding equation can be modified to

$$\sigma_h' = \frac{2q}{H}(\beta - \sin\beta\cos 2\alpha) \qquad (2.47)$$

The nature of the distribution of $\sigma_h^{'}$, with depth is shown in Figure 2.16c. The force P per unit length of the wall caused by the strip load alone can be obtained by integration of $\sigma_h^{'}$ with limits of z from 0 to H (Lambe, 1969-1979).

2.4 OTHER LIVE LOADS

2.4.1 Live load (people)

A horizontal load on the top edge should be considered due to the peaples, which can act in both directions (tension / compression). Its value is 0.5 kN/m.

2.4.2 Live load (vehicle)

Live load is not a requirement to bear the load of an intentionally collisioning vehicle. The vehicleload is applied at slow, e.g. reversing into consideration. The load is a concentrated 5 kN/m force and the point of contact is at 1.2 m height (Figure 2.17).
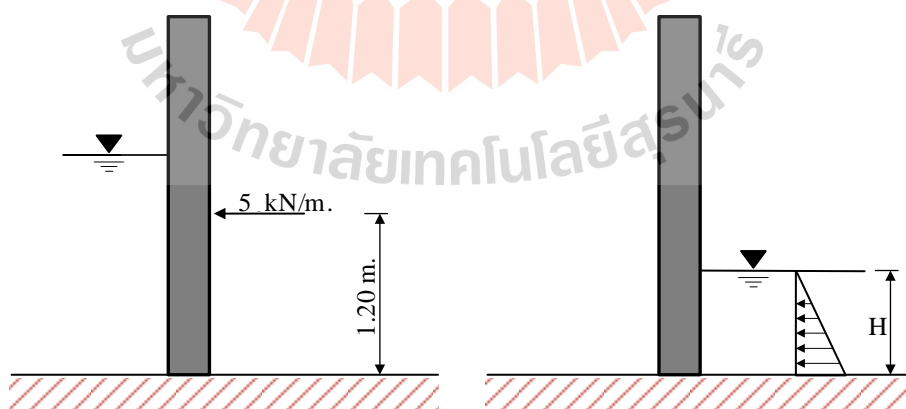
Fig. 2.17 Vehicle load and dry-side water pressure

2.5 FAILURE MODE OF RETAINING WALLS

Retaining walls are constructed to provide sufficient structural ability with suitable movements, sufficient foundation bearing capacity with appropriate settlements, and satisfactory stability of slopes adjacent to walls (Lee et al., 1973; Anderson et al., 1985). The tolerable level of lateral and vertical deformations is controlled by the type and location of the wall structure and surrounding facilities.

2.5.1 External failure

Like the conventional reinforced concrete cantilever and gravity retaining walls, MSE structures are considered the following four potential external failure mechanisms:

1) Sliding of the reinforced soil block over the foundation soil

2) Overturning of the reinforced soil block

3) Bearing capacity failure of the foundation soil

4) Deep sated stability failure (rotational slip-surface or slip along a plan of weaknes)

The external failures of the MSE structures are shown in 2.18. Due to its flexibility and satisfactory field performance, the factor of safety values for external failure are lower than those used for classical unreinforced retaining structures. For example, the factor of safety for overall bearing capacity is 2 lower than the conventional value of which is used for more rigid structures. The sliding requirement for external stability generally governs the dimension of the MSE structure.
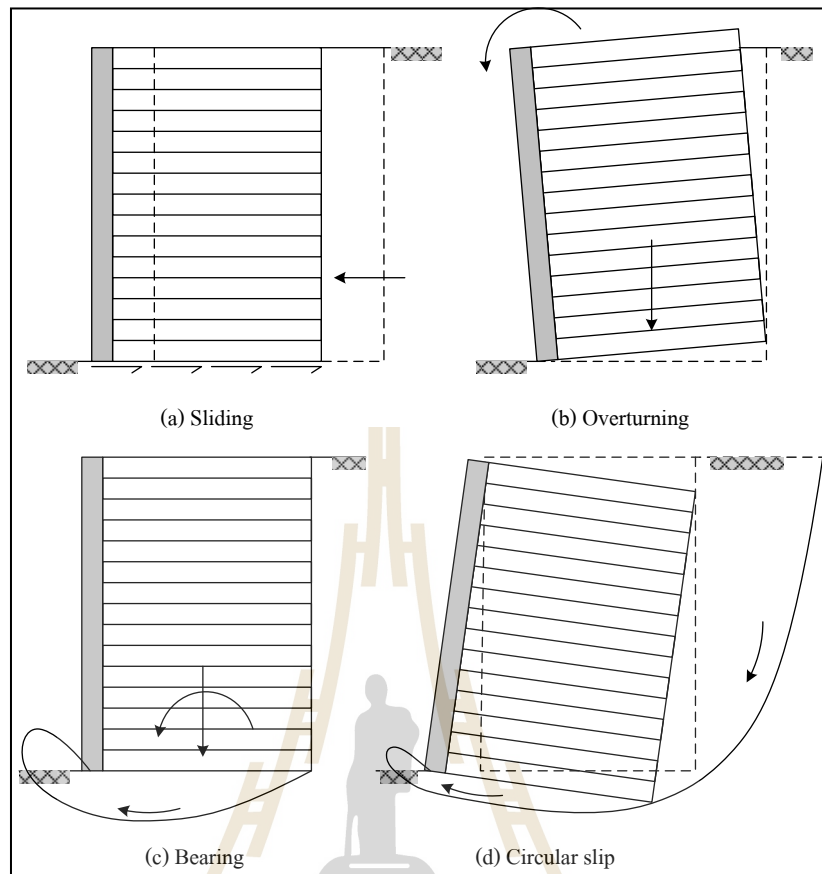
Figure 2.18 Potential external failure mechanisms of MSE structures

2.5.2 **Internal failure**

The reinforced soil structure is internally stable once the reinforcement can carry the tensile stress and shear stress.

The internal failure mode can be categorized into two theories (Figure-2.22):

1) Tensile failure is caused by rupture of reinforcement. Tension occurs when the tension developed in the reinforcement exceeds its tensile strength.

2) Slippage failure is caused by slippage between soil and which may be called pullout, friction or bond failure of the reinforcement. Friction on

failure will occur when tension is less than its tensile strength but greater than friction or bond resistance of the reinforcement.
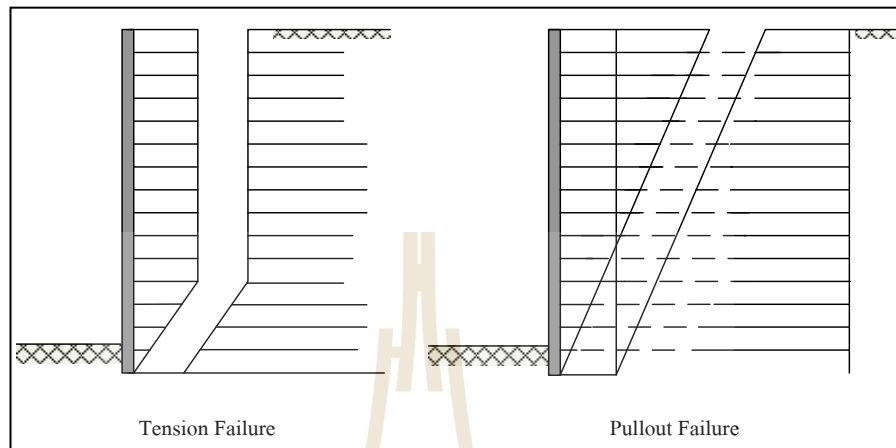
Figure 2.19 Internal failure mechanisms of MSE structures

2.6 THEORY OF FINITE ELEMENT ANALYSIS

2.6.1 Elastic strains

Material models for soil and rock are generally expressed as a relationship between infinitesimal increments of effective stress (effective stress rates) and infinitesimal increments of strain (strain rates) Brinkgreve, (2014). This relationship may be expressed in the form:

$$\dot{\sigma}' = M\dot{\varepsilon} \tag{2.48}$$

Where

M is a material stiffness matrix.

The simplest material model in PLAXIS is based on Hooke's law for isotropic linear elastic behavior. This model is available under the name Linear Elastic model, but it is also the basis of other models. Hooke's law can be given by the equation:

$$\begin{bmatrix} \dot{\sigma}'_{xx} \\ \dot{\sigma}'_{yy} \\ \dot{\sigma}'_{zz} \\ \dot{\sigma}'_{xy} \\ \dot{\sigma}'_{yz} \\ \sigma'_{zx} \end{bmatrix} = \frac{E'}{(1-2v')(1+v')} \begin{bmatrix} 1-v' & v' & v' & 0 & 0 & 0 \\ v' & 1-v' & v' & 0 & 0 & 0 \\ v' & v' & 1-v' & 0 & 0 & 0 \\ 0 & 0 & 0 & \frac{1}{2}-v' & 0 & 0 \\ 0 & 0 & 0 & 0 & \frac{1}{2}-v' & 0 \\ 0 & 0 & 0 & 0 & 0 & \frac{1}{2}-v' \end{bmatrix} \begin{bmatrix} \dot{\varepsilon}_{xx} \\ \dot{\varepsilon}_{yy} \\ \dot{\varepsilon}_{zz} \\ \dot{\gamma}_{xy} \\ \dot{\gamma}_{yz} \\ \dot{\gamma}_{zx} \end{bmatrix} \quad (2.49)$$

The elastic material stiffness matrix is often denoted as D^e. Two parameters are used in this model, theveffective Young's E', and the effective Poisson's ratio, v'. In the remaining part of this manual effective parameter are denoted without dash $(')$, unless a different meaning is stated. The symbols E and v are sometimes used in this manual in combination with the subscript ur to emphasize that the parameter is explicitly meant for unloading and reloading. A stiffness modulus may also be indicated with the subscript ref to emphasize that it refers to a particular reference level $\left(y_{ref}\right)$.

According to Hooke's law, the relationship between Young's modulus E and other stiffness modulus, such as the shear modulus G, the bulk modulus K, and the oedometer modulus E_{oed}, is given by:

$$G = \frac{E}{2(1+v)} \qquad (2.50a)$$

$$K = \frac{E}{3(1-2v)} \qquad (2.50b)$$

$$E_{oed} = \frac{(1-v)E}{(1-2v)(1+v)} \qquad (2.50c)$$

During the input of material parameters for the Linear Elastic model or the Mohr-Coulomb model the values of G and E_{oed} are presented as auxiliary parameters (alternatives), calculated from Eq. (2.53). Note that the alternatives are influenced by the input values of E and v. Entering a particular value for one of the alternatives G or E_{oed} results in a change of the E modulus, while v remains the same.

It is possible for the Linear Elastic module and the Mohr-Coulomb model to specify a stiffness that varies linearly with depth.

Together with the input of E_{inc} the input of y_{ref} becomes relevant. Above y_{ref} the stiffness is equal to E_{ref}. Below the stiffness is given by:

$$E(y) = E_{ref} + (y_{ref} - y)E_{inc} \qquad y < y_{ref} \qquad (2.51)$$

The Linear Elastic model is usually inappropriate to model the highly non-linear behavior of soil, but it isvof interest to simulate structural behavior, such as thick concrete walls or plates, for which strength properties are usually very high compared with those of soil. For these applications, the Linear Elastic model will

often be selected together with Non-porous type of material behavior in order to exclude pore pressures from these structural elements.

2.6.2   Undrained effective stress analysis (effective stiffness parameters).

In PLAXIS it is possible to specify undrained behavior in an effective stress analysis using effective model parameters. This is achieved by identifying the type of material behavior (Drainage type) of a soil layer as Undrained (A) or Undrained (B). In this section, it is explained how PLAXIS deals with this special option.

The presence of pore pressures in a soil body, usually caused by water, contributes to the total stress level. According to Terzaghi's principle, total stresses σ can be divided into effective stresses σ' and pore pressures σ_w. However, water is supposed not to sustain any shear stress, and therefore the effective shear stresses are equal to the total shear stresses:

$$\sigma_{xx} = \sigma'_{xx} + p_w \tag{2.52a}$$

$$\sigma_{yy} = \sigma'_{yy} + p_w \tag{2.52b}$$

$$\sigma_{zz} = \sigma'_{zz} + p_w \tag{2.52c}$$

$$\sigma_{xy} = \sigma'_{xy} \tag{2.52d}$$

$$\sigma_{yz} = \sigma'_{yz} \tag{2.52e}$$

$$\sigma_{zx} = \sigma'_{zx} \tag{2.52f}$$

Note that, similar to the total and the effective stress components, p_w is considered negative for pressure.

A further distinction is made between steady state pore, p_{steady}, and excess pore stress, p_{excess}:

$$P_w = P_{steady} + P_{excess} \qquad (2.53)$$

Steady state pore pressures are considered input data, i.e. generated on the basis of phreatic levels. Excess pore pressures are generated during plastic calculations for the case of undrained (A) or (B) material behavior or during a consolidation analysis. Undrained material behavior and corresponding calculation of excess pore pressure are described below.

$$P_w = P_{excess} \qquad (2.54)$$

Hooke's law can be inverted to obtain:

$$
\begin{bmatrix} \varepsilon^e_{xx} \\ \varepsilon^e_{yy} \\ \varepsilon^e_{zz} \\ \gamma^e_{xy} \\ \gamma^e_{yz} \\ \gamma'_{zx} \end{bmatrix} = \frac{1}{E'} \begin{bmatrix} 1 & -v' & -v' & 0 & 0 & 0 \\ -v' & 1 & -v' & 0 & 0 & 0 \\ -v' & -v' & 1 & 0 & 0 & 0 \\ 0 & 0 & 0 & 2+2v' & 0 & 0 \\ 0 & 0 & 0 & 0 & 2+2v' & 0 \\ 0 & 0 & 0 & 0 & 0 & 2+2v' \end{bmatrix} \begin{bmatrix} \dot{\sigma}'_{xx} \\ \dot{\sigma}'_{yy} \\ \dot{\sigma}'_{zz} \\ \dot{\sigma}'_{xy} \\ \dot{\sigma}'_{yz} \\ \dot{\sigma}'_{zx} \end{bmatrix} \qquad (2.55)
$$

Substituting Eq. (2.22) gives:

$$\begin{bmatrix} \dot{\varepsilon}^e_{xx} \\ \dot{\varepsilon}^e_{yy} \\ \dot{\varepsilon}^e_{zz} \\ \dot{\gamma}^e_{xy} \\ \dot{\gamma}^e_{yz} \\ \dot{\gamma}'_{zx} \end{bmatrix} = \frac{1}{E'} \begin{bmatrix} 1 & -v' & -v' & 0 & 0 & 0 \\ -v' & 1 & -v' & 0 & 0 & 0 \\ -v' & -v' & 1 & 0 & 0 & 0 \\ 0 & 0 & 0 & 2+2v' & 0 & 0 \\ 0 & 0 & 0 & 0 & 2+2v' & 0 \\ 0 & 0 & 0 & 0 & 0 & 2+2v' \end{bmatrix} \begin{bmatrix} \dot{\sigma}'_{xx} - p_w \\ \dot{\sigma}'_{yy} - p_w \\ \dot{\sigma}'_{zz} - p_w \\ \dot{\sigma}'_{xy} \\ \dot{\sigma}'_{yz} \\ \dot{\sigma}'_{zx} \end{bmatrix} \quad (2.56)$$

Considering slightly compressible water, the rate of excess pore pressure is written as:

$$\dot{p}_w = \frac{K_w}{n}(\dot{\varepsilon}^e_{xx} + \dot{\varepsilon}^e_{yy} + \dot{\varepsilon}^e_{zz}) \quad (2.57)$$

In which K_w is the bulk modulus of the water and n is the soil porosity. The inverted form of Hooke's law may be written in terms of the total stress rates and the undrained parameters E_u and v_u:

$$\begin{bmatrix} \dot{\varepsilon}^e_{xx} \\ \dot{\varepsilon}^e_{yy} \\ \dot{\varepsilon}^e_{zz} \\ \dot{\gamma}^e_{xy} \\ \dot{\gamma}^e_{yz} \\ \dot{\gamma}^e_{zx} \end{bmatrix} = \frac{1}{E_u} \begin{bmatrix} 1 & -v_u & -v_u & 0 & 0 & 0 \\ -v_u & 1 & -v_u & 0 & 0 & 0 \\ -v_u & -v_u & 1 & 0 & 0 & 0 \\ 0 & 0 & 0 & 2+2v_u & 0 & 0 \\ 0 & 0 & 0 & 0 & 2+2v_u & 0 \\ 0 & 0 & 0 & 0 & 0 & 2+2v_u \end{bmatrix} \begin{bmatrix} \dot{\sigma}_{xx} \\ \dot{\sigma}_{yy} \\ \dot{\sigma}_{zz} \\ \dot{\sigma}_{xy} \\ \dot{\sigma}_{yz} \\ \dot{\sigma}_{zx} \end{bmatrix} \quad (2.58)$$

Where:

$$E_u = 2G(1+v_u) \quad and \quad v_u = \frac{v' + \mu(1+v')}{1+2\mu(1+v')} \quad (2.59)$$

$$\mu = \frac{1}{3n}\frac{K_w}{K'} \quad and \quad K' = \frac{E'}{3(1-2v')} \quad (2.60)$$

Hence, the special option for undrained behavior in PLAXIS (Undrained (A) or Undrained (B)) is such that the effective parameters G and v' are transferred into undrained parameters E_u and v_u according to Eq. (2.62) and (2.63). Note that the index u is used indicate auxiliary parameters undrained soil. Hence, E_u and v_u should not be confused with E_{ur} and v_{ur} as used to unloading / reloading.

Fully incompressible behavior is obtained for $v_u = 0.5$. However, taking $v_u = 0.5$ leads to singularity of stiffness matrix. In fact, water is not fully incompressible, but realistic bulk modulus water is very large. order to avoid numerical problems caused by an extremely low compressibility, v_u is by default, taken as 0.495, which make undrained soil body slightly compressible. In order to ensure realistic computational results, the bulk modulus of the water must be high compared with the bulk modulus of the soil Skeleton, $i.e.$ $K > n\,K'$. This condition is sufficiently ensured by requiring $v' \leq 0.35$.

Consequently, for material behavior Undrained (A) or Undrained (B), a bulk modulus for water is automatically added to the stiffness matrix. The value of the bulk modulus is given by:

$$\frac{K_w}{n} = \frac{3(v_u - v')}{(1 - 2v_u)(1 + v')} K' = 300\frac{0.495 - v'}{1 + v'} K' > 30K' \qquad (2.61)$$

At least for $v' \leq 0.35$. In retrospect it is worth mentioning here a review about the Skempton B-parameter.

2.6.3   Skempton B-parameter

When the Drainage type (type of material behavior) is to Undrained (A) or Undrained (B), PLAXIS automatically assumes an implicit undrained bulk modulus, K_u, for the soil as a whole (soil skeleton + water) and distinguishes between total stresses, effective stresses and excess pore pressures:

Total stress: $\Delta p = K_u \Delta \varepsilon_v$

Effective stress: $\Delta p' = (1 - B)\Delta p + K' \Delta \varepsilon_v$

Excess pore pressure $\Delta p_w = B\Delta p = +\dfrac{K'_w}{n}\Delta \varepsilon_v$

Note that for Undrained (A) or Undrained (B) effective stiffness parameters should be entered in the material data set, i.e. E' and v' and not E_u and ν_u , or the respective stiffness parameters in advanced models. The undrained bulk modulus is automatically calculated by PLAXIS using Hooke's law of elasticity:

$$K_u = \frac{2G(1 + v_u)}{3(1 - 2v_u)} \qquad \text{where} \quad G = \frac{E'}{2(1 - 2v')}$$

and $\nu_u = 0.495$ (when using the Standard setting)

or $\nu_u = \dfrac{3v' + B(1 - 2v')}{3 - B(1 - 2v')}$ when using the Manual setting with input

of Skempton's B-parameter

A particular value of the undrained Poisson's ratio, ν_u implies a corresponding reference bulk stiffness of the pore fluid, $K_{w,ref} / n$:

$$\frac{K_{w,ref}}{n} = K_u - K' \qquad \text{where} \qquad K' = \frac{E'}{3(1-2v')}$$

This value of $\dfrac{K_{w,ref}}{n}$ is generally much smaller than the real bulk stiffness of pure water, $K_w^o \left(= 2 \cdot 10^6 \, kN/m^2\right)$.

If the value of Skempton's B-parameter is unknown, but the degree of saturation, s, and the porosity, n, are known instead, the bulk stiffness of the pore fluid can be estimated from:

$$\frac{K_w}{n} = \frac{K_w^0 K_{air}}{SK_{air} + (1-s)K_w^0} \frac{1}{n}$$

Where $K_{air} = 100 \, kN/m^2$ for air under atmospheric pressure.

The value of Skempton's B-parameter can now be calculated from the ratio bulk stiffnesses of the soil skeleton and the pore fluid:

$$B = \frac{1}{1 + \dfrac{nK'}{K_w}}$$

The rate of excess pore pressure is calculated from the (small) volumetric strain rate, according to:

$$\dot{p}_w = \frac{K_w}{n}\varepsilon_v \qquad\qquad (2.62)$$

The types of elements used in PLAXIS are sufficiently adequate to avoid mesh locking effects for nearly in compressible materials.

This special option to model undrained material behavior on the basis of effective model parameters is available for most material in PLAXIS. This enables undrained calculations to be executed with effective stiffness parameters, with explicit distinction between effective stresses and (excess) pore pressures. However, shear induced (excess) pore pressure may not be sufficiently included.

Such an analysis requires effective soil parameters and is therefore highly convenient when such parameters are available. For soft soil projects, accurate data on effective parameters may not always be available. Instead, in situ tests and laboratory tests may have been performed to obtain undrained soil parameters. In such situations measured undrained Yong's modulus can be easily converted into effective Yong's modulus based on Hooke's law:

$$E' = \frac{2(1+v')}{3}E_u \qquad\qquad (2.63)$$

For advanced models there is on such direct conversion possible. In that case it is recommended to estimate the required effective stiffness parameter from the measured undrained stiffness parameter, then perform a simple undrained test to check the resulting undrained stiffness and adapt the effective stiffness if needed. The soil test facility may be used as a convenient tool to perform such test.

2.6.4 Undrained effective stress analysis with effective strength parameter (undrained A)

In principle, undrained effective stress analysis as described in Section 2.7.3 can be used in combination with effective strength parameters   and   to model the material's undrained shear strength (Undrained (A)). In this case, the development of the pore pressure plays a crucial role in providing the effective stress path that leads to failure at a realistic value of undrained shear strength$\left(c_u \, or \, s_u \right)$. However, note that most soil models are not capable of providing the right effective stress path in undrained loading. As a result, they will produce the wrong undrained shear strength if the material strength has been specified on the basis of effective strength are parameters. Another problem is that for undrained materials effective strength parameters are usually not available from soil investigation data. In order to overcome these problems, some models for a direct input of undrained shear strength. This approach is described in Section 2.7.5

If the user wants to model the material strength of undrained materials using the effective strength parameters $\varphi^{'}$ and $c^{'}$, this can be done in PLAXIS in the same way as for drained materials. However, in this case the drainage type must be set to Undrained (A). As a result, PLAXIS will automatically add the stiffness of water to the stiffness matrix (see Section 2.7.3) in order to distinguish between effective stresses and (excess) pore parameters in undrained loading conditions is that after consolidation a qualitatively increased shear strength is obtained, although this increased shear strength could also be quantitatively wrong, for the same reason as explained before.
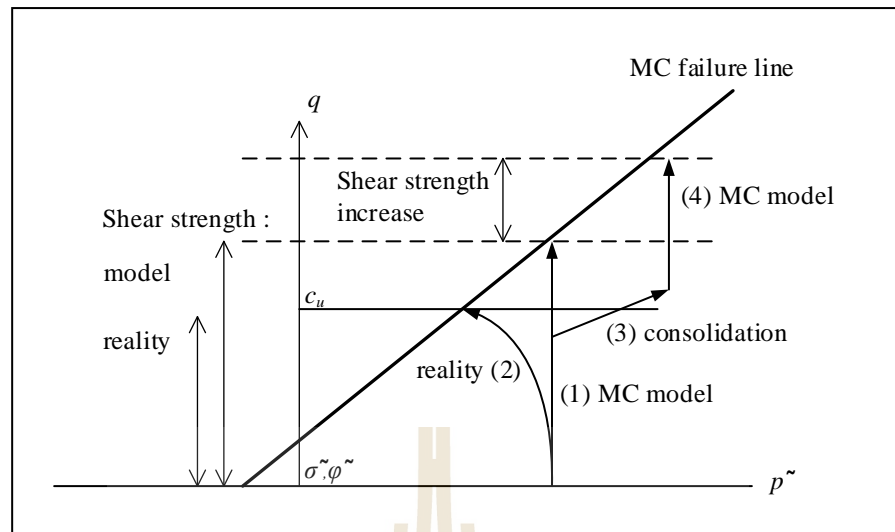
Figure 2.20 Illustrates of stress parth; reality vs. Mohr-Coulomb model

Figure 2.20 illustrates an example using the Mohr-coulomb model. When the Drained type is set to Undrained (A), the model will follow an effective stress path where the mean effective stress, p', remains constant all the way up to failure 1). It is know that especially soils, like normally consolidated clays and peat, will follow an effective stress path in undrained loading where p' reduces significantly as a result of shear induced pore pressure 2). As a result, the maximum deviatoric stress that can be reached in the model is over-estimated in the Mohr-Coulomb model. In other words, the mobilized shear strength in the model supersedes the available undrained shear strength.

If, at some stress state, the soil consolidated, the mean effective stress will increase 3). Upon further undrained loading with the Mohr-Conlomb model, the observed shear strength will be increased 4) compared to the previous shear strength, but this increased shear strength may again be unrealistic, especially for soft soil.

On the other hand, advanced models do include, to some extent, the reduction of mean effective stress in undrained loading, but even when using advanced models, it is generally advised to check the mobilised shear strength in the Output program against the available (undrained) shear strength when this approach is followed.

2.6.5 Undrained effective stress analysis with undrained strength parameters (undrained B)

For undrained soil layers with a known undrained shear strength profile, PLAXIS offers for some models the possibility of an undrained effective stress analysis, as described in Section 2.7.3 (Drainage type = Undrained (B)), with direct input of the undrained shear strength, i.e. setting the friction angle to zero and the cohesion equal to the undrained shear strength $(\varphi = \varphi_u \ 0°; c = s_u)$. Also in this case, distinction is made between pore pressures and effective stresses. Although the pore pressures and effective stress path may not be fully correct, the resulting undrained shear strength is not affected, since it is directly specified as an input parameter.

The option perform an undrained effective stress analysis with undrained strength properties is only available for the Mohr-Coulomb model, the Hardening Soil model, the HS small model and the NGI-ADP modal. Since most soils show an increasing shear strength with depth, it is possible to specify the increase per unit of depth in PLAXIS in the Advanced subtree in the Parameter tab-sheet of the soil window.

Further note that whenever the Drainage type parameter is set to Undrained (B), effective values must be entered for the stiffness parameter (Young's

modulus E') and Poisson ratio v' in case of the Mohr-Coulomb model or the respective stiffness parameters in the advanced models).

2.6.6 Undrained total stress analysis with undrained parameters (undrained C)

If, for any reason, it is desired not to use the Undrained (A) or Undrained (B) options in PLAXIS to perform an undrained effective stress analysis, one may simulate undrained behavior using a total stress analysis with all parameters specified as undrained. In that case, stiffness is modeled using an undrained Yong's modulus E_u and an undrained Poisson ratio v_u, and strength is modeled using an undrained shear strength S_u and $\varphi = \varphi_u = 0°$. Typically, for the undrained Poisson ratio a value close to 0.5 is selected (between 0.495 and 0.499). A value of 0.5 exactly is not possible, since this would lead to singularity of the stiffness matrix.

In PLAXIS it is possible to perform a total stress analysis with undrained parameters if the Mohr-Coulomb model or the NGI-ADP model is used. In this case, one should select Undrained (C) as the Drainage type. The disadvantage of the undrained total stress analysis is that no distinction is made between effective stresses and pore pressures. Hence, all output referring to effective stresses should now be interpreted as total stresses and all pore pressures are equal to zero.

2.6.7 Safety analysis

In structural work, the factor of safety is usually classified as the ratio of the failure load to the working load. For earth structures, however, this description is not commonly used. For embankments, for instance, the loading is caused by soil mass and an increase in soil mass would not certainly lead to collapse. In addition, a

slope of purely frictional soil will not fail in a test in which the self-weight of the soil is increased. A more appropriate definition of the factor of safety is therefore:

$$\text{Safety factor} = \frac{S_{maximum\ available}}{S_{needed\ for\ equilibrium}} \tag{2.64}$$

where S represents the shear strength. The ratio of the true strength to the computed minimum strength required for equilibrium is the safety factor that is conventionally used in soil mechanics. By introducing the standard Coulomb condition, the safety factor is obtained:

$$\text{Safety factor} = \frac{c - \sigma_n \tan \varphi}{c_r - \sigma_n \tan \varphi_r} \tag{2.65}$$

where c and φ are the input strength parameters and σ_n is the actual normal stress component. The parameters c_r and φ_r are reduced strength parameters that are just large enough to maintain equilibrium. The principle described above is the basis of the method of safety that can be used in PLAXIS to calculate a global safety factor. In this approach the cohesion and the tangent of the friction angle are reduced in the same proportion:

$$\frac{c}{c_r} = \frac{\tan \varphi}{\tan \varphi_r} = \sum Msf \tag{2.66}$$

The reduction of strength parameters is controlled by the multiplier $\sum Msf$ (Figure 2.21). This parameter is increased in a step-by-step procedure until failure occurs. The safety factor is then defined as the value of $\sum Msf$ at failure,

provided that at failure a more or less constant value is obtained for a number of successive load steps.
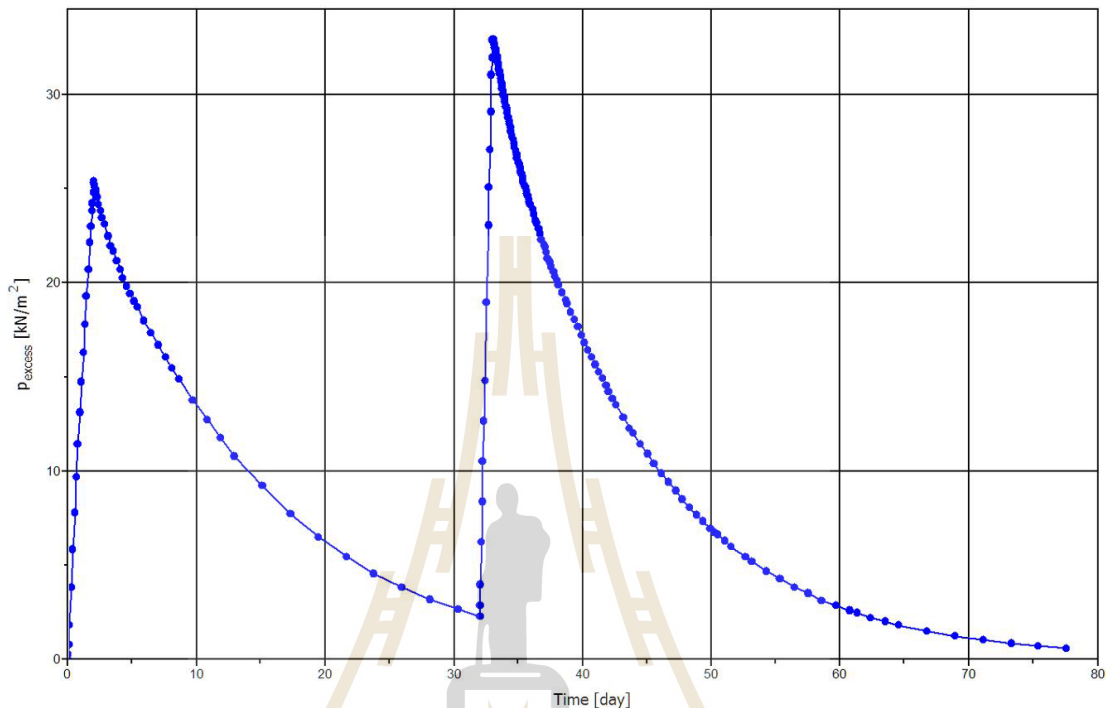
Figure 2.21 Development of excess pore pressure under the embankment

2.7 CASE STUDIES

In this section, an overview of some principles related to FEM and the uncertainties in geotechnical engineering is presented. More precisely, an introduction into FEM concept and a discussion over the different types of FEM are made. Moreover, the uncertainties in geotechnical engineering are stressed and the general framework according to which they are handled is described. Finally, previous studies that are associated with the application of FEM on soil structures and the reliability analysis are discussed.

The conventional method stability analysis in a soil body is represented by LEM (Limit equilibrium method) although FEM is increasingly used by designers/researchers. The latter has been proved to be quite realistic for the progressive behavior (i.e. stress-strain development in different construction phases) of a soil system under the effect of stress redistribution in comparison with classical models. Especially, in their master thesis, Johansson & Sandeman (2014) compared the deformations and the forces measured at a deep excavation supported by anchored sheet pile wall in a railway tunnel located in Gothenburg in Sweden with 1D finite element software, the 2D finite element software (Plaxis) and hand calculations. They proved that Plaxis produces reliable results for horizontal deformations in the sheet pile wall and anchor forces when compared to in-situ measurements.

Moreover, in González et al. (2013), it was proved that the simplification of reality done by the classical methods, such as Blum's, Engel's, Krey's methods etc (for further information for these methods a reference is made to González et al. (2013)), allows us to generally understand the behavior of the system wall-soil. Nonetheless, the results that came out of this analysis were found to be quite conservative whereas FEM managed to give a more realistic interpretation of the wall's movement.

Seed et al. (2008) analyzed the I-Wall by using FEM to evaluate and identify causes of failure of the I-wall. The wall was affected by Hurricane Katrina in 2005. The external failure of the wall is shown in Figure 2.22. Due to the increased water level in the canal, the lateral pressure increased. As a result, the wall is flat and the Factor of Safety (FS) ratio decreases with increasing level (Figure 2.23).
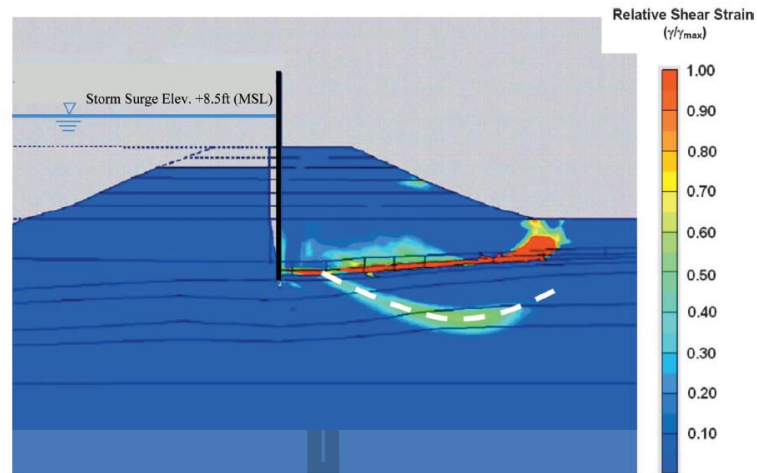
Figure 2.22 Failure Plan by FEA (Seed et al. 2008)
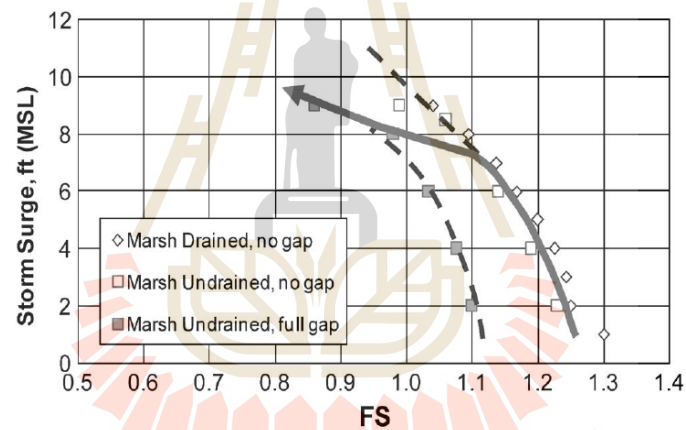
Figure 2.23 The relationship between FS and water level.(Seed et al. 2008)

Hossain et al. (2012) introduced FEM as a tool for analyzing and predicting MSE wall behavior to compare the results of the analysis. FEM method with the results of measuring the movement of the wall in the field. They indicated that the results from the FEM analysis were good and close to the values obtained from field measurements. Therefore, the use of FEM in geotechnical problem analysis helps save time and accuracy closer to reality than calculated LEM.
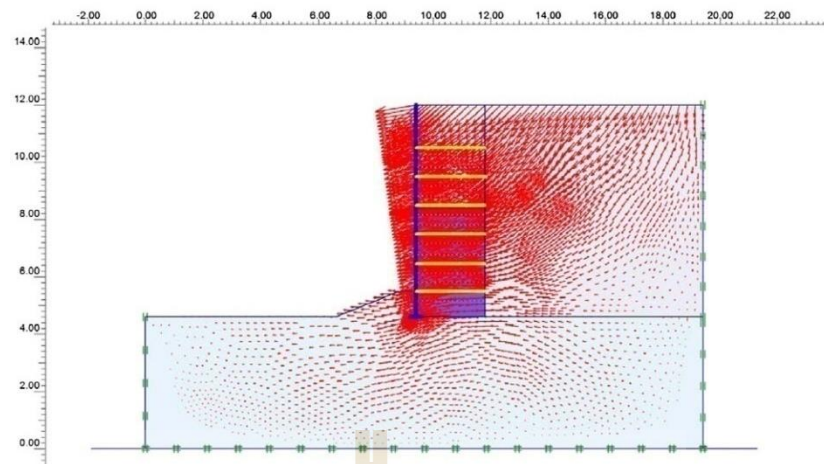
Figure 2.24. Model predicted displacements. (Hossain et al. 2012)

Tan (2008) presented the use of FEM for analysis of geotechnical problems that occurred during construction and after highway construction, along with the monitoring of the sheet pile wall, shown in Figure 2.25. In comparison with field measurements, it is known that behavior of the sheet pile is consistent with the measurement in the field. In addition, the accuracy values obtained from the analysis are based on the input of the correct parameters. The results are reasonable.

Suksiripattanapong et al. (2012) studied the behavior of internal reinforcement of the bearing reinforcement earth (BRE) wall by simulation of the full scale model in the field as shown in Fig. 2.26. The installation of moving equipment and force measuring equipment during construction and after construction were also investigated. Finally, present the FEM method for predicting the behavior and internal stability of the (BRE) wall. The results from the FEM analysis compared with the field measurements are in good agreement.

Therefore, it can be concluded that the FEM in research or solving geotechnical problems. helps predict various behaviors of earth-retaining structures

more convenient and faster. But the reliable result depends on the right selection of engineering parameters and constitutive model.
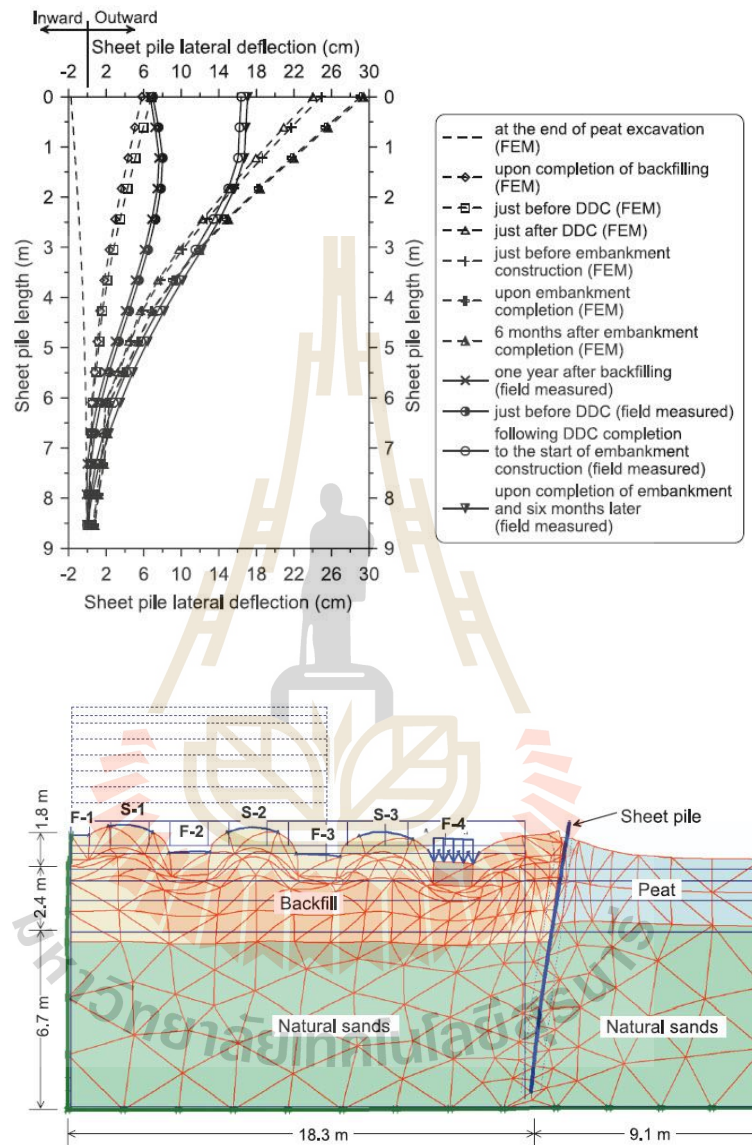
Figure 2.25 Comparison between the FE-calculated and field-measured sheet pile

deflections. (Tan, 2008)
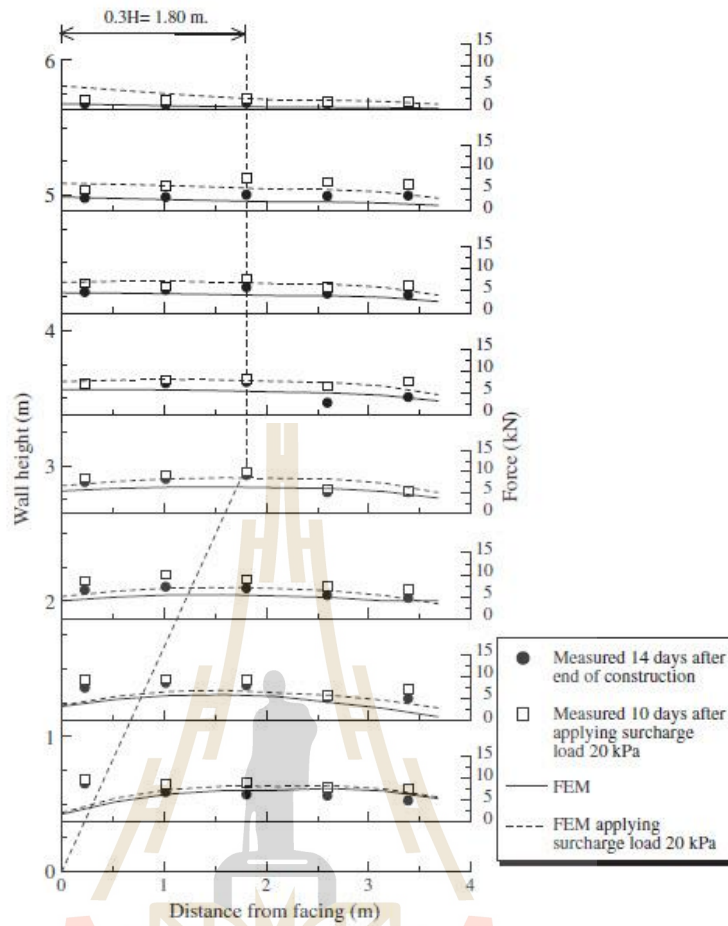
Figure 2.26 Comparison between the simulated and measured tension forces in the

reinforcements. (Suksiripattanapong et al. 2012)

2.8 REFERENCE

Anderson, L.R., Sharp, K.D., Woodward, B.L., and Winward, R.F. (1985), **"Performance of the Raininer Avenue welded wire retaining wall"**, Seattle, Washington, Report submitted to the Hilfiker Co. and Washington State Department of Transportation, USA.

Boussinesq, J. (1885) **Application des potentials a l' etude de l' equilibreet du mouvement des solidselastiques,** Gauthier-Villars, Paris

Brinkgreve, R. B. J., Kumarswamy, S., Swolfs, W. M., Waterman, D., Chesaru, A., Bonnier, P. G., & Haxaire, A. (2014). **Plaxis 2014. PLAXIS bv**, the Netherlands.

Coulomb, C. A. (1776). **Essai sur une application des regles demaximiaetminimis a quelquesproblèmes de statiquerelatifsa l'architecture. Mémoires de la Mathématiqueet de Physique,présentés a l'Académie Royale des Sciences, par divers savants,** etlusdansçesAssemblées. L'Imprimérie Royale, Paris, 3–8.

González, A., Cuadrado, A., Josa, A. and Olivella, S. (2013). **Safety assessment of limit equilibrium methods for the design of cantilever and anchored sheet pile walls.** Escola de Camins, Barcelona.

Hossain, M. S., Kibria, G., Khan, M. S., Hossain, J., &Taufiq, T. (2011)**. Effects of backfill soil on excessive movement of MSE wall.** Journal of Performance of Constructed Facilities, Vol. 26, No. 6, 793-802.

Jaky, J. (1944). **"The coefficient of earth pressure at rest. In Hungarian (A nyugalminyomastenyezoje)."** J. Soc. Hung. Eng. Arch. (MagyarMernokes Epitesz-Egylet Kozlonye), 355–358.

Johansson, E. & Sandeman, E. (2014). **Modelling of Deep Excavation in Soft Clay: A comparison of different calculation methods to in situ measurements.** Chalmers University of Technology, Gothenburg, Sweden.

Lee, K.L., Adams, B.D., Vagneron, J.J. (1973), **"Reinforced earth retaining walls"**, Journal of Soil Mechanics and Foundation Division, ASCE, Vol.99, No. SM10.

R. B. Seed, R. G. Bea, A. Athanasopoulos-Zekkos, G. P. Boutwell, J. D. Bray, C. Cheung, D. Cobos-Roa, L. F. Harder Jr, R. E. S. Moss, J. M. Pestana, M. F. Riemer, J. D. Rogers, R. Storesund, X. Vera-Grunauer and J. Wartman. (2008), **"New Orleans and hurricane katrina. The 17th Street drainage canal."** Journal of Geotechnical and Geoenvironmental Engineering, ASCE, Vol. 134, 740-761.

Rankine, W. J. M. (1857). **On the stability of loose earth.** Philos. Trans. R. Soc. London, 1, 9–27.

Suksiripattanapong, C., Chinkulkijniwat, A., Horpibulsuk, S., Rujikiatkamjorn, C., & Tanhsutthinon, T. (2012). **Numerical analysis of bearing reinforcement earth (BRE) wall.** Geotextiles and Geomembranes, Vol. 32, 28-37.

Tan, Y. (2008). **Finite element analysis of highway construction in peat bog.** Canadian Geotechnical Journal, Vol. 45, No. 2, 147-160.

Gerber, E. (1929). **Untersuchungen iiber dic Druckkverteilung im Orlich belasteten Sand,** Technische Hochschule. Zurich.

Spangler, M. G. (1938). **"Horizontal Pressures on Retaining Walls Due to Concentrated Surface Loads,"** Iowa State University Engineering Experiment Station, Bulletin, No. 140.

Brooker, E. W., and Ireland, H. O.(1965)**"Earth Pressure at Rest Related to Stress History"**, Canadian Geotechnical Journal, Vol. 2, No. 1, pp. 1-15.

Budhu, M. (2000), **"Soil Mechanics and Foundations"**, John Wiley & Sons, Inc., 586p.

Coduto, D.P. (2001), **"Foundation Design: Principles and Practice"**, Prentice Hall, New Jersey.

Das, B.M. (1994), **"Principles of Geotechnical Engineering"**, 3d ed. PWS

Publishing, Boston, 672 pp.

Das, B.M. (1987), **"Theoretical Foundation Engineering"**, Elsevier, Amsterdam.

Dunn, I. S., Anderson, L. R., and Kiefer, F. W. (1980), **"Fundamentals of

Geotechnical Analysis",** John Wiley & Sons, Inc.

Lambe, T. W., and Whitman, R. V. (1969;1979), **"Soil Mechanics"**, John Wiley &

Sons, Inc., New York.

CHAPTER III

PREDICTING PULLOUT RESISTANCE OF BEARING

REINFORCEMENT EMBEDDED IN COHESIVE-

FRICTIONAL SOILS

3.1 Introduction

Mechanical stabilized earth (MSE) walls have been proven to be an effective retaining structure in infrastructure applications (Horpibulsuk et al., 2011 and Udomchai et al., 2017). The reinforcement types are classified into inextensible (i.e. steel strips and steel grid) and extensible (i.e. geotextile and geogrid) materials, depending upon the amount of deformation that occurs during loading. Both types of reinforcement minimize the horizontal movement of the MSE wall (Palmeira, 2004; Roodi Gholam and Zornberg Jorge, 2017). The reinforcement can also be placed at base of embankment on soft soil to enhance bearing capacity and reduce the settlement of foundation (Bonaparte and Christopher, 1987; Chai et al., 2002; Jewell, 1988; Zhang et al., 2015).

Bearing reinforcement (Figure 3.1 (a)) developed by Horpibulsuk and Niramitkronburee (2010) is an inextensible reinforcement type. The more detail of bearing reinforcement was proposed by Horpibulsuk and Niramitkronburee (2010). The performances of the bearing reinforcement have been examined in the large-scale laboratory testing carried with the pullout apparatus as shown in Figure 3.1 (b), field-scale testing, and numerical simulation testing. The Bearing reinforcement earth

(BRE) wall has been successfully implemented in many construction projects of Department of Highways (DOH), Department of Rural Roads and Electricity Generating Authority of Thailand. Based on AASHTO (2002) specification, the design method of MSE wall was proposed for high quality friction (coarse-grained) backfill, which specifies a fines content (<0.075 mm), F of less than 15% and a plasticity index of less than 6%.
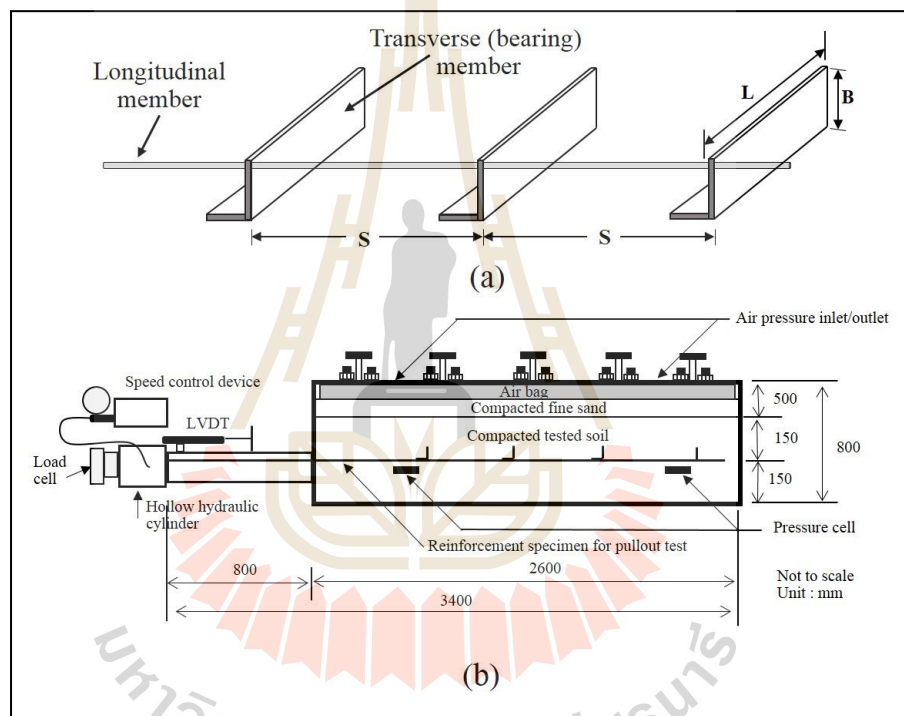
Figure 3.1 (a) Typical schematic view of the bearing reinforcement, (b) Pullout test

apparatus (Adapted from: Horpibulsuk and Niramitkornberee, 2010)

Due to economical and environmental factors, the marginal cohesive-frictional soils ($F > 15\%$) abundant in Thailand is typically used for infrastructure activities after soil improvement (Sukmak et al., 2013; Phummiphan et al., 2016; Donrak et al., 2018). In practice, the clayey soil can be used as a backfill material but the water content and relative density of the compacted backfill must be close to the optimum water content and 95% of maximum density, respectively, obtained from laboratory. Also during service, the seepage of water such as rain and ground water must be protected for the MSE wall by the provision of geotextile as a drainage layer to minimize the expansion of the backfill. The locally available clay stone were used as a backfill material for a construction the first MSE wall in the Mae Moh mine (Udomchai et al., 2017). The usage of cohesive-frictional soil as a backfill for BRE walls is challenging, as the generalized pullout resistance equations for cohesive-frictional soil at various water contents and fines contents, are not currently available. The previous studies (Sukmak et al., 2015 and Horpibulsuk et al., 2017) studied the influences of cohesive-friction soils contained with different fines contents on the pullout resistance of bearing reinforcement. However, these two research studies are only applicable for the compacted soils at the optimum water content (w_{owc}) and maximum dry unit weight. Sukmak et al. (2016) investigated the effect of moisture contents on performance of bearing reinforcement embedded in clayey sand soil ($F = 20\%$) compacted at various water contents ($w_{owc} \pm 2.5\%$).

Reanalysis of the available test results taking into account the combined effect of fines content and water content for developing generalized pullout resistance predictive equations is significant and is the focus of this research. To have a better insight, a pullout test result of red clay from this study is also analyzed. The studied

water content of red clay is in the range of $w_{owc} \pm 2.5\%$, specified for field compaction according the DOH specification. For compacted unsaturated soils, the total strength parameters used in this study are reasonable to explain the soil behavior, which are acceptable in practice (Bergado et al., 1996; Liu et al., 2009; Sukmak et al., 2016; Sukmak et al., 2015). The outcome of this study will lead to the using of in-situ cohesive-frictional soil as a backfill material for BRE walls, which can substantially reduce costs associated with long distance haulage of imported virgin materials.

3.2 Theoretical Background

The total pullout force of bearing reinforcements composes of the friction pullout force and the bearing pullout force. The friction pullout force of longitudinal member (without any transverse member), P_f, is expressed in the form of:

$$P_f = \pi D L_e \alpha (c + \sigma_n \tan \phi) \tag{3.1}$$

where α is the interaction factor, c and ϕ are cohesion and internal friction angle of compacted soil, respectively, σ_n is the applied normal stress and D and L_e are the diameter and embedded length of the longitudinal member, respectively.

The bearing pullout force, P_{bn} of the transverse members, which are placed at regular intervals, is governed by the interference of each transverse member during pullout. The bearing pullout force, P_{bn} is expressed as:

$$P_{bn} = nIFP_{b1} \tag{3.2}$$

where n is the number of transverse members, IF is the transverse members interference factor and P_{b1} is bearing pullout force of a single transverse member.

Typically, B, of the transverse members (steel equal angles) is smaller than 40 mm, while the length, L, is larger than 150 mm. The L/B value for the transverse members is therefore more than 3.7. Although during pullout of the bearing reinforcement, the deformation around the transverse member is three-dimensional (3D), previous studies (Horpibulsuk and Niramitkornburee, 2010; Suksiripattanapong et al., 2013; Sukmak et al., 2015 and Horpibulsuk et al., 2017) reported that within this B/L range, the 3D effect has been inexplicitly considered by the proposed plane strain failure model (2D). By extending the modified punching shear mechanism (Bergado et al., 1996; Chai, 1992), the P_{b1} can be determined using the following equations.

$$P_{b1} = \left[cN_c + \sigma_n N_q \right] BL \tag{3.3}$$

$$N_q = \frac{1}{\cos\phi} \exp\left[2\beta\tan\phi\right]\tan\left(\frac{\pi}{4} + \frac{\phi}{2}\right) \tag{3.4}$$

$$N_c = \frac{1}{\sin\phi} \exp\left[2\beta\tan\phi\right]\tan\left(\frac{\pi}{4} + \frac{\phi}{2}\right) - \cot\phi \tag{3.5}$$

where B and L are leg length and length of transverse member, respectively (Figure 3.1), β is the failure angle (radian).

The extensive test results reported previously (Suksiripattanpong et al., 2013; Sukmak et al., 2015 and 2016) that β was dependent upon F and water content ratio (w/w_{OWC}), where w is water content and w_{OWC} is the optimum water content. When

the β values are $\pi/1.65$ and $\pi/3$, the failure modes are general shear (Perterson and Anderson, 1980) and punching shear(Jewell et al., 1984) mechanisms, respectively, which are the upper and lower boundary limits.

The transverse members interference factor (*IF*) on the bearing reinforcement is controlled by the spacing of the transverse members *S* and *B*, regardless of *L* (Horpibulsuk and Niramitkronburee, 2010; Sukmak et al., 2016; Sukmak et al., 2015; Suksiripattanapong et al., 2013). The failure mechanism for the bearing reinforcement depends upon the spacing ratio, *S/B* as shown in Figure 3.2. The detail of classification has been reported by Sukmak et al., 2015. The block failure and the interference failure zones is separated by the S_1/B ratio. The S_2/B ratio separates the interference failure and individual failure zones. Based on the extensive past test results, S_1/B can be taken as 3.75 for a wide range of fines contents (Sukmak et al., 2015 and 2016 and Horpibulsuk et al., 2017). Sukmak et al (2015) reported that a lower shear strength results in a smaller softened region, and hence a lower S_2/B value. The *IF* is equal to $1/n$ when $S/B < S_1/B$ (block failure) and 1 when $S/B > S_2/B$ (individual failure). When $S_1/B < S/B < S_2/B$, the *IF* can be determined from logarithm of *S/B*, regardless of applied normal stress as follows.

$$IF = a + b\ln\left(\frac{S}{B}\right) \tag{3.6}$$

$$b = \frac{\left[1 - \dfrac{1}{n}\right]}{\left[\ln\left(\dfrac{S_2}{B}\right) - 1.322\right]} \tag{3.7}$$

$$a = 1 - b \ln \left(\frac{S_2}{B} \right) \tag{3.8}$$

The number and spacing of the transverse members are determined based on the internal stability design method of BRE wall suggested by Horpibulsuk and Niramitkornburee, 2010 and Suksiripattanapong et al., 2013 for coarse-grained backfill and Udomchai et al., 2017 for fine-grained backfill. The pullout resistance of each reinforcement must provide high enough capacity against pullout failure due to the dead load and live load with a minimum factor of safety of 1.5. Typically the vertical spacing of the MSE wall is 750 mm as suggested by AASHTO (2002) to have satisfactory interaction between the backfill and the reinforcements. For the BRE wall, the reinforcement is connected to the wall facing by a locking bar and the vertical spacing is 750 and 350 mm depending upon the height of BRE wall. The dimension of segmental concrete facing panels is 1.50x1.50x0.14 m. The reasonable interaction between backfill and reinforcement in BRE wall has been reported by Horpibulsuk et al. (2011) for coarse-grained backfill and Udomchai et al. (2017) for fine-grained backfill.
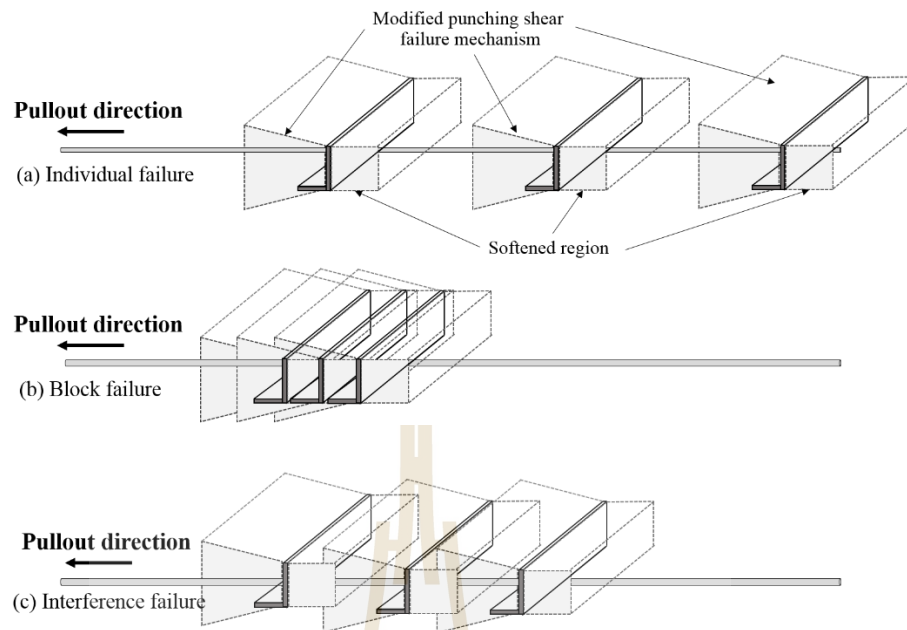
Figure 3.2 Transverse members interference (Adapted from: Sukmak et al. 2015)

3.3 Materials and Methods

Soil Samples

The tested soil was the residual red clay soil, containing 98% of fines content which was collected from the Mae Moh mine of Electricity Generating Authority of Thailand. The grain size distribution curve of red clay shows in Figure 3.3(a). The red clay was classified as a low-quality soil and as a high plasticity clay (CH) according to the Unified Soil Classification System (USCS).

The compaction characteristic under standard Proctor energy (ASTM D698-91, 1995) was $w_{OWC} = 16\%$ and maximum dry unit weight, $\gamma_{d,\max} = 17.61$ kN/m^3. The soil samples were prepared according to Sukmak et al. 2016a for both direct shear and pullout tests at five different molding water contents, w, which were on the dry side of optimum ($w_1 = 12\%$ and $w_2 = 14\%$), at w_{owc} ($w_3 = 16\%$), and on the wet side of

optimum ($w_4 = 18\%$ and $w_5 = 20\%$)as shown in Figure 3.3(b). The degrees of saturation, S_r, corresponding to w_1, w_2, w_3, w_4, and w_5 were 59%, 70%, 83%, 85%, and 88%, respectively.

A large direct shear device with a dimension of 305 mm x 305 mm x 240 mm depth were used to investigate the total strength parameters. The detail of the test has been reported by Sukmak et al. (2015). The red clay samples were prepared at the required water contents (w_1, w_2, w_3, w_4, and w_5) and at their corresponding dry unit weight. The physical and engineering properties are summarized in Table 3.1.
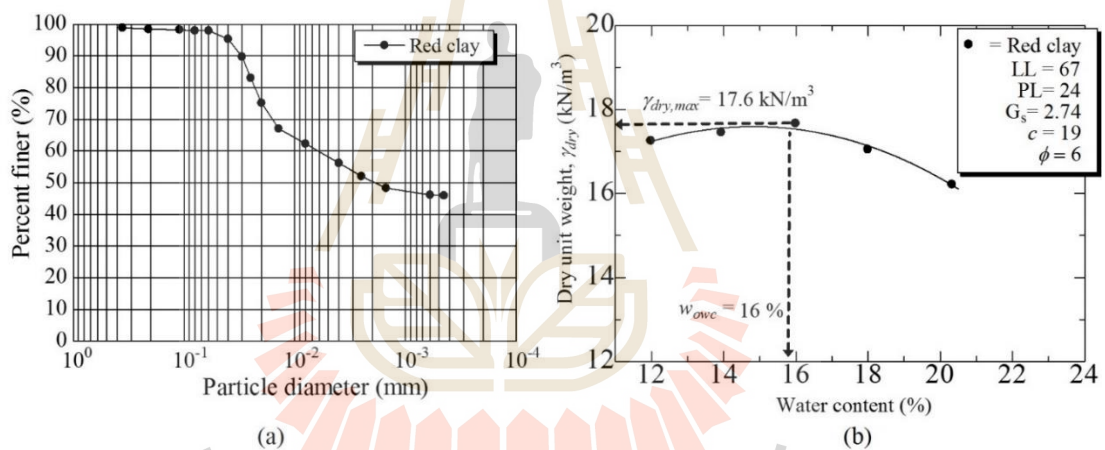
Figure 3.3 (a) Grain size distribution of red clay, (b) Compaction curve of red clay.

Table 3.1: Physical and engineering properties of red clay.

Properties of red clay	w_1	w_2	w_3	w_4	w_5
Dry density, γ_{dry} (kN/m^3)	17.25	17.40	17.60	17.00	15.85
Water content (%)	12	14	16	18	20
Degree of saturation, S_r (%)	59	70	83	85	88
Relative degree of compaction (%)	96.36	98.63	100	98.63	96.36
Water content ratio	0.75	0.88	1.00	1.13	1.25
Angle of internal friction, ϕ	13	11	6	5	4
Cohesion, c (kPa)	22	21	19	14	8

Bearing Reinforcement

The leg length, *B*, of the tested transverse members (steel equal angles) were 25, 40, and 50 mm, while the length, *L*, were 100 and 150 mm, respectively, which are typical to those used for BRE walls. The spacing between the transverse members, *S*, varied from 150 to 1500 mm, depending upon the number of transverse members, *n*. In this study, the *n* was 1 to 4, which is typical in practice. The longitudinal and transverse members were strongly welded together according to the American Institute of Steel Construction (AISC).

Methodology

The detail of the pullout test apparatus and the procedure of the pullout testing have been explanted by Horpibulsuk and Niramitkronburee (2010). The soil was compacted with a vibratory compactor until the maximum dry unit weight was attained. A compacted soil thickness of 300 mm was maintained above and below the reinforcement (Figure 3.1(b)). The pullout tests were conducted at a pullout rate of 1.0 mm per minute as recommended by Sukmak et al. (2015) for unsaturated soils. At

least three samples were tested under the same conditions to assure consistency of the test results. In most cases, the results under the same testing conditions were reproducible with a low mean standard deviation, SD (SD/$\overline{x}$ < 10%, where $\overline{x}$ is mean strength value). Besides the red clay, the data from previous research (Sukmak et al., 2015 and 2016 and Horpibulsuk et al., 2017) were taken and reanalyzed to develop the generalized equations for assessing pullout resistance at various water contents and fines contents.

3.4 Test Results and Discussion

Shear strength of compacted backfills

Figure 3.4 shows the effect of w and F on undrained shear strength of red clay compared with other cohesive-frictional soils. Figure 3.4(a) summaries the change in shear strength and F for clayey sands compacted at their w_{OWC}. It was evident that $F = 45\%$ was the threshold limit that the shear strength sharply decreases with F. The change of shear strength with F was relatively small when $F < 45\%$ but was significantly larger when $F > 45\%$. The large decrease in shear strength was clearly noted with higher normal stress. The sudden change in shear strength when $F > 45\%$ is because at this condition, the fines particles fill the void spaces between the coarse particles and dominate the coarse-grained behaviour (Wang et al. 2009). The large amount of fines particles cause the slippage and sliding of coarse grain particles over each other. The shear strengths therefore drop with an addition of fine content due to the decrease of internal friction angle.

Figure 3.4 (b) and (c) show the relationships between shear strength and water content ratios (w / w_{owc}) for lateritic soil ($F = 20.3\%$) and red clay ($F = 98\%$)

compacted at various water contents, respectively. The shear strength of both soils decreased with increasing water content ratio. The reduction in shear strength was small for low F (Figure 3.4(b)) but very large for high F (Figure 3.4(c)). The linear relationship between shear strength and w/w_{owc} was observed for red clay. This understanding of shear strength change is essential for BRE wall design, as the shear strength controls the pullout resistance.
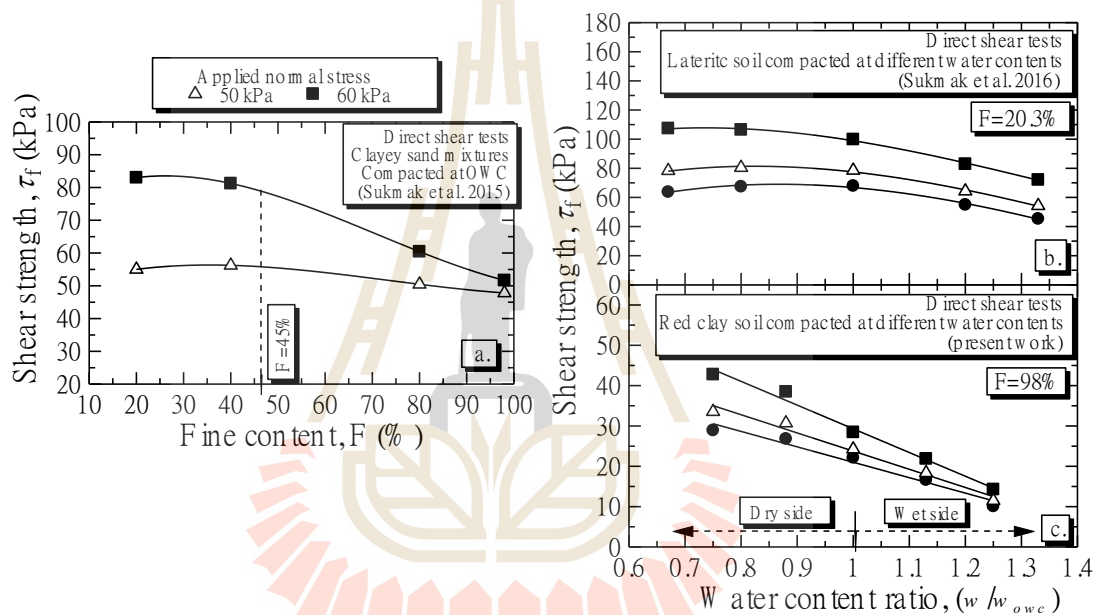
Figure 3.4 (a) Relationship between shear strength versus fine content of compactedsoils at optimum water content (Data from: Sukmak et al. 2015), (b) relationships between shear strength and water content ratios (w/w_{owc}) of lateritic soil (Data from: Sukmak et al. 2016), (c) relationships between shear strength and water content ratios (w/w_{owc}) of red clay

Friction pullout resistance

Figure 3.5 illustrates the results of the pullout friction tests on a longitudinal member bar with a diameter of 16 mm and a length of 2600 mm embedded in red clay. The friction force increased with the pullout displacement until the peak friction pullout force, $P_{f\text{peak}}$ was reached and subsequently reduced to the end of test of 40 mm. The friction pullout force at the end of test is herein defined as the residual friction pullout force, $P_{f\text{residual}}$. The displacement corresponding to $P_{f\text{peak}}$ was 3-5 mm for all applied normal stresses. The $P_{f\text{peak}}$ and $P_{f\text{residual}}$ increased with an increase of the normal stress and depended upon the water content. The $P_{f\text{peak}}$ and $P_{f\text{residual}}$ values significantly reduced with increasing water content because of the significant reduction in shear strength (see Figure 3.4c).

Figure 3.6 shows the relationships between the interface shear strength versus shear strength of the compacted soil. From a linear regression analysis, the peak and residual interaction factors (α_p and α_r) of red clay ($F = 98\%$) were 0.66 and 0.47, respectively for all water content tested. These values are close to those ($\alpha_p = 0.63$ and $\alpha_r = 0.46$) reported by Sukmak et al. (2015) for high plasticity clay (CH and $F = 98\%$). Based on this present work and previous research (Sukmak et al., 2015 and Horpibulsuk et al., 2017), the α_p and α_r for a particular soil are constant with water contents. Sukmak et al. (2016) have proposed a relationship between α_p and α_r versus F as follows:

$$\alpha_p = -0.002F + 0.859 \qquad \text{for } 20 < F < 98\% \qquad (3.9)$$

$$\alpha_r = -0.0014F + 0.592 \qquad \text{for } 20 < F < 98\% \qquad (3.10)$$

Both equations are recommended as a quick tool for predicting α_p and α_r at various fines contents and water contents.
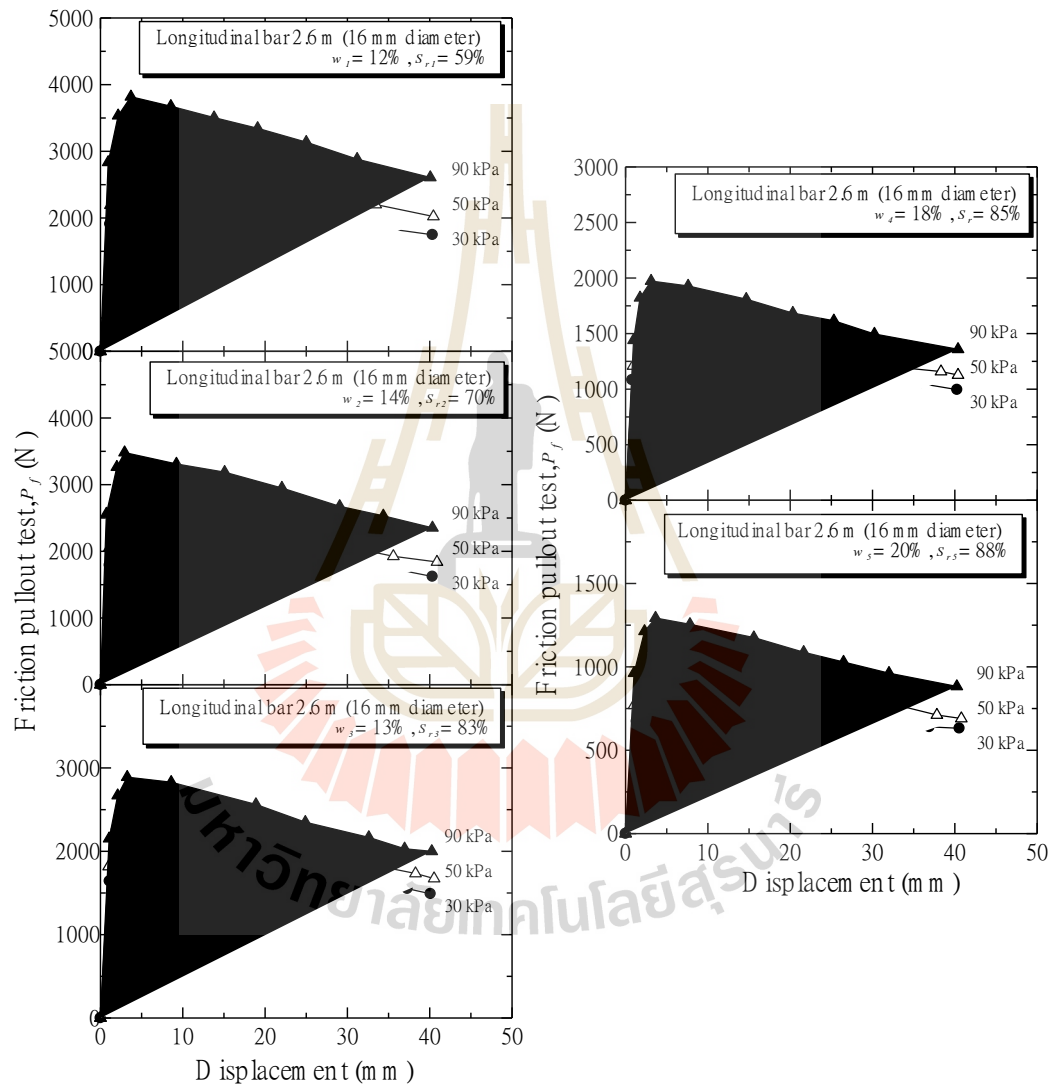
Figure 3.5 Pullout test results of a longitudinal member under different normal stresses.
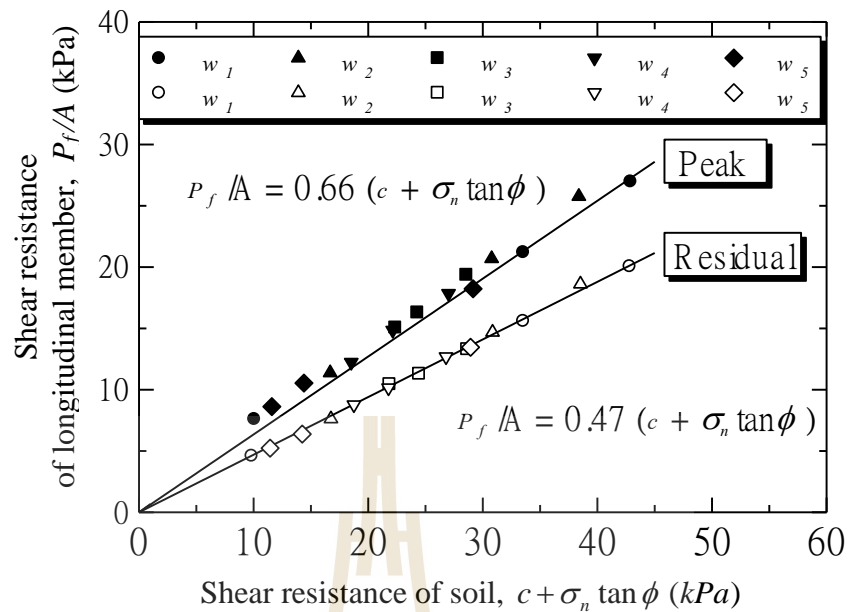
Figure 3.6 Relationship between shear interface and shear strength.

Bearing pullout resistance

Bearing pullout resistance of a single isolated transverse member (n = 1)

The measured maximum bearing stress, σ_{bmax}, of a single transverse member for the red clay, with various dimensions (B and L) of transverse member and normal stresses is shown in Figure 3.7. By using the generalized equation (Eqs. (3.3)-(3.5)) to predict σ_{bmax}, the β value of $\pi/3$ can satisfactorily fit all the test data both on the dry and the wet sides of optimum of compacted red clay. This implied that the failure mechanism of the bearing reinforcement in red clay was punching shear for all water contents on both dry and wet sides of optimum. With the same punching shear failure mode and the significant reduction in shear strength with increasing water content, the bearing pullout resistance essentially decreased with addition of water content.

The analysis of the present and previous data (Sukmak et al., 2015 and 2016 and Horpibulsuk et al., 2016) leads to the 3 dimensional plot of β versus F and w/w_{OWC} as shown in Figure 3.8. The plot was made from the three assumptions.

1. At $w = w_{OWC}$, $F = 45\%$ is the threshold limit separating small and large change in bearing pullout resistance with F (Sukmak et al., 2015).

2. On the dry side of optimum and at w_{OWC}, the β is identical and can be determined from the following equation (Sukmak et al., 2015):

$$\beta_{(rad)} = \left[-0.00002F^2 + 0.0002F + 0.505 \right] \pi \qquad \text{for } 20 < F < 98\% \qquad (3.11)$$

3. On the wet side of optimum, β reduces significantly with increasing w/w_{OWC} until $\beta = \pi/3$ (punching shear) at $w/w_{OWC} = 1.33$ (Sukmak et al., 2016; Horpibulsuk et al., 2017 and present data). Therefore the β at any w/w_{OWC} can be approximated using interpolation method where the β at $w/w_{OWC} = 1$ can be determined from Eq. (3.11).

With the known β value determined from Figure 3.8, the P_{b1} can be determined using Eqs. (3.3) to (3.5).
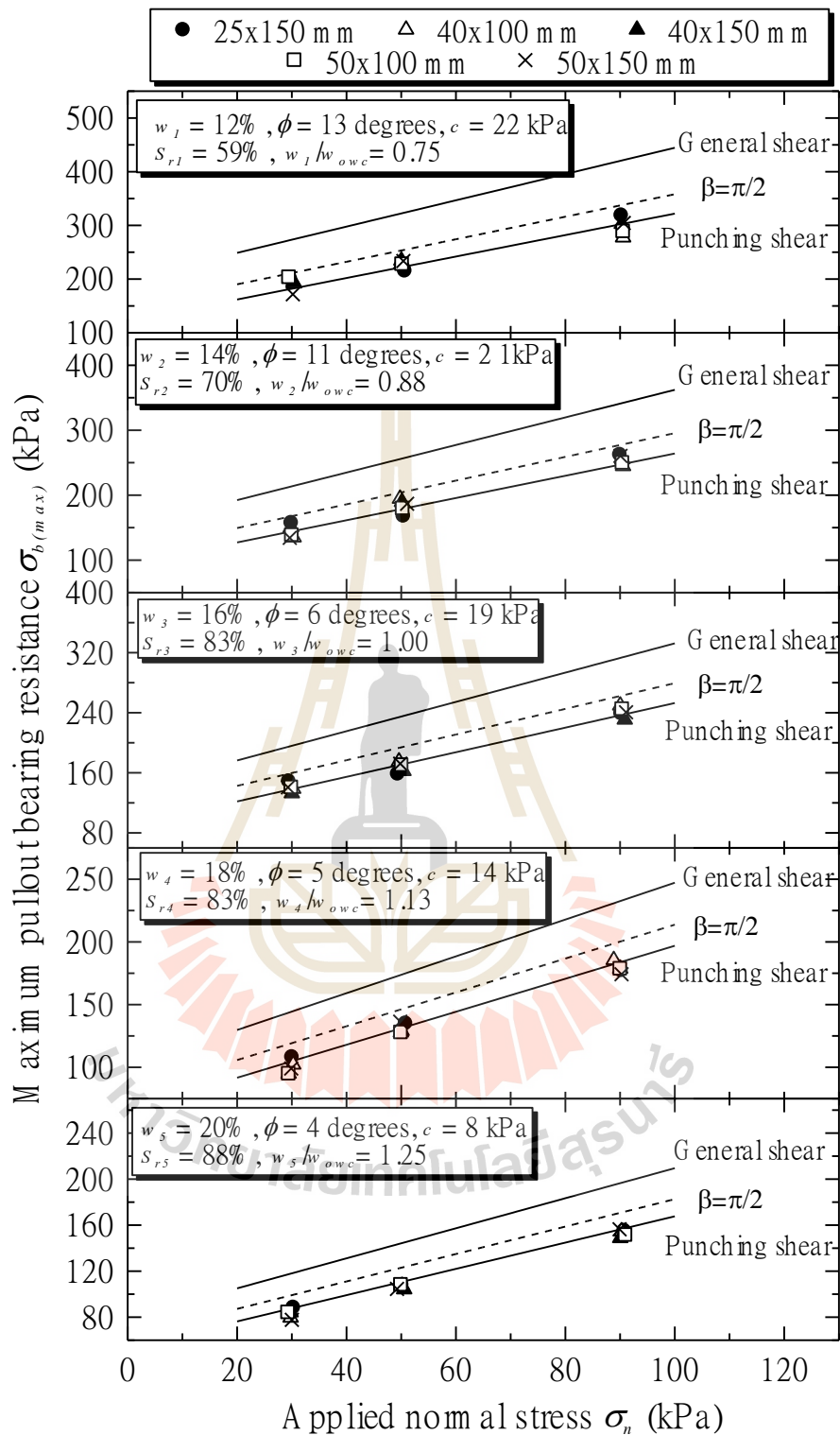
Figure 3.7 Maximum pullout bearing resistance of a single isolated transverse member at various water contents.
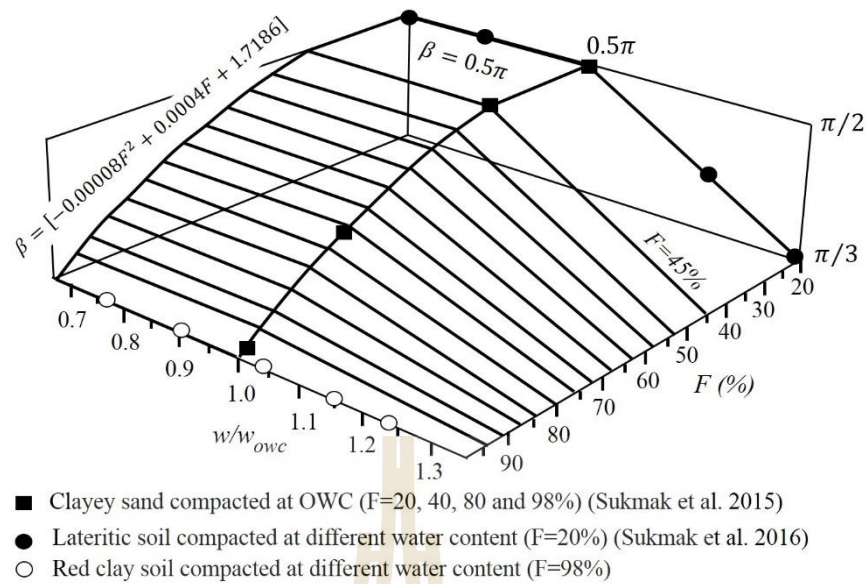
Figure 3.8 Plot of β versus F and w/w_{OWC} (Data from: Sukmak et al. 2015 and 2016)

Bearing pullout resistance of the bearing reinforcement (n > 1)

Figure 3.9 illustrates the relationship between *IF* and *S/B* at various w/w_{OWC} and *n* for red clay. It was evident that the S_1/B value was essentially the same of 3.75 for all *w* and *n* tested, which agrees with previous studies (Sukmak et al., 2015 and 2016 and Horpibulsuk et al. 2016). The S_2/B value was essentially the same of 13.3 for $w \le w_{OWC}$, whereas the S_2/B value for $w > w_{OWC}$ decreased linearly with increasing water content. The analysis of the previous and present studies resulted in the three dimensional plot of S_2/B versus F and w/w_{OWC} as shown in Figure 3.10. The following assumptions were made for the development of Figure 3.10.

(i) At $w/w_{OWC} = 1$, S_2/B can be determined using the following equation proposed by Sukmak et al. (2015).

$$(S_2 / B)_{OWC} = -0.121F + 25.16 \tag{3.12}$$

(ii) On the dry side and at w_{OWC}, the S_2/B is identical and can be approximated using Eq. (3.12).

(iii) On the wet side, the relationship between S_2/B and w/w_{OWC} at a given F can be determined from

$$(S_2 / B)_F = c(w / w_{OWC}) + d \tag{3.13}$$

where c and d are constant. The c values are -30.7 and -12.81 for $F = 20\%$ and 98%, respectively. The c values at various F can thus be approximated from an interpolation using c values at $F = 20\%$ and 98%. The d value can be calculated from the known S_2/B value at $w/w_{OWC} = 1$ determined by Eq. (3.12).

Once S_2/B is known, IF can be determined using Eq. (3.6) to (3.8). Therefore, the P_{bn} at various S/B and n can be determined from Eq. (3.2).
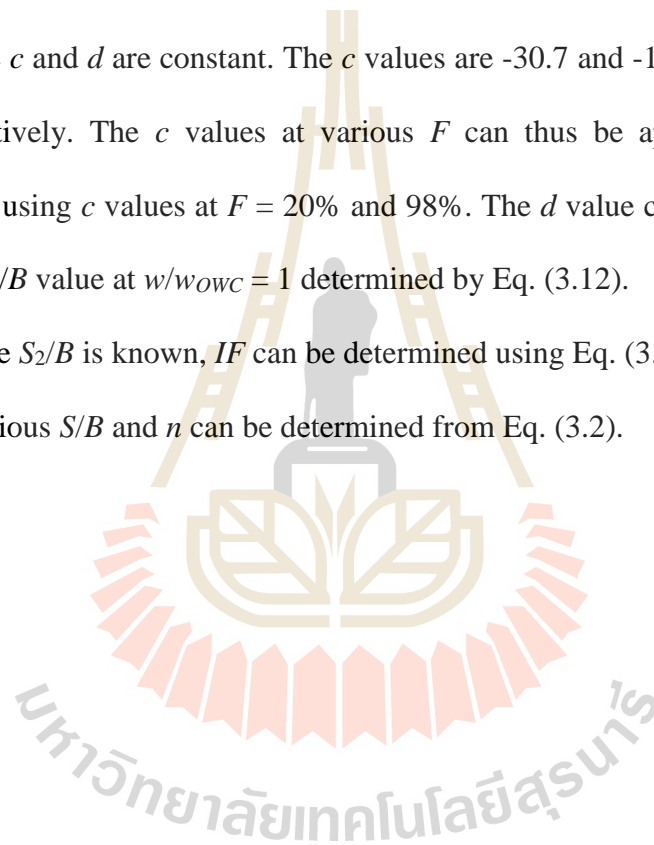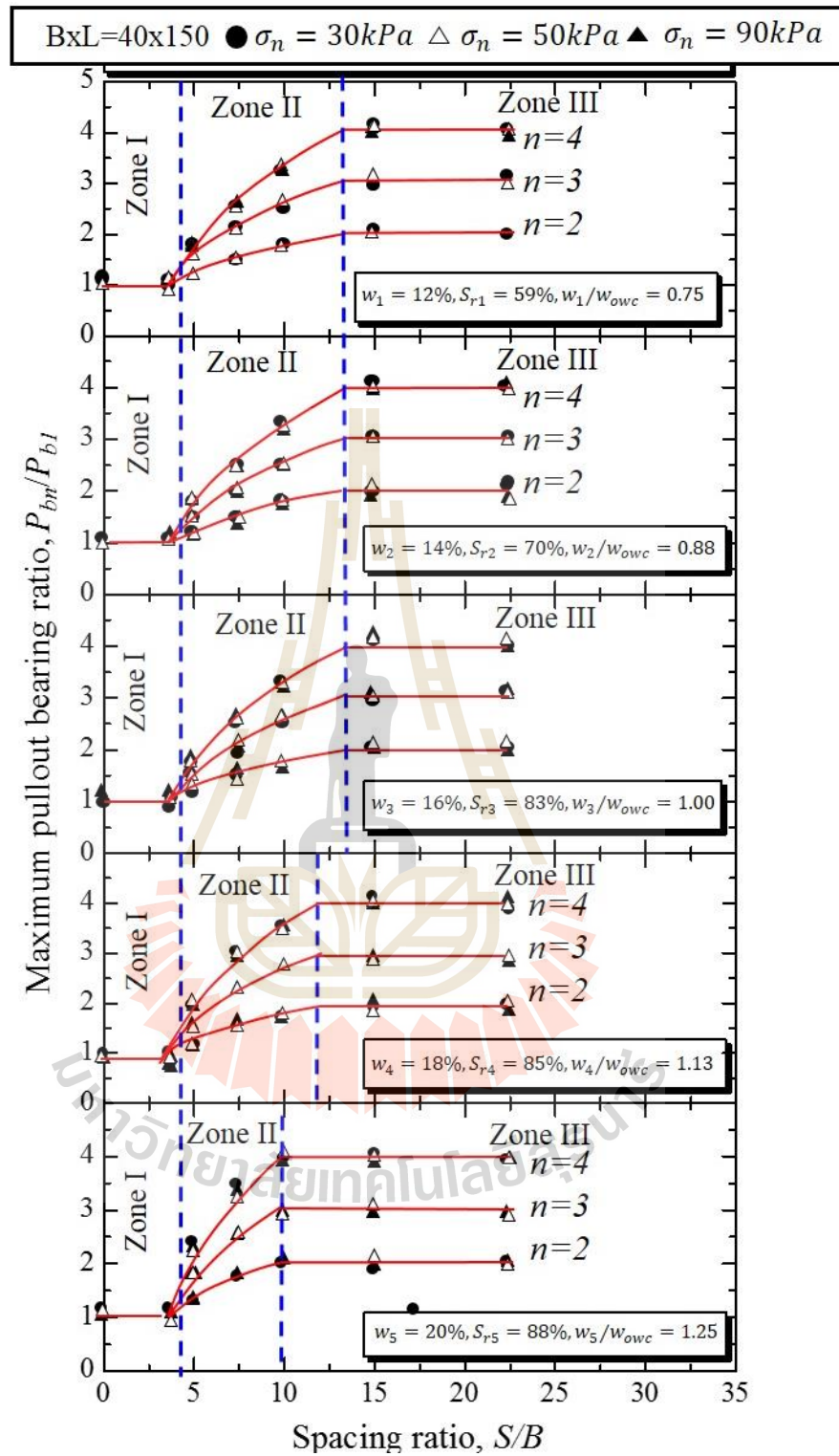
Figure 3.9 *IF* and *S/B* relationship for 40x150 mm transverse members (zone I: block failure, zone II: interference failure, and zone III: individual failure)
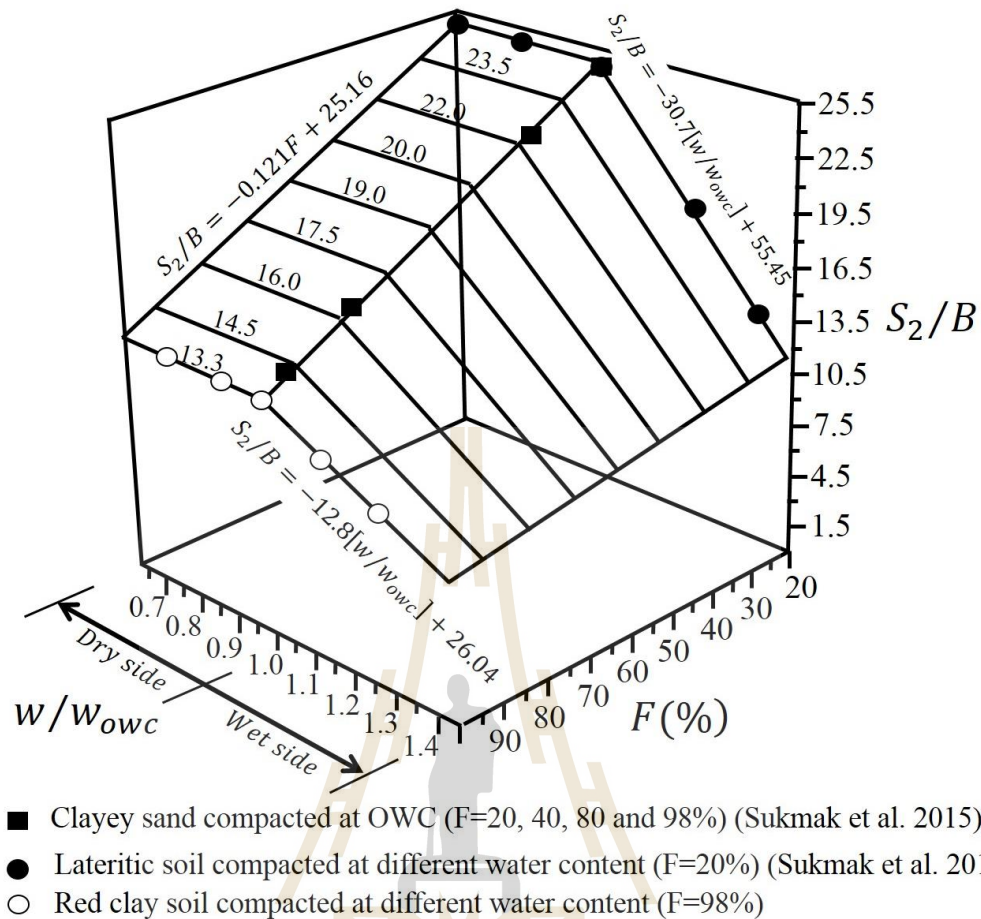
Figure 3.10 Plot of S_2/B versus F and w/w_{OWC} (Data from: Sukmak et al. 2015 and 2016)

3.5 Recommended Method for Predicting Pullout Resistance

A stepwise procedure for assessing pullout bearing resistance with transverse members, n of 1 to 4 for various water contents and fines contents is proposed as follows:

Determine the friction pullout resistance of the bearing reinforcement

1. Perform sieve, compaction and direct shear tests on the backfill material to determine F, w_{OWC} and shear strength parameters.

2. Determine α for the friction pullout resistance, which can be directly obtained from a pullout test on a longitudinal member or approximated from Eq. (9).

3. Determine the maximum pullout friction force of longitudinal member at required normal stress level from Eq. (1).

Determine the bearing pullout resistance of the bearing reinforcement

4. Determine β at required w and F using Figure 8.

5. Determine the N_c and N_q values using Eqs. (4) and (5).

6. Determine P_{b1} from $P_{b1} = N_q \sigma_n BL$.

7. Determine the S_2/B using Figure 9.

8. Determine IF of the required transverse members (required n, S, B, and L). Eqs.(6) to (8) are used when $S_1/B < S/B < S_2/B$.

9. Determine the maximum pullout bearing force with n transverse members, P_{bn} from $P_{bn} = nIFP_{b1}$.

Determine the pullout resistance of the bearing reinforcement

10. Determine the pullout resistance = $P_f + P_{bn}$.

3.6 Conclusions

This research investigated the combined effects of fines and water contents on the pullout resistance of bearing reinforcement embedded in the cohesive-frictional soils. The previous and present test results were analyzed to develop the generalized pullout resistance predictive equations at various water contents and fines contents. The following conclusions can be drawn from this study:

1) The total pullout resistance of the bearing is the sum of friction pullout and bearing pullout resistances. The lower water content resulted in the higher shear strength; hence the higher pullout friction resistance. The peak and residual interaction factors (α_p and α_r) value were dependent upon F, irrespective of water contents. The relationships between α_p and α_r versus F were suggested in this paper. The relationships between α_p and α_r versus F are $\alpha_p = -0.002F + 0.859$ and $\alpha_r = -0.0014F + 0.592$, respectively.

2) The bearing pullout resistance of transverse members P_{bn} is calculated in terms of the number of transverse members (n), transverse members interference factor (IF) and pullout bearing resistance of a single transverse member P_{b1}. The IF and P_{b1} were found to be primarily controlled by F and w/w_{OWC}. The 3-dimensional plot of β versus w/w_{OWC} and F in the range of $0.67 \leq w/w_{owc} \leq 1.33$ and $20 < F < 98\%$ are proposed to determine P_{b1}. On the dry side of optimum and at w_{OWC}, the β of $\pi/2$ is recommended for $F < 45\%$. On the wet side of optimum, β reduces significantly with increasing w/w_{OWC} and F until $\beta = \pi/3$ at $w/w_{OWC} = 1.33$.

3) The 3-dimensional plot of S_2/B versus w/w_{OWC} and F in the range of $0.67 \leq w/w_{owc} \leq 1.33$ and $20 < F < 98\%$ are proposed to determine IF. The S_2/B value was essentially the same of 13.3 for $w \leq w_{OWC}$, whereas the S_2/B value for $w > w_{OWC}$ decreased linearly with increasing water

content. Using the relationship between β versus F and w and the relationship between IF versus F and w, the P_{bn} can be calculated.

4) The method of predicting pullout resistance of bearing reinforcement embedded in cohesive-frictional soils were proposed in this research. The proposed method is useful for examination of internal stability of BRE wall during construction and at the end of construction. The development of this generalized pullout resistance predictive equations for the bearing reinforcement is based on sound principle. The framework can be extended to develop pullout resistance predictive equations of other reinforcement systems for further study.

3.7 Reference

AASHTO. 2002. **Standard specifications for highway bridges.** 17th ed. Washington, DC: AASHTO.

ASTM. 1995. **Test method for laboratory compaction characteristics of soil using standard effort (12,400 ft-lbf = ft³ (600 kN-m/m³)).** ASTM D698-91. West Conshohocken, PA: ASTM.

Bergado, D. T., J. C. Chai, and H. Marui. 1996. **"Prediction of pullout resistance and pullout force displacement relationship for inextensible grid reinforcements."** Soils Found. 36 (4): 11–22.
https://doi.org/10.3208/sandf.36.4_11

Bonaparte, R., and B. R. Christopher. 1987. **"Design and construction of reinforced embankments over weak foundations."** Transp. Res. Rec.1153 (1): 26–39.

Chai, J. C., N. Miura, and S. L. Shen. 2002. **"Performance of embankments with and without reinforcement on soft subsoil."** Can. Geotech. J. 39 (4): 838–848. https://doi.org/10.1139/t02-033.

Donrak, J., S. Horpibulsuk, A. Arulrajah, H. Kao, A. Chinkulkijniwat, and M.Hoy. 2018. **"Wetting-drying cycles durability of cement stabilised marginal lateritic soil/melamine debris blends for pavement applications."** Road Mater. Pavement Des. https://doi.org/10.1080/14680629.2018.1506816.

Horpibulsuk, S., and A. Niramitkronburee. 2010. **"Pullout resistance of bearing reinforcement embedded in sand."** Soils Found. 50 (2): 215–226. https://doi.org/10.3208/sandf.50.215.

Horpibulsuk, S., C. Suksiripattanapong, A. Niramitkornburee, A. Chinkulkijniwat, and T. Tangsutthinon. 2011. **"Performance of earth wall stabilized with bearing reinforcements."** Geotext. Geomembr. 29 (5): 514–524. https://doi.org/10.1016/j.geotexmem.2011.05.002.

Horpibulsuk, S., A. Udomchai, A. Joongklang, A. Chinkulkijniwat, N. Mavong, A. Suddeepong, and A. Arulrajah. 2016. **"Pullout resistance mechanism of bearing reinforcement embedded in residual clayey soils."** Geosynthetics Int. 24 (3): 255–263.

Jewell, R. A. 1988. **"The mechanics of reinforced embankments on soft soils."** Geotext. Geomembr. 7 (4): 237–273. https://doi.org/10.1016/0266-1144(88)90001-5.

Jewell, R. A., G. W. E. Milligan, R. W. Sarsby, and D. Dubois. 1984. **"Interaction between soil and geogrids."** In Proc., Symp. on Polymer Grid Reinforcement in Civil Engineering, 11–17. London: Thomas Telford.

Jiang, Y., J. Han, R. L. Parsons, and J. J. Brennan. 2016. **"Field instrumentation and evaluation of modular-block MSE walls with secondary geogrid layers."** J. Geotech. Geoenviron. Eng. 142 (12): 05016002. https://doi.org/10.1061/(ASCE) GT.1943-5606.0001573.

Liu, C. N., Y. H. Ho, and J.W. Huang. 2009. **"Large scale direct shear tests of soil/PET-yarn geogrid interfaces."** Geotext. Geomembr. 27 (1): 19–30. https://doi.org/10.1016/j.geotexmem.2008.03.002.

Liu, H. 2012. **"Long-term lateral displacement of geosynthetic-reinforced soil segmental retaining walls."** Geotext. Geomembr. 32 (Jun): 18–27. https://doi.org/10.1016/j.geotexmem.2011.12.001.

Mohamed, S. B. A., K.-H. Yang, and W.-Y. Hung. 2013. **"Limit equilibrium analyses of geosynthetic-reinforced two-tiered walls: Calibration from centrifuge tests."** Geotext. Geomembr. 41 (Nov): 1-16. https://doi. org/10.1016/j.geotexmem. 2013.08.004.

Palmeira, E. M. 2004. **"Bearing force mobilisation in pull-out tests in geogrids."** Geosynthetics Int. 22 (6): 481–509.

Perterson, E. M., and L. R. Anderson. 1980. **Pullout resistance of welded wire mats embedded in soil.** Research Rep. Logan, UT: Dept. of Civil and Environmental Engineering, Utah State Univ.

Phummiphan, I., S. Horpibulsuk, T. Phoo-ngernkham, A. Arulrajah, and S. L. Shen. 2016. **"Marginal lateritic soil stabilized with calcium carbide residue and fly ash geopolymers as a sustainable pavement basematerial."** J. Mater. Civ. Eng. 29 (2): 04016195. https://doi.org/10.1061/(ASCE)MT.1943-5533.0001708.

Roodi, G. H., and J. G. Zornberg. 2017. **"Stiffness of soil-geosynthetic composite under small displacements. II: Experimental evaluation."** J. Geotech. Geoenviron. Eng. 143 (10): 04017076. https://doi.org/10.1061/(ASCE) GT.1943-5606.0001769.

Sukmak, K., P. Sukmak, S. Horpibulsuk, A. Chinkulkijiniwat, A. Arulrajah, and S. L. Shen. 2016. **"Pullout resistance of bearing reinforcement embedded in marginal lateritic soil at molding water contents."** Geotext. Geomembr. 44 (3): 475–483. https://doi.org/10.1016/j.geotexmem.2015.07.01.

Sukmak, K., P. Sukmak, S. Horpibulsuk, J. Han, S. L. Shen, and A. Arulrajah. 2015. **"Effect of fine content on the pullout resistance mechanism of bearing reinforcement embedded in cohesive-frictional soils."** Geotext. Geomembr. 43: 107–117. https://doi.org/10.1016/j.geotexmem.2014.11.010.

Sukmak, P., S. Horpibulsuk, and S. L. Shen. 2013. **"Strength development in clay-fly ash geopolymer."** Constr. Build. Mater. 40 (Mar): 566–574. https://doi.org/10.1016/j.conbuildmat.2012.11.015.

Suksiripattanapong, C., S. Horpibulsuk, A. Chinkulkijniwat, and J. C. Chai. 2013. **"Pullout resistance of bearing reinforcement embedded in coarsegrained soils."** Geotext. Geomembr. 36 (Feb): 44–54. https://doi.org/10 .1016/j.geotexmem.2012.10.008.

Udomchai, A., S. Horpibulsuk, C. Suksiripattanapong, N. Mavong, R. Rachan, and A. Arulrajah. 2017. **"Performance of the bearing reinforcement earth wall as a retaining structure in the Mae Moh mine."** Geotext. Geomembr. 45 (4): 350–360. https://doi.org/10.1016/j.geotexmem.2017.04.007.

Wang, S., D. Chan, and K. C. Lam. 2009. **"Experimental study of the effect of fines content on dynamic compaction grouting decomposed granite of Hong Kong."** Constr. Build. Mater. 23 (3): 1249–1264. https://doi.org/10.1016/j. conbuildmat.2008.08.002.

Zhang, N., S. L. Shen, H. N. Wu, J. C. Chai, and Z. Y. Yin. 2015. **"Evaluation of performance of embankments with reinforcement on PVD-improved marine clay."** Geotext. Geomembr. 43 (6): 506–514. https://doi.org/10.1016/j. geotexmem.2015.05.005.

CHAPTER IV

PERFORMANCE OF THE BEARING REINFORCEMENT EARTH WALL AS A RETAINING STRUCTURE IN THE MAE MOH MINE, THAILAND

4.1 Introduction

Mae Moh mine is located in the Mae Moh district, Lampang province, Thailand. This mine is operated by the Electricity Generating Authority of Thailand (EGAT) and is reputably the largest open-pit lignite mine in Southeast Asia. The lignite is consumed approximately 45,000 tons/day (16 million tons/year), which represent 70% of the total coal production of Thailand. The current Mae Moh pit covers an area of 4 km by 7.5 km and is up to 490 m deep at certain locations. The excavated lignite is crushed into small, suitably-sized particles for electricity generation, with the use of an onsite crusher plant. The crushed lignite is subsequently transferred to the power plant by a conveyor system (Figure 4.1). The onsite crusher plant is composed of a crusher plant, truck ramp and natural slope. The excavated lignite is hauled by a truck to be crushed in the crusher plant through the truck ramp supported on a stable slope. Ideally, a crusher plant must be located close to the excavated lignite open pit to minimize haulage costs. The haulage cost rate increases by more than 150 million baht (approximately 4.3 million US dollars) per year, for each 1 km distance the crusher plant is away from the open pit. Instead of relying on the natural slope as the truck ramp support, which is often a large distance away for

the open pit, a Mechanically Stabilized Earth (MSE) wall alternative was proposed as a vertical temporary structure close to the open pit. This concept was adopted by the Mae Moh mine authorities. MSE wall has been successfully applied in many earth structures with various types of reinforcements such as basal geotextile (Zhang et al., 2015), hexagonal wire mesh (Voottipruex and Bergado, 1996), geosynthetics (Athanasapoulos, 1993; Bathurst et al., 2005; Skinner and Rowe, 2005; Mcgown et al., 1998), grids (Alfaro et al., 1997) and bearing reinforcement (Horpibulsuk et al., 2011).

The bearing reinforcement system was initially developed as an inextensible reinforcement in Thailand by Horpibulsuk and Niramitkornburee (2010). It is a relatively cost-effective reinforcement system whose advantages include: availability of raw materials, simple and fast installation, convenient transportation, and high pullout and rupture resistances with a less required steel volume. The configuration of the bearing reinforcement is shown in Figure 4.2. It is composed of a combination of a longitudinal member and several transverse (bearing) members. The longitudinal member comprises a deformed steel bar while the transverse members are a set of equal steel angles, which produce high pullout bearing resistance. The bearing reinforcement is connected to the wall facing panel at the tie point (2 U shape steel) by a locking bar (a deformed bar) (Figure 4.3). This reinforcement has been introduced into industry practice in Thailand since 2008. Several BRE walls have been constructed in several different regions of Thailand; namely in the north, northeast, and south of the country. The BRE wall design method with coarse-grained fill materials (< 15% fine content) has been developed based on laboratory and full-

scale tests (Horpibulsuk et al., 2011; and Suksiripattanapong et al., 2012, 2013 and 2016).

The MSE wall utilizing the bearing reinforcement as earth reinforcement, designated as Bearing Reinforcement Earth (BRE) wall (Horpibulsuk et al., 2011) was approved by the Mae Moh mine authorities as a temporary truck support. Residual claystone was considered as the backfill material for the BRE wall for economical and environmental reasons. The use of fine-grained soil as a backfill was a challenging aspect in the project due to limited research to date and available design protocols. The BRE wall was designed to support the weight of the truck ramp and also to provide a 90 degree slope to allow shorter access for the large mine haul trucks. The BRE wall system provides a more optimum performance than a natural slope in terms of lower unit cost of electrical generation, lower total and differential settlement and higher slope stability. In addition, due to the vertical slope of the BRE wall, more service and maintenance space is available between the crusher plant and BRE wall (Figure 4.4).

The laboratory-scale pullout resistance mechanism and predictive equations in term of vertical stress, dimension, spacing and number of transverse members for cohesive-frictional soils were recently investigated by Sukmak et al. (2015 and 2016a and Horpibulsuk et al., 2016). Sukmak et al. (2016b) performed numerical sensitivity analysis of BRE wall with various fine-grained backfills to evaluate the effect of fines content on the lateral wall movement. However, this earlier research has not been practically applied to any real construction projects to date, due to the lack of any available international code of practice and design guidelines for designing BRE wall with fine-grained backfill materials.

In this research, a full-scale instrumented BRE wall was constructed using claystone backfill in the Mae Moh mine as a truck ramp support for an on-site crusher plant. The performance of the BRE wall was analyzed to propose a practical design method for future BRE walls in the Mah Moh mine. The performance of the BRE wall after the completion of construction and during the service period included settlement, bearing stress, lateral movement, lateral earth pressure and tension force in the reinforcements. This research on BRE walls in a challenging work environment required the use of innovative techniques from engineering, economic and environmental perspectives.

Figure 4.1 Typical on-site crusher plant at the Mae Moh mine.

In this study
B = 50 mm
L = 180 mm
S = 750 mm

Longitudinal bar

Bearing plate

B

B

S

S

Welded connection

L

B

L

B
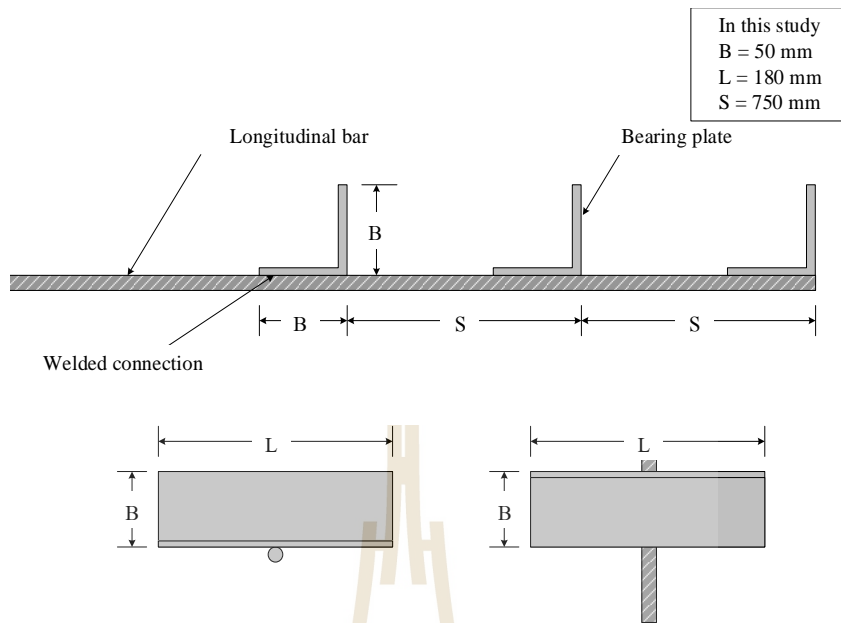
Figure 4.2 Configuration of the bearing reinforcement.

U-SHAPE REINFORCMENT
LOCKING BAR

U-SHAPE REINFORCMENT
LOCKING BAR

U-SHAPE REINFORCMENT
LOCKING BAR

WALL FACING
PANEL

U-SHAPE REINFORCMENT

LONGITUDINAL BAR

LOCKING BAR
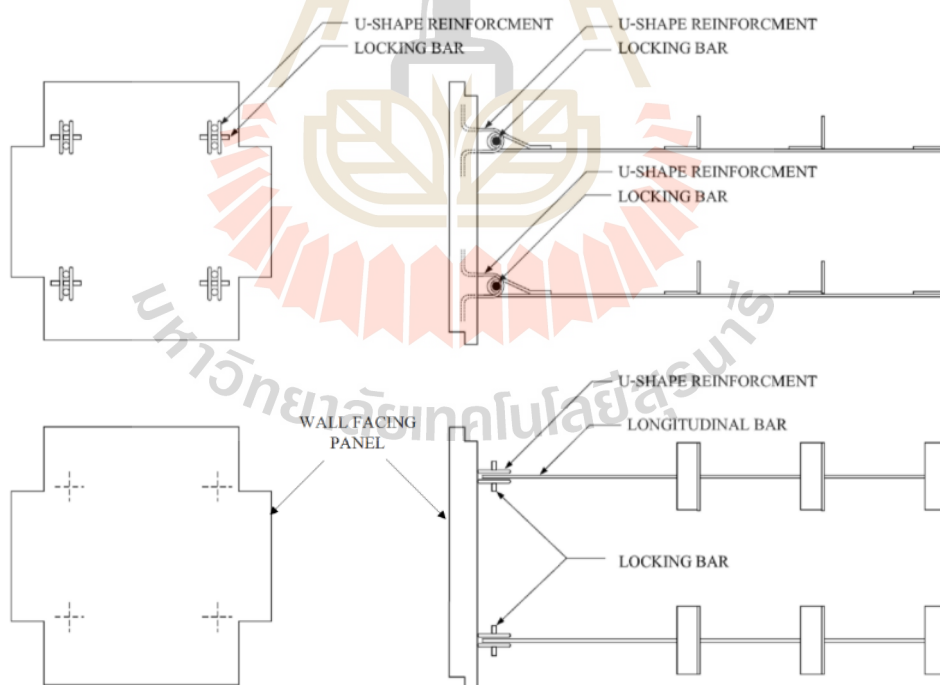
Figure 4.3 Connection of the bearing reinforcement to wall facing.

Figure 4.4 Photo of the BRE wall as a truck ramp support.

4.2   Full-scale test earth wall

4.2.1   Backfill

The backfill soil used for constructing the BRE wall was claystone, which was abundantly available at the Mae Moh mine. The claystone can be classified as a high plasticity silt (MH), according to the Unified Soil Classification System (USCS). Its specific gravity was 2.67. The liquid limit and plastic limit were 54% and 36%, respectively. The laboratory compaction characteristics under standard Proctor energy (ASTM D 698-91, 1995) was an optimum water content of 29.6% and a maximum dry unit weight of 13.6 kN/m^3. Direct shear tests were conducted to determine the total shear strength parameters, used for practical design in the unsaturated conditions. Total strength parameters of claystone were c = 57 kPa, and

ϕ' = 12 degrees. This high clay content and poor shear strength parameters are however unacceptable for the MSE wall construction according to AASHTO (2002) and the Department of Highways, Thailand specifications. Even though high quality well-graded materials are preferred for use as backfill materials, they were not used for this BRE wall due to the high economical and environmental costs.

4.2.2   Design of the BRE wall

A BRE wall with 9 m height was constructed in front of a stable natural slope of 50 degrees in 15 October 2014. The distance between the slope toe and wall face was 4.75 m. The BRE wall was designed with 14 layers of reinforcement. The vertical spacing between each layer was fixed at 750 mm. The longitudinal member comprised of a deformed steel bar with a diameter of 12 mm and with a yield strength of 400 MPa. The number of transverse members were designed to satisfy the factor of safety against pullout using the predictive equation proposed by Horpibulsuk et al. (2016). The transverse members comprised of equal steel angles with a 50 mm leg length (B), 180 mm length (L) and with a yield strength of 240 MPa.

The failure pullout mechanism of the bearing reinforcement can be classified into three types, depending upon the S/B value: block failure ($S/B < 3.75$), interference failure ($3.75 \leq S/B \leq 15$, and individual failure ($S/B > 15$) (Horpibulsuk et al., 2016). In this BRE wall, the spacing between transverse members (S) was 750 mm, which is equal to 15B, hence the transverse member interference can be ignored (total pullout resistance is the product of number of transverse members and pullout resistance of a single transverse member). The length of bearing reinforcement for each layer was varied to be close to the face of the existing slope. The horizontal

spacing between the bearing reinforcements varied from 250 to 500 mm. The details of the bearing reinforcement for each layer are summarized in Table 4.1. The facing of the wall was constructed of segmental reinforced concrete panels, which measured 1.50x1.50x0.14 m in dimension.

The total pullout resistance of the bearing reinforcement, P_t, is the sum of the pullout friction and bearing resistances, P_{bn}. Maximum pullout friction resistance, P_f, of the longitudinal member can be calculated from (Horpibulsuk et al., 2016):

$$P_f = \pi D L_e \alpha \left(c + \sigma_v \tan \phi \right) \tag{4.1}$$

where D and L_e are the diameter and embedded length of the longitudinal member, respectively, σ_v is the vertical stress, α is the interface factor and equal to 0.4 based on the laboratory pullout test (Horpibulsuk et al., 2016), and c and ϕ are cohesion and friction angle of backfill, respectively.

Horpibulsuk et al. (2016) reported that the pullout bearing resistance of bearing reinforcement embedded in claystone, when S is greater than $15B$ (Figure 2), can be evaluated using the punching shear failure mechanism (Jewell et al., 1984):

$$P_{bn} = n \sigma_{b\max} BL \tag{4.2}$$

$$\sigma_{b\max} = N_q \sigma_v \tag{4.3}$$

$$N_q = \exp \left[\left(\pi/2 + \phi \right) \tan \phi \right] \tan^2 \left(45 + \frac{\phi}{2} \right) \tag{4.4}$$

$$N_c = \left(N_q - 1\right)\cot\phi \qquad\qquad\qquad\qquad (4.5)$$

where B and L are dimension of a transverse member, n is number of transverse member and N_c and N_q are bearing capacity factors.

In the design of the BRE wall, both internal (pullout and rupture failures of the reinforcement) and external (overturning, sliding, bearing and deep seated failures) stabilities were examined. Three assumptions were made to develop a conservative design for internal stability as follows: the at rest earth pressure coefficient, K_0, was used to determine the maximum pullout forces for all reinforcement layers; the potential failure plane was the bilinear failure mechanism (coherent gravity structure hypothesis) (Anderson et al., 1987); and, a static truck load (Q) of 40 kN/m on the BRE wall was considered at the end of construction. The vertical stress due to truck load ($\Delta\sigma_v$) for each reinforcement layer is thus calculated:

$$\Delta\sigma_v = \frac{2Q}{\pi z} \qquad\qquad\qquad\qquad (4.6)$$

where z is reinforcement depth.

After the examination of internal stability, the external stability was examined by numerical analysis using the PLAXIS finite element modelling software. The details of the numerical analysis method has been reported by Suksiripattanapong et al. (2012). The bearing reinforcement earth wall was modeled as a plane strain problem whereby the bearing reinforcement was modeled as geotextile elements. The finite element mesh involved 15-node triangular elements for the backfill and the foundation. Table 4.2 shows the model parameters used for the examination of

external stability. The factor of safety against external failure using c-ϕ reduction method was found to be 1.587 at the end of construction.

Table 4.1 The details of the bearing reinforcement for each layer.

Layer	Longitudinal Reinforcement				Transverse Reinforcement			
	Dia. (mm)	F_y (Mpa)	L (m)	Number	Thick (mm)	leg length, B (mm)	L (mm)	Spacing (mm)
14	12	400	9.75	9	3	50	180	750
13			8.75	8				
12			8.75	8				
11			8.75	8				
10			7.75	8				
9			7.75	8				
8			7.75	8				
7			7.75	8				
6			7.75	8				
5			7.00	8				
4			7.00	8				
3			7.00	8				
2			4.75	6				
1			4.75	6				

Table 4.2 Parameters for examination of external stability

Parameter	Symbol	Claystone	Foundation	Unit
Material model	Model	Mohr-Coulomb	Mohr-Coulomb	-
Unsaturated weight	γ_{unsat}	17	16	kN/m^3
Saturated weight	γ_{sat}	19	18	kN/m^2
Young's modulus	E_u	20,000	60,000	kN/m^2
Poisson's ratio	v_u	0.35	0.35	-
Cohesion	c	57	20	kN/m^2
Friction angle	φ	12	30	degrees
Dilatancy angle	ψ	0	0	degrees
Initial void ratio	e_{init}	0.6	0.6	-

4.2.3 Construction of the BRE wall

The instrumented BRE wall was 9 m high as illustrated in Figure 4.5. The ground was first excavated to 0.5 m depth below the original ground where the wall base was located. The wall facing panels were placed on a lean concrete leveling pad (0.50 m width and 0.15 m thickness) after 2 days of curing. The leveling pad was founded at 0.15 m depth below the excavated ground. There was no backfill material present in front of the wall facing panels, and as such the passive earth pressure acting on the wall facing was ignored. In the wall construction, seven vertically facing panels and ten horizontally facing panels (15 m width) were installed in fourteen reinforcement levels.

During the field compaction, water was sprayed on the claystone backfill to increase the water content up to a level close to the optimum water content obtained from the laboratory standard Proctor test (ASTM D698). The claystone was brittle and was broken down with compaction rollers. The broken backfill was compacted in layers approximately 0.15 m thick to a density greater than that of 90% of the relative density. The total time for construction was 20 days and the construction sequence is shown in Figure 4.6.
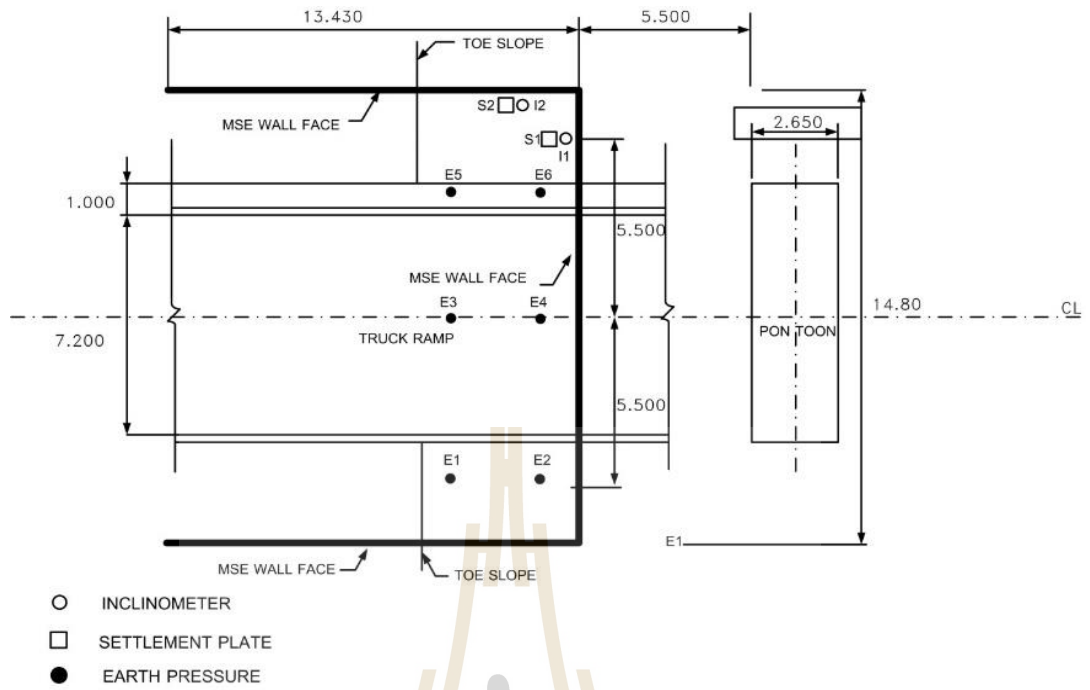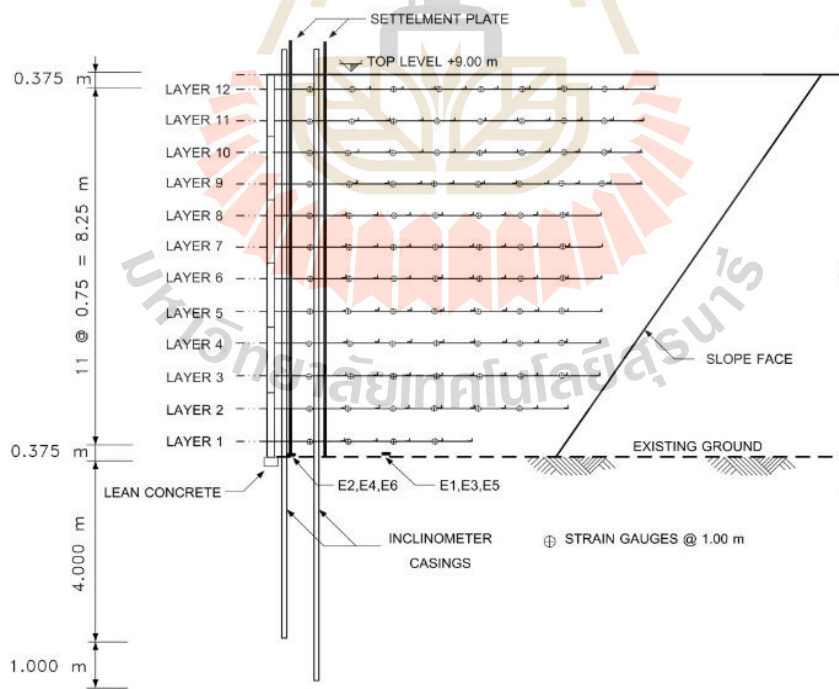
Figure 4.5 Schematic diagram of the test wall with instrumentation.
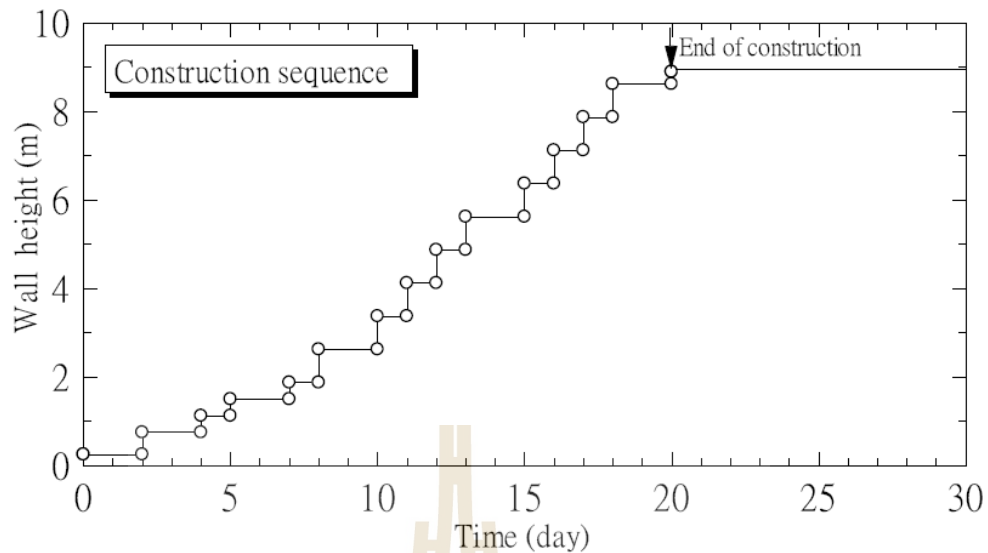
Figure 4.6 Construction sequence.

4.2.4 Instrumentation program

Due to space limitation of the BRE wall, where the truck ramp was at the middle of the BRE wall for work safety requirements, only the most significant instruments were installed, which were the settlement plates, earth pressure gauges, inclinometers and strain gauges. The instrumentation of the BRE wall is shown in Figure 4.5. Ground water table observation wells and piezometers were not used in this investigation since the ground water was very deep. The surface settlement plates, inclinometers, and earth pressure gauges were installed in the excavated ground prior to the construction of the wall. Two settlement plates were placed beneath the wall (at 0.5 m depth below the ground surface) at 0.5 and 1.5 m from the wall face (S_1 and S_2 in Figure 4.5). The settlement plates at the center of the wall could not be installed as the truck ramp was located at the center of the wall. S_1 measured the settlement at the front side close to the truck ramp while S_2 measured the settlement at the lateral side

close to the crusher plant. Settlements were measured by means of precision survey leveling with reference to a benchmark.

Lateral soil movements of the BRE wall both in front and at the lateral sides were recorded after the completion of construction and operation state for over 270 days. Lateral movements of the subsoil and the wall at various times were measured using two digital inclinometers (I_1 and I_2) located close to S_1 and S_2. The inclinometer casings were installed from the top of the wall down to the subsoil level of approximately 4 m (I_1) and 5 m (I_2) below the wall base. The subgrade upon which the wall was constructed comprised of a coal foundation, with a cohesion of 20 kPa and friction angle of 30°.

Vertical earth pressures beneath the wall in truck ramp and no truck ramp zones were measured by earth pressure gauges E_3 and E_4 and E_1, E_2, E_5 and E_6, respectively, during construction and after the completion of construction. The earth pressure gauges were installed at 0.5 m depth below the original ground level (following the foundation excavation). The strains and tensile forces along the longitudinal members were measured with outdoor waterproof type strain gauges. The rib on the deformed steel longitudinal member was initially sharpened, following which the strain gauges were attached using a special glue. The initial readings on the strain gauges were taken corresponding to zero tension (strain) in the reinforcements at the time of installation and before being subjected to any load. Subsequent readings were taken after the completion of construction at regular time intervals. The measurement points were located at 1.0 m spacing from the wall face. The strain gauges were installed on fourteen layers of the bearing reinforcement with the middle zone of the wall.

4.3 FIELD TEST RESULTS

4.3.1 Settlement

Figure 4.7 shows the relationship between settlement and time at the front and lateral sides of the BRE wall. The measured result shows that the settlement of BRE wall at the front and lateral sides is similar. The settlement of BRE wall was recorded during three intervals: during construction, during installation of the truck ramp and during operation. The settlement of the wall during construction increases with construction time due to the increased weight of the backfill as the wall was constructed. The maximum settlement at the end of construction (20 days) is about 5 mm. The installation of the truck ramp (10 days after end of construction) results in an immediate settlement of approximately 2 mm. During operation (34 days after installation of truck ramp), the settlement of the BRE wall increases immediately because of the increase in loading from the truck weight. For the safety of the surveyor, settlement was measured while no truck was on the wall. The final settlements at the front and lateral sides of the BRE wall were measured to be between 25 to 27 mm. It is of interest to mention that the settlement behavior of this BRE wall can be attributed mostly due to immediate settlement because the settlements at each stage (during construction, installation of truck ramp and operation) are insignificant with time.
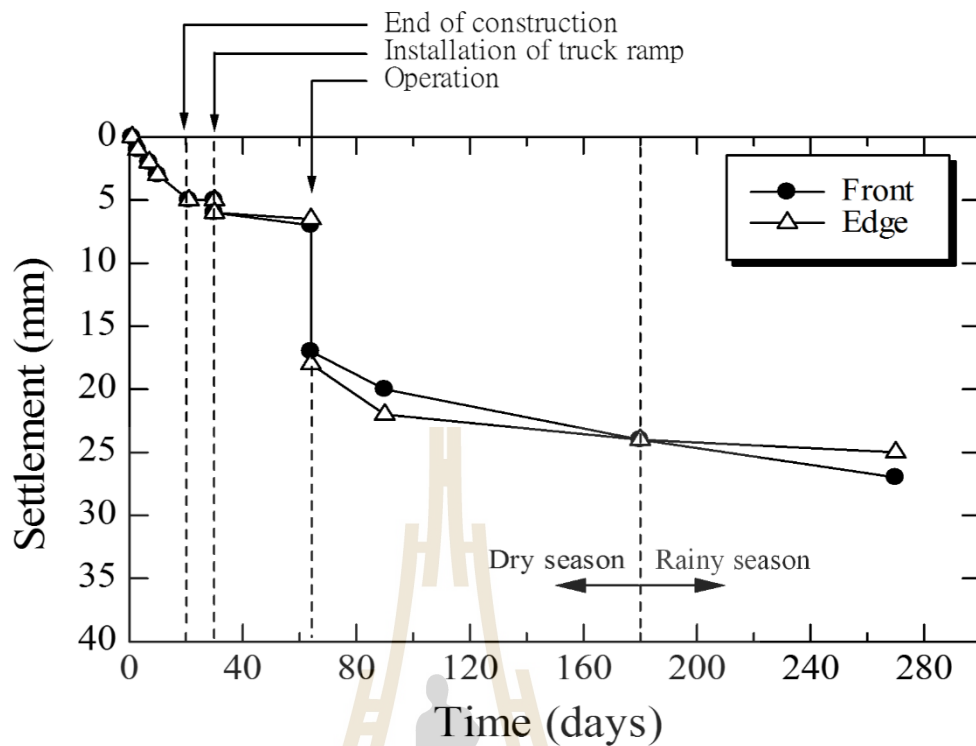
Figure 4.7 Relationship between settlement and time.

4.3.2 Bearing stress

Figure 4.8 presents the relationship between the bearing stress and construction time at the center (E_3 and E_4) and right lateral side (E_1 and E_2) of the BRE wall. The measured result indicates that during construction the bearing stress increases rapidly with construction time (20 days) due to the increase in construction load (backfill). The bearing stress then remains constant until the truck ramp was installed. In operation, the bearing stress increases slightly because the bearing stress was measured while no truck was on the truck ramp. The slight difference in bearing stress of the BRE wall at the center (E_3 and E_4) and lateral (E_1 and E_2) sides at the end of construction is noted. It is evident that the bearing stresses at lateral side (on truck ramp) at 1.0 (E_1) and 4.0 (E_2) m from wall facing are 153.4 and 158.9 kPa,

respectively. In the middle zone, the bearing stresses of the BRE wall (truck ramp zone) at 1.0 (E_3) and 4.0 (E_4) m from wall facing are 158.0 and 162.7 kPa, respectively. The bearing stresses at the lateral side of the truck ramp (E_5 and E_6) are 150.7 and 150.3 kPa, respectively. It is of interest to mention that the bearing stresses measured at E_1 to E_6 are more or less similar and are close to the calculated backfill load (unit weight x backfill height) of about 150 kPa. In other words, the backfill load distribution is uniform which is in agreement with uniform measured settlement.
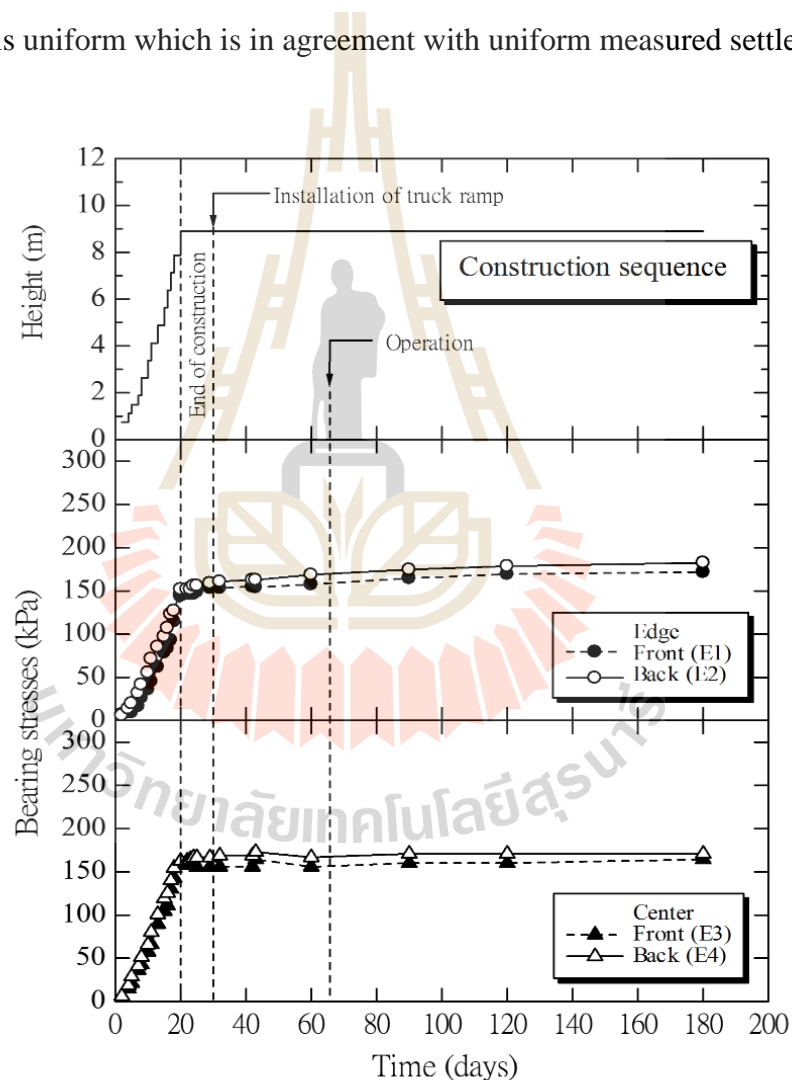
Figure 4.8 Relationship between bearing stresses and time.

4.3.3 Lateral wall movement

The measured lateral movement of the wall face at front and lateral sides after the end of construction until 270 days is shown in Figures 4.9 and 4.10. The lateral movement patterns of the wall face at front and lateral sides are similar. The lateral movement increases uniformly with wall height. Within 30 days after the end of construction (day 50), the lateral movement of the wall face at the front and lateral sides is very small with the maximum (at the top of the wall) of only less than 10 mm. As such, the ratio of lateral movement to height (δ/H) at the end of construction is approximately 0.12%, which is lower than the allowable value of 0.4% for inextensible reinforcement suggested by Brag et al. (2009). Immediately after the operation, the lateral wall movement increases with wall height up to a wall height of 2 m, which is in agreement with remarkable increase in settlement. Then the lateral movement increases clearly at wall height between 2.0 to 5.0 m. The lateral movement becomes constant for wall heights greater than 6.0 m. Although the lateral movement increases with construction time, the magnitude of lateral movement is insignificant. The maximum lateral movement occurring at the middle to top of the wall. The maximum measured lateral movements at the top of the wall (6.0-9.0 m wall height) at the front and lateral sides were small, being 58 and 20 mm, respectively at 270 days. The larger lateral movement at the front side results from the shear force from braking and acceleration of the truck on the truck ramp. With insignificant change in the settlement and lateral movement during the service stage, this BRE wall is considered to have a very high stability.
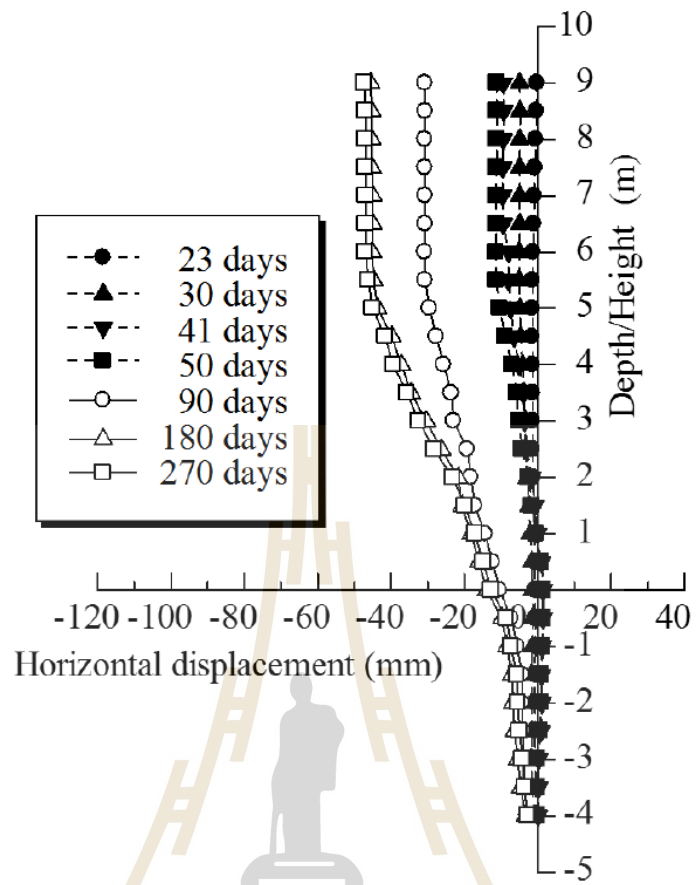
Figure 4.9 Measured lateral wall movement at front side.
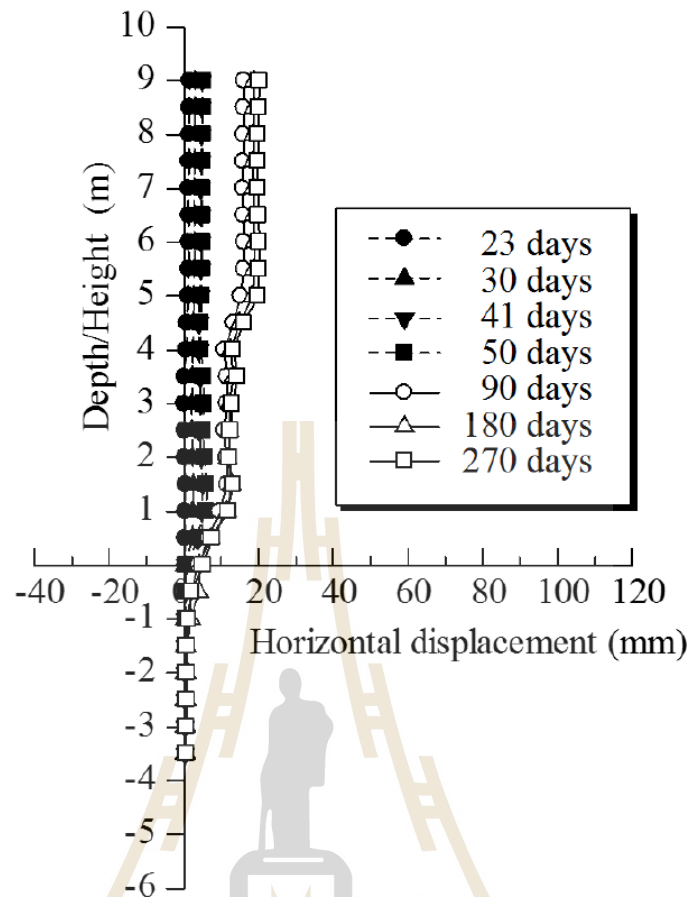
Figure 4.10 Measured lateral wall movement at lateral side.

4.3.4 Coefficient of lateral earth pressure

Figure 4.11 shows the relationship between the calculated lateral earth pressure and the wall depth (total wall height – current height) at the location of maximum measured tension in the reinforcements after the completion of construction, compared with calculated active and passive lateral earth pressures. It is found that the lateral earth pressure increases as the wall depth increases until a wall depth of 3 m (from the top of the wall) and then tends to decrease until a wall depth of 5 m. Beyond this depth, the lateral earth pressure increases again down to the wall base.

The active Rankine lateral earth pressure σ_h at the top of the wall is equal to $-2c\tan\left(45+\dfrac{\phi}{2}\right)$ = -92 kPa. The σ_h value increases with depth and becomes effectively nil at a wall depth of 8.2 m from the top. This negative lateral earth pressure due to the cohesion effect suggests that the backfill can potentially stand even without reinforcement, but possibly with a large horizontal deformation. A comparison between Rankine active earth pressure, σ_a and measured σ_h, shows that the measured σ_h is greater than σ_a and is between active and passive earth pressures. The higher measured lateral earth pressure is because the reinforcements enhance the stiffness in the backfill and results in less lateral movement.

At a depth greater than 5 m, the rate of development in lateral earth pressure with wall depth is constant. Whereas at 0 to 5 m depth, the lateral earth pressure increases from 0 to 2 m in depth and tends to decrease with depth. This behavior is similar to that of MSE walls using coarse-grained soil backfills. (Christopher et al., 1990 and Horpibulsuk et al. 2010). The difference is the magnitude of lateral earth pressure and the critical depth where the rate of development in lateral earth pressure is constant. It is noted that the lateral earth pressure can be represented in term of vertical stress as follows:

$$\sigma_h = K\sigma_v \tag{4.7}$$

where K is the coefficient of lateral earth pressure. The K values can be determined from Figure 4.11 using Eq. (4.7) and are presented in Figure 4.12. The K values are effectively constant for wall depths from 0 to 2 m and then decreases with an increase

in wall depth (from 2 to 4 m). The K values are then effectively constant at wall

depth greater than 4 m. The relationship between K and wall depth, z is as follows:

$$K = 1.3 \qquad\qquad \text{for z = 0 to 2 m} \qquad\qquad (4.8)$$

$$K = 2 - 0.35z \qquad\qquad \text{for z = 2 to 4 m} \qquad\qquad (4.9)$$

$$K = 0.6 \qquad\qquad \text{for z > 4 m} \qquad\qquad (4.10)$$
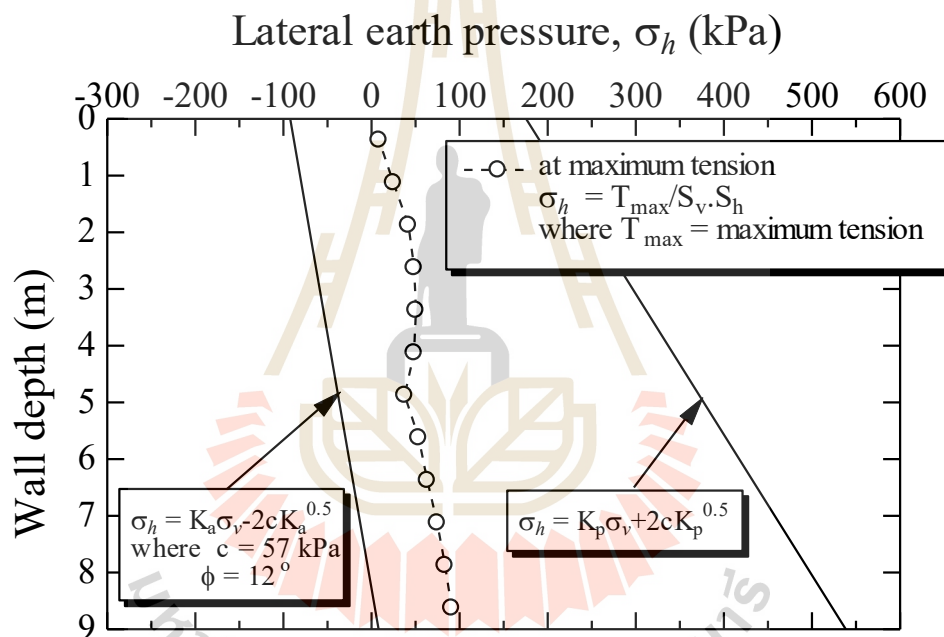
Figure 4.11 The relationship between the lateral earth pressure and the wall depth

(total wall height – current height).
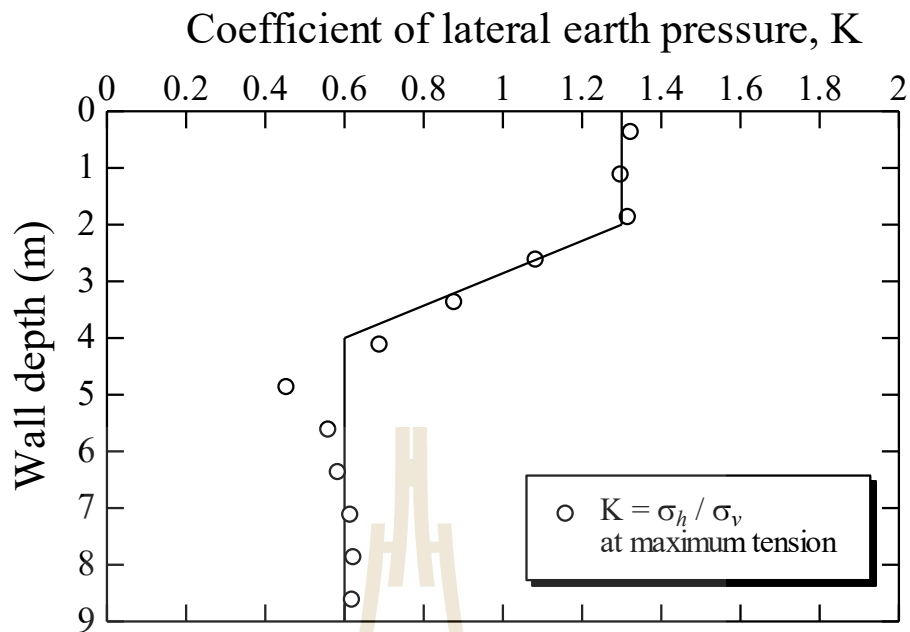
Figure 4.12 Relationship between coefficients of lateral earth pressure and wall depth.

4.3.5   Possible failure plane

Figure 4.13 illustrates the reinforcement tension measured from strain gauges after the completion of construction at different wall heights and distances from wall facing. The measured reinforcement tensions (solid line) show high tension at the point near the wall face when location of reinforcement is below H/2 while high tension is at the middle and top layers of wall occurring at the points about 3 m distance from the wall face. The dash line in Figure 4.13 shows the bilinear type of maximum tension line (coherent gravity structure hypothesis) for coarse-grained backfill, which is close to the measured maximum tension line (solid line). In other words, the coherent gravity structure hypothesis can be applied to estimate the location of the maximum tension of reinforcement embedded in fine-gained soil.
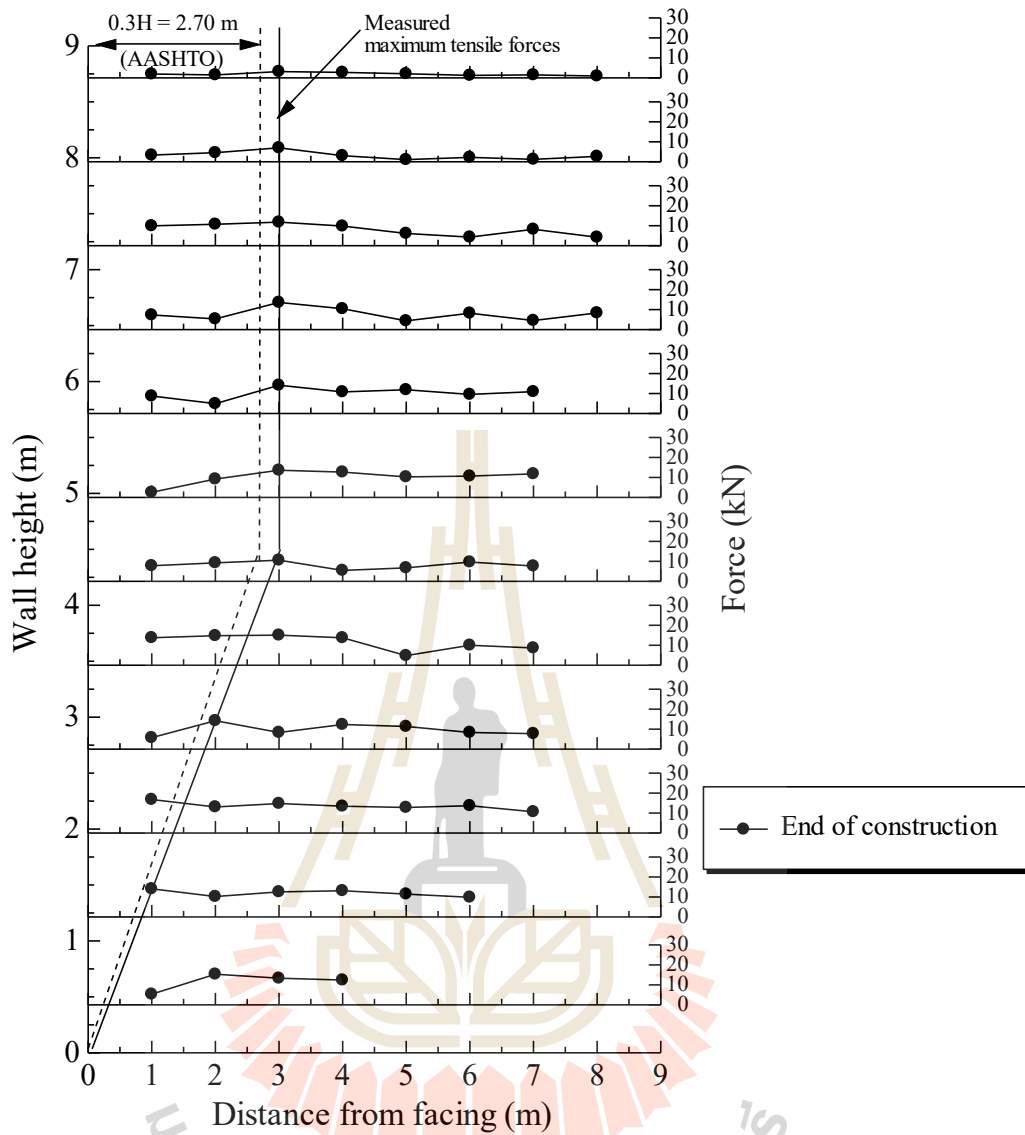
Figure 4.13 Measured tensions in the bearing reinforcements at the end of construction.

4.4 Proposed method for the BRE wall design

A proposed design method for examination of internal stability of the BRE wall using claystone backfill as truck ramp support is proposed. The examination of the internal stability deals with the rupture and pullout failure. The pullout resistance equations, maximum tension plane (possible failure plane), and coefficient of lateral

earth pressure are needed for the examination. A proposed procedure for examining the internal stability of the BRE wall is as follows:

Determine the maximum pullout force in the bearing reinforcement

1. Based on the coherent gravity structure hypothesis, approximate the maximum tension (possible failure) plane for the designed BRE wall.

2. Determine the vertical stress at each reinforcement level due to dead load and live load due to truck (using Equation (1) and assuming the truck load of 40 kN/m).

3. Determine the maximum pullout forces in the bearing reinforcements by multiplying the vertical stress by the coefficient of lateral earth pressure, K, and the vertical and horizontal spacing (S_v and S_h) of the bearing reinforcement. The relationship between K and depth presented in Figure 4.12 is recommended for this calculation.

Determine the rupture strength of the bearing reinforcement

4. Perform a tensile test on a longitudinal member to determine the yield strength.

5. Determine the rupture strength of the longitudinal member by multiplying the yield strength by the cross-sectional area.

Determine the pullout resistance of the bearing reinforcement

6. Perform a large direct shear test on the backfill material to determine the shear strength parameters.

7. Determine the interface factor, α, which can be obtained directly from a pullout test on a longitudinal member or taken as 0.4 as recommended by

Horpibulsuk et al. (2016). Hence, the friction pullout resistance can be determined from Eq. (1).

8. Determine pullout bearing resistance using Eqs. (2) to (5) and hence total pullout resistance P_t, which is the sum of the friction and bearing pullout resistances.

<u>Examine the internal stability</u>

9. Determine the factor of safety against rupture failure. This factor of safety must be greater than 2.0.

10. Determine the factor of safety against pullout failure. This factor of safety must be greater than 1.5.

The proposed method is based on sound engineering principles. However, the proposed method would benefit from calibration with several additional full-scale case histories including design and instrumented construction.

4.5 Conclusions

This paper presents the performance of the Bearing Reinforcement Earth (BRE) wall constructed as a truck ramp support for an on-site crusher plant in Mae Moh mine. During construction, the settlement and bearing stress increased rapidly with construction time due to an increase in the backfill load. The settlement and bearing stress were uniform for the case history presented. The settlement due to the backfill was only 5 mm while the cyclic load from the truck travel caused settlement of 20 mm.

The lateral movement pattern at the front and lateral sides was found to be similar with approximately the same magnitude at the end of construction but with

different magnitudes at the service stage. The maximum lateral movement at the end of construction was small, of less than 10 mm. As such, the lateral movement to height ratio is only 0.12%, which was lower than the allowable value of 0.4% and indicated the high stability of the BRE wall. The maximum lateral movement (wall height of 6.0-9.0 m) at the front was greater than that that at the lateral side (58 and 20 mm, for front and lateral sides, respectively at 270 days).

The maximum tension line for BRE wall with claystone backfill can be represented by the coherent gravity structure hypothesis. The coefficients of lateral earth pressure can be divided into three zones for 0 to 2 m, 2 to 4 m and greater than 4 m. The proposed procedure for examination of the internal stability of the BRE wall, which includes factors of safety against rupture and pullout failure, is very useful for BRE design using claystone as a backfill in other mining applications.

4.6 Reference

AASHTO (2002), **Standard Specifications for Highway and Bridge,** 7th edition. Washington D.C., American Association of State Highway and Transportation Officials.

Alfaro, M.C., Hayashi, S., Miura, N., Bergado, D.T. (1997), **"Deformation of reinforced soil-embankment system on soft clay foundation",** Soils and Foundations, Vol.37, No.4, pp.33-46.

Anderson, L.R., Sharp, K.D., and Harding, O.T. (1987), **"Performance of 50-feet high welded wire wall",** Soil Improvement – A Ten Year Update, Geotechnical Special Publication No.12, ASCE, pp.280-308.

Athanasapoulos, G.A. (1993), **"Effect of particle size on the mechanical behavior of sand-geotextile composites",** Geotextiles and Geomembranes, Vol.12, pp.252-273.

Bathurst, R.J., Allen, T.M., and Walters, D.L. (2005), **"Reinforcement load in geosynthetics wall and the case for a new working stress design method (Mercer Lecture),"** Geotextiles and Geomembranes, Vol.23, No.4, pp.287-322.

Berg, R.R., Christopher, B.R., and Samtani, N.C. (2009), **"Design of mechanically stabilized earth walls and reinforced soils slopes",** Volume II. Publication No. FHWA-NHI-10-025, Federal Highway Administration Report.

Bergado, D.T., Voottipruex, P., Modmoltin, C., and Khwanpruk, S. (1999), **"Behavior of a full-scale test wall reinforced with hexagonal wire mesh",** Ground Improvement, Vol.4, pp.47-58.

Chai, J.C. (1992), **Interaction between Grid Reinforcement and Cohesive-Frictional Soil and Performance of Reinforced Wall/Embankment on Soft Ground,** D.Eng. Dissertation, Asian Institute of Technology, Bangkok, Thailand.

Horpibulsuk, S., and Niramitkornburee, A. (2010), **"Pullout resistance of bearing reinforcement embedded in sand",** Soils and Foundations, Vol.50, No.2, pp.215-226.

Horpibulsuk, S., Kumpala, A., and Katkan, W. (2008), **"A case history on underpinning for a distressed building on hard residual soil underneath non-uniform loose sand",** Soils and Foundations, Vol.48, No.2, pp.267-286.

Horpibulsuk, S., Suksiripattanapong, C., Niramitkornburee, A., Chinkulkijniwat, A., and Tangsutthinon, T. (2011), **"Performance of earth wall stabilized with bearing reinforcements",** Geotextiles and Geomembranes, Vol.29, pp.514-524.

Horpibulsuk, S., Udomchai, A., Joongklang, A., Chinkulkijniwat, A., Mavong, N., Suddeepong, A. and Arulrajah, A. (2016), **"Pullout resistance mechanisam of bearing reinforcement embedded in residual clayey soils",** Geosynthetics International, doi: 10.1680/jgein.1600030.

Jewell, R.A., Milligan, G.W.E., Sarsby, R.W., Dubois, D. (1984), **"Interaction between soil and geogrids",** Proceedings of the sympositum on Polymer Grid Reinforcement in Civil Engineering, Thomas Telford Limited, London, UK, 11-17.

McGown, A., Andrawes, K.Z., Pradhan, S., and Khan, A.J. (1998), **"Limit state analysis of geosynthetics reinforced soil structures",** Keynote lecture, Proceedings of 6th International Conference on Geosynthetics, March, 25-29, 1998, Atlanta, GA, USA, pp.143-179.

Rowe, R.K. and Ho, S.K. (1995), **"Continuous panel reinforced soil walls on rigid foundations",** Journal of Geotechnical and Geoenvironmental Engineering, Vol.123, No.10, pp.912-920.

Skinner, G.D., and Rowe, R.K. (2005), **"Design and behavior of a geosynthetic reinforced retaining wall and bridge abutment on a yielding foundation",** Geotextitles and Geomembranes, Vol.23, No.3, pp.234-260.

Sukmak, K., Sukmak, P., Horpibulsuk, S., Han, J., Shen, S.-L., Arulrajah, A. (2015), **"Effect of fine content on the pullout resistance mechanism of bearing**

reinforcement embedded in cohesive–frictional soils", Geotextiles and Geomembranes, Vol.43, 107-117.

Sukmak, K., Sukmak, P., Horpibulsuk, S., Chinkulkijniwat, A., Arulrajah, A., Shen, S.L., (2016a), **"Pullout resistance of bearing reinforcement embedded in marginal lateritic soil at molding water contents",** Geotextiles and Geomembranes, Vol.44, 475-483.

Sukmak, K., Han, J., Sukmak, P., and Horpibulsuk, S. (2016b). **"Numerical parametric study on behavior of bearing reinforcement earth (BRE) walls with different backfill material properties",** Geosynthetics International, doi: 10.1680/jgein.1600008.

Suksiripattanapong, C., Chinkulkijniwat, A., Horpibulsuk, S., Rujikiatkamjorn, C., and Tangsuttinon, T. (2012), **"Numerical Analysis of Bearing Reinforcement Earth (BRE) Wall",** Geotextiles and Geomembranes, Vol.32, pp.28-37.

Suksiripattanapong, C., Horpibulsuk, S., Chinkulkijniwat, A., and Chai, J.C. (2013), **"Pullout resistance of bearing reinforcement embedded in coarse-grained soils",** Geotextiles and Geomembranes, Vol.36, pp.44-54.

Suksiripattanapong, C., Horpibulsuk, S., Chinkulkijniwat, C., Chai, J.C., Shen, S.L., Arulrajah, A. and Suddeepong, A. (2016), **"Numerical and sensitivity analysis of bearing reinforcement earth (BRE) wall",** KSCE Journal of Civil Engineer*ing*, doi: 10.1007/s12205-016-0576-4.

Voottipruex, P., and Bergado, D.T. (1999), **"Evaluation of full scale embankment with hexagonal wire mesh reinforcement with additional surcharge",** Geotechnical Engineering Journal, Vol.30, No.3, pp.201-220.

CHAPTER V

FAILURE OF RIVERBANK PROTECTION STRUCTURE

AND REMEDIAL APPROACH

5.1 Introduction

Retaining walls are constructed for protecting and holding back soils from buildings and any other construction structures. Early studies of retaining walls by many researchers and practitioners demonstrated that the main objective of the retaining walls is to prevent the down slope movement of soil or to resist the lateral earth pressure (Villemus et al., 2007; and Dickens & Walker, 1996). Retaining walls are classified based on the type of construction material used and are commonly constructed using masonry, stone, brick, and concrete. The gravity retaining wall is a rigid wall that provides functional support for keeping the in-situ soil in place and relies on its mass to resist pressure from behind the wall. Pile retaining walls are built by first assembling a sequence of driven or bored piles, followed by excavating away the excess soil. The pile retaining wall structures comprises driven piles or bored piles and reinforced concrete beam or steel beam bracing elements. Anchor retaining wall or tieback retaining wall, on the other hand, can be constructed in any of the aforementioned styles but also provides additional strength, with the usage of cables or other ties anchored in the rock or soil behind it.

The use of soil reinforcement for retaining wall construction, also known as the Mechanically Stabilized Earth (MSE) wall, was developed in the 1960s

(Vidal, 1969, 1978). MSE walls provide significant advantages compared to conventional reinforced concrete walls, which include the ease of installation, rapid construction, simple construction techniques, cost-effectiveness, and aesthetics (Horpibulsuk et al., 2011; Sukmak et al., 2016; Sukmak et al., 2015; Udomchai et al., 2012; Zornberg & Leshchinsky, 2003).

Many retaining walls may fail due to poor design and construction practices, as well as due to the installation of insufficient number of supports to prevent the wall from moving (Jamsawang et al., 2015). Three fundamental criteria are necessary

for the design of retaining walls, which include overturning, sliding, and bearing capacity (Harkness et al., 2000). The other important consideration for the retaining wall design is the elevation of the water table, which has significant effect on the lateral pressure imposed on the retaining wall. The water pressure due to the water table reduces the effective stress and acts as an additional force to the retaining wall, which can cause overturning and sliding failures (Huang & Luo, 2009; Won & Kim, 2007). Furthermore, this phenomenon also caused serious issues of long-term settlement and large lateral displacement of the sub-structure (Shen et al., 2014; 2017). Chai et al., (2014) and (2018) also studied the effect of pore water pressure on the sub-structure based on laboratory tests and finite element analyses methods. The laboratory model tests were conducted using a piezocone to measure the pore pressure generated during penetration and its subsequent dissipation, while finite element analyses were performed using the constitutive Modified Cam Clay model. The results clearly confirmed that the pore water pressure as well as its dissipation behavior were very important for theoretical analysis and numerical simulation. Binici et al. (2010) investigated the failure of a retaining wall in Kahramanmaras, Turkey

and reported that the main reason for the failure was the effect of hydrostatic pressure, which was not taken into consideration for the calculation of lateral pressures. The effective stress decreased as result of an increase in the hydrostatic pressure, which developed due to heavy rainfall and the resulting rise in the water level led to additional forces being imposed on the retaining wall. In addition, the widespread damage or risk of the retaining structures are threatened by natural disaster, including storming, heavy raining, and flooding that can be occurred unexpectedly and abruptly and/or by the geohazards that involve with the changing of geological and environmental conditions as well as short-term or long-term geological processes (Lyu, Shen, & Arulrajah, 2018; Lyu et al., 2018).

A case study of the investigation on the collapse of the river protection structure located at Muang Ngam, Sao Hai District, Saraburi Province along the Pasak River in Thailand is presented in this paper. The Pasak River is located in the central Thailand. It originates in Loei Province and passes through Phetchabun Province and Saraburi Province, until it joins with the Lopburi River in Lopburi Province before flowing into the Chao Phraya River in southeast of Ayutthaya Province, Thailand. To protect against devastation of the riverbank, the Department of Public Works and Town & Country Planning (DPT) and Department of Water Resources (DWR) constructed a riverbank protection structure. The construction completed in March 2012.The riverbank protection structure was 400 m long and was constructed using an anchor system. However, the details of the anchor retaining wall construction was not available at the time of the site investigation. An approximately 68 m length of riverbank protection structure constructed by the DWR collapsed in October 2012,

whereby 6 m of the wall facing moved laterally toward the river side, as shown in Figure 5.1

Figure 5.1 Large movement of wall facing of the first riverbank protection structure.
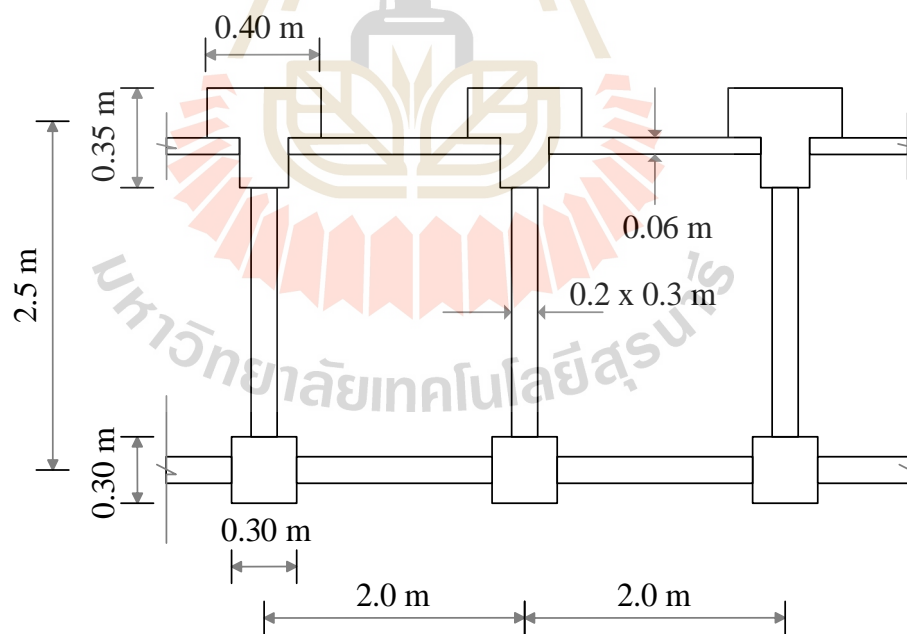
(a) plan view
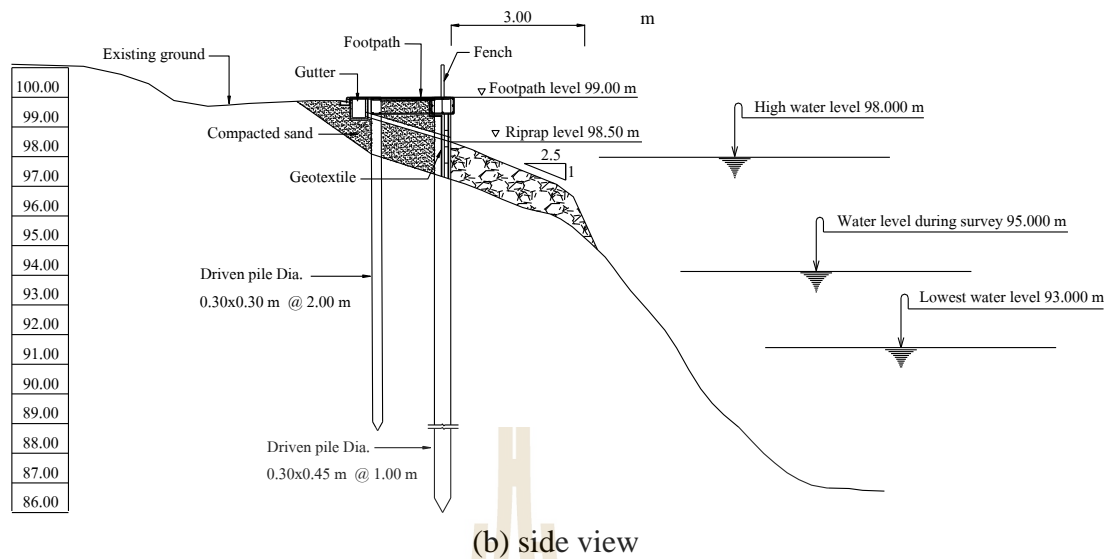
(b) side view

Figure 5.2 Details of the driven pile retaining wall structure: (a) plan view, and

(b) side view.

The DWR then designed the second riverbank protection structure by using

driven piles as a wall facing and reinforced concrete beams as bracings, as shown in

Figure 5.2 A riprap structure was constructed on the slope in front of riverbank

protection structure, in order to prevent erosion on the river bank. The construction of

this second riverbank protection structure was completed in June 2014. After about 2

months of the construction in August, lateral movement again occurred along the

retaining wall, though major settlement of the embankment was not observed.

However, large lateral movement occurred due to heavy rainfall, which resulted in

excessive settlement of the backfill and also resulted in failure of the retaining wall in

early of November 2014.

The improvement and rehabilitation of this retaining wall structure is critical

for the protection and prevention of erosion at the riverbank. The DWR engaged

geotechnical engineering experts to design the new (third) stable riverbank protection

structure and a geotechnical design and research team from Suranaree University of Technology, Thailand led by the third author was selected to once and for all solve this technical problem. The investigation methods and the remedial approaches for the failure of riverbank protection structure are presented in this research paper. This research study will also report on the positive impacts of the approach used by the research team and provides information and guidelines on the application of earth-retaining structure in riverbank rehabilitation works. The cause of failure and its remedial approaches for the riverbank protection structure presented in this paper is useful for geotechnical engineers, designers, and practitioners alike in terms of assessing suitable site exploration methods and critical analysis methods particularly in tropical regions, where the weather changes seasonally and the serious conditions (flood and drought) may occurred unexpectedly.

5.2 Causes of failure

5.2.1 Visual observation

Figure 5.3 shows the progress of lateral movement of the wall facing of the second riverbank protection structure in March 2015 and in January 2016. The photos indicated that the large damage occurred after the rainy season (July 2015 to October 2015). This can exacerbate external lateral forces, which exceeded the passive resistance of the retaining wall structure. The passive resistance occurred along the embedded length of the piles to prevent the soil movement caused by the backfill and seepage forces. Based on theory, this indicates that the soil was at the point of incipient shear failure due to the lateral force exerted by the lateral earth pressure, in which the retained soil mass was allowed to deform laterally and slide the

retaining wall outward towards the riverside. For the rigid retaining structure, it is assumed the active failure wedge in the backfill and the plan with an inclination angle of (45º + $\phi/2$) from the horizontal may result in interference in the development of the active state behind the wall (Fan & Fang, 2010; Rankine, 1857). The longitudinal crack along the wall facing was clearly detected as shown in Figure 5.4, which indicates that the retaining wall was unable to resist the sliding forces created by the horizontal soil pressure.

(a) Location 1

(b) Location 2

Figure 5.3 The retaining walls before and after its failure at: (a) Location 1 and (b) Location 2.

The longitudinal crack

Figure 5.4 The longitudinal crack along the wall facing of the riverbank protection structure.

5.2.2 Stability analysis program

For riverbank improvement and rehabilitation, first and foremost the cause and the mode of failure must be examined for the accurate design of new riverbank protection structure. The reliable non-linear finite element program PLAXIS 2D, which is widely used by geotechnical engineers and researchers to solve earth-retaining structure problems (Fan & Fang, 2010; Yu et al., 2015) was used as the design tool to analyze the stability of the retaining wall and to diagnose the cause of failure in this study. The investigated mechanical properties of the retaining wall and geotechnical properties of the backfill and foundation will be used in the finite element analysis.

Soil elements used in this study were six-node triangular isoperimetric elements, with three Gauss points for each element. Mohr-Coulomb model is an elastic-perfectly plastic model, which is often used to model soil behaviors in general and serves as a first-order model for practical design. Thus, the Mohr–Coulomb constitutive model using the effective stress analysis was used to model the stress-strain behavior of soils in this study. This model required five parameters, i.e., Young's modulus (E'), friction angle (ϕ'), Poisson's ratio (v'), cohesion (c'), and dilatancy angle (ψ'). The dilatancy angel (ψ') is approximately equal to $\phi' - 30°$ for $\phi' > 30°$ (Bolton, 1986). Interface element between the wall and the soil backfill was also considered in the analysis. Thin rectangular interface elements, six-node elements, were used between the soils and structure elements (Brinkgreve & Broere, 2015).Figure 5.5 shows the soil profile of the site. The in-situ strength of the subsoil was measured using the standard penetration test (SPT). The soil materials properties used for this finite element simulations are demonstrated in Table 5.1
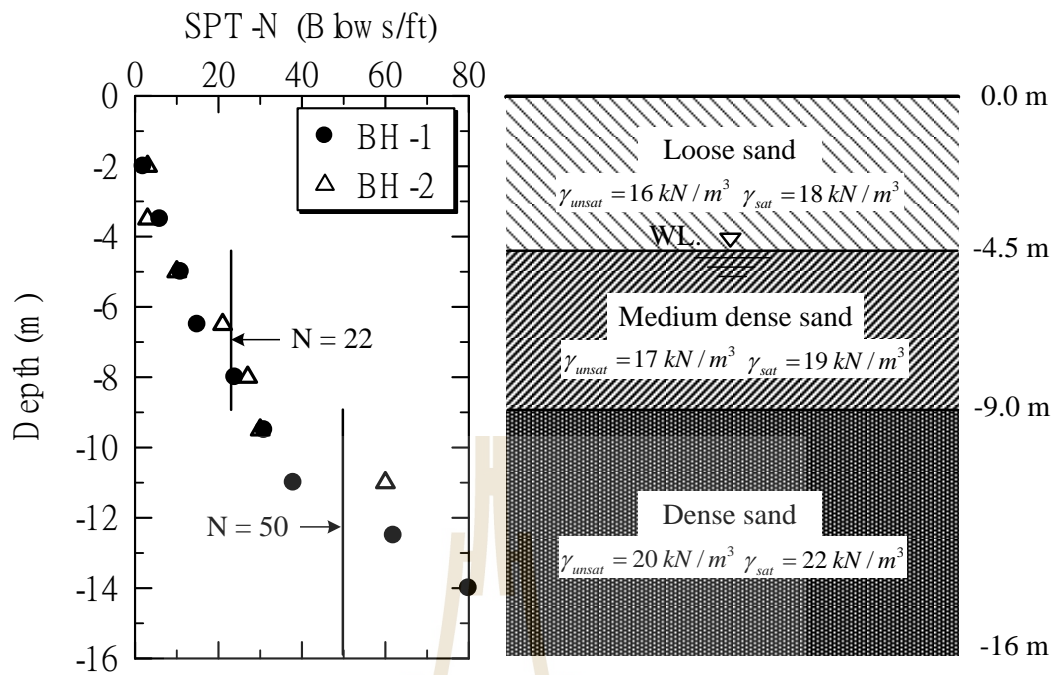
Figure 5.5 General soil profile.

Table 5.1 Soil material properties for finite element analysis.

Parameter	Symbol	Loose sand	Medium dense sand	Dense sand	Unit
Material model	Model	M-C	M-C	M-C	-
Saturate unit weight	γ_{sat}	18	19	22	kN/m³
Total unit weight	γ_{unsat}	16	17	20	kN/m³
Young's modulus	E'	30000	35000	60000	kN/m²
Friction angle	ϕ'	28	33	38	Degrees
Cohesion	c'	1	2	4	kN/m²
Dilatancy	Ψ	-	3	8	Degrees
Poisson's ratio	v'	0.3	0.3	0.3	-

5.2.3   Analysis based on available data

The entire riverbank protection structure was 400 m long and located along the Pasak River in Sao Hai District, Saraburi Province. Figure 5.2 shows the geometry and structural details of the second riverbank protection structure. The structure was braced double driven pile system with reinforced concrete bracing beams. The rear piles were rectangular in shape (0.3x0.3x10 m), while the front piles were T-section (0.35x0.40x14 m). The spacing between the back and the front piles was 2.5 m and the spacing between the T-section piles was 2 m. The rectangular reinforced concrete beams were 0.2 m in width and 0.3 m in height, while the thickness of the pre-cast wall facing between T-section piles was 0.06 m. In addition, the riprap with 0.3 m in diameter was applied in front of the riverbank protection structure to protect the erosion. Material properties of the second riverbank protection structure are presented in Table 5.2 The soil data collected from the boring log near the collapsed riverbank protection structure was obtained from the worksite and indicated that the soil layers were typical loose to dense sandy materials as shown in Figure 5.5 In addition, soil samples were also brought to the laboratory in order to carry out the triaxial test and its results were used for a soil model in the finite element analysis. For very hard soil layers, it was unable to get the samples for triaxial test. Hence, the SPT was undertaken and the ϕ values were estimated from the SPT values conversion.

Finite element (FE) modeling using PLAXIS 2D program was carried out to evaluate the stability of the riverbank protection structure. The material parameters of soil and riverbank protection structure are summarized in Table 5.1 and Table 5.2, respectively. The lowest water level of 7 m at the front of the riverbank

protection structure, measured from the surface of the backfill (at water label = 93 m in Figure 5.2), recorded by the Department of Irrigation, was used in the FE analysis. Figure 5.6 shows the factor of safety (FS) of 1.613, which is greater than the required design FS = 1.5, commonly used by the geotechnical engineers and researchers (Budhu, 2008). This demonstrates that the riverbank protection structure had a high stability, which was consistent with the visual observation of the stable part of riverbank protection structure as it is clearly evident in Figure 5.7 In other words, there might be other natural hazards causing the failure of riverbank protection structure, which were not taken into account in this analysis; hence, further site investigation to obtain primary data was required.

Table 5.2. Material properties of the driven pile retaining wall structure.

Parameter	Front Pile (0.45x0.30 m)	Back Pile (0.30x0.30m)	Reinforced Beam (d = 0.2m, h = 0.3m)
Material model	Elastic	Elastic	Elastic
Young's modulus, E' (kPa)	25.5×10^6	25.5×10^6	2.04×10^8
Area, A (m²/m)	0.135	0.09	4.99×10^{-3}
Moment of inertia, I (m⁴/m)	2.27×10^{-3}	0.338×10^{-3}	1.56×10^{-3}
Poisson's ratio, υ'	0.25	0.25	0.25
Density, γ (kN/m³)	23.5	23.5	23.5

Figure 5.6 The simulation of FE analysis with the lowest water level at the front of

the retaining wall.

Figure 5.7 The visual observation of the stable retaining wall structure.

5.2.4   Analysis based on primary data

The primary data was collected by interviewing residents living close to the riverbank, and whom were affected by the collapse of the earlier riverbank protection structure. It was found that there were farm lands behind the failed riverbank protection structure, inducing water seepage through the backfill, particularly during the rainy season.
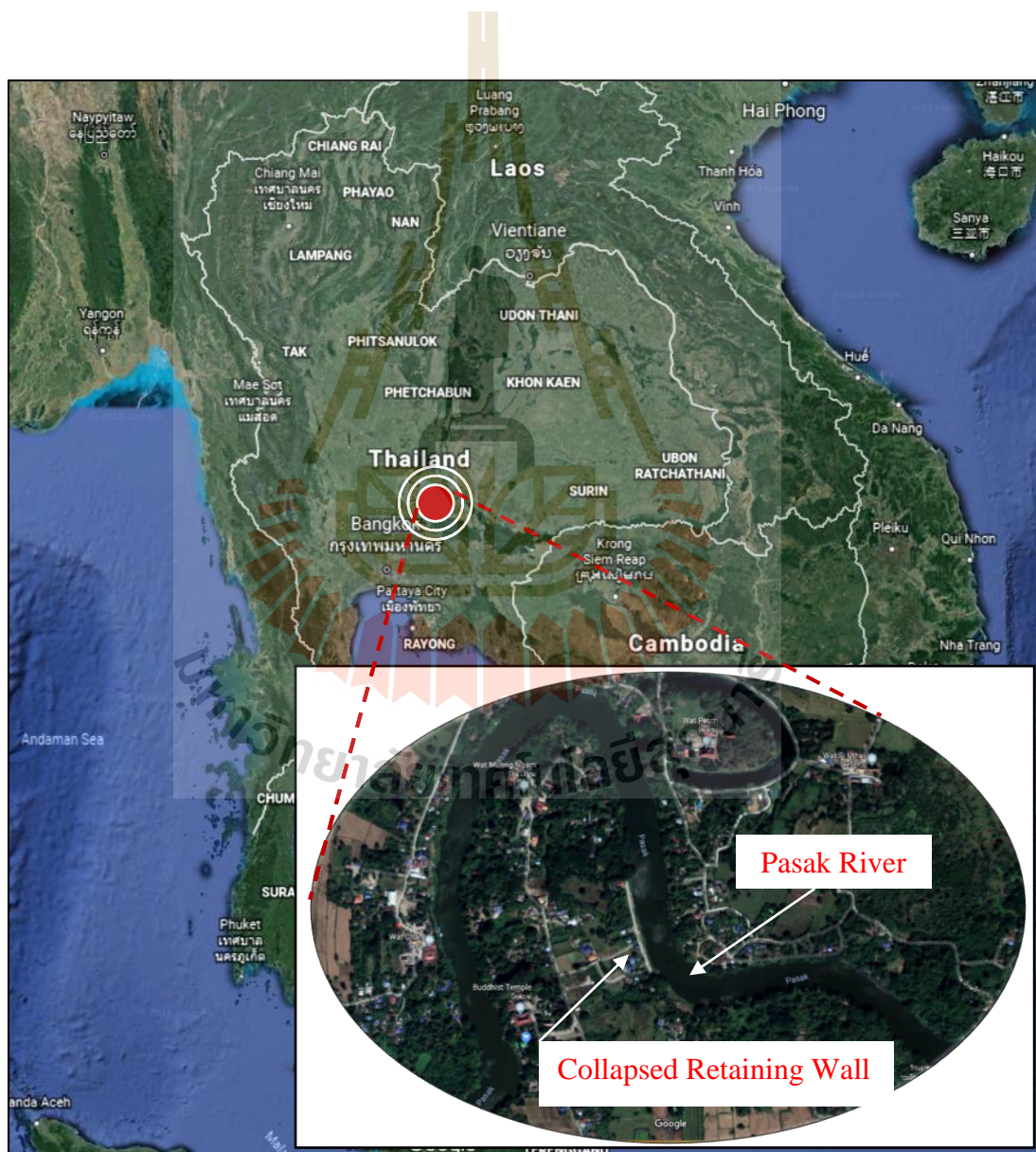
Figure 5.8 The location of the collapsed retaining wall.
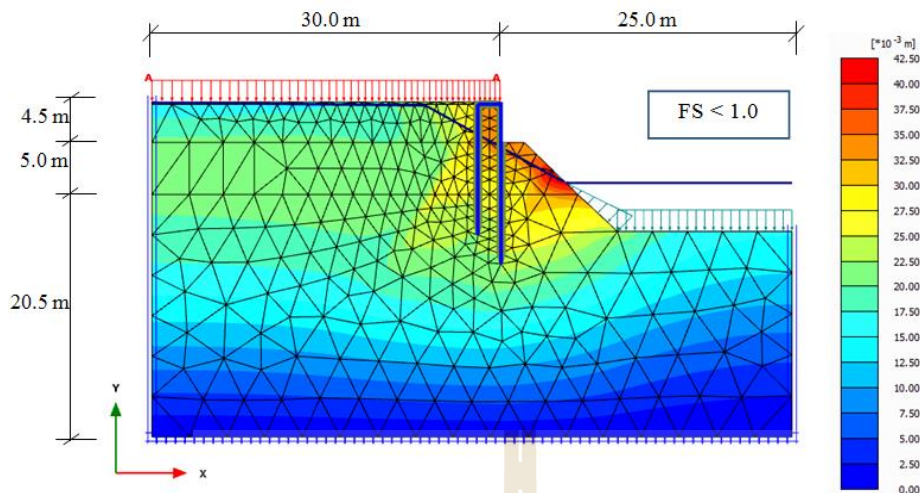
Figure 5.9 FE analysis of riverbank protection structure with water seepage and eroded slope.

Furthermore, the aerial photograph map as shown in Figure 5.8 indicated that the riverbank protection structure was located on the curvature of the watershed, which faced to the strong force direction of river flow. It was thus assumed that the current continuously scoured the riverbank, undermining the natural slope (loss of soil mass) in front of the riverbank protection structure. The erosion changed the geometry of the slope in the passive zone, reducing the stability of the collapsed riverbank protection structure. Elevation surveying along the exiting slope in front of the collapsed riverbank protection structure was carried out, which revealed that the existing slope was much steeper than that obtained from the drawing previous designed by the DWR (available data). This supports the assumption of soil erosion due to the attack of strong current at the curvature of watershed.

Based on the primary data, the FE analyses were carried out using the water level measured by piezometers and the measured existing slope in the passive zone. The water level behind riverbank protection structure was 0.5 m below the

backfill surface while the water level in the river was 7 m below the backfill surface (Figures 5.9). The results showed soil collapse at the end of computation, indicating that FS was lower than 1.0 and the erosion and seepage force significantly induced the instability of the riverbank protection structure. Similar failure of the retaining walls caused by the insufficient base friction and passive resistance in front of the wall was also found (Abdullahi, 2009; Budhu, 2008; Rankine, 1857).
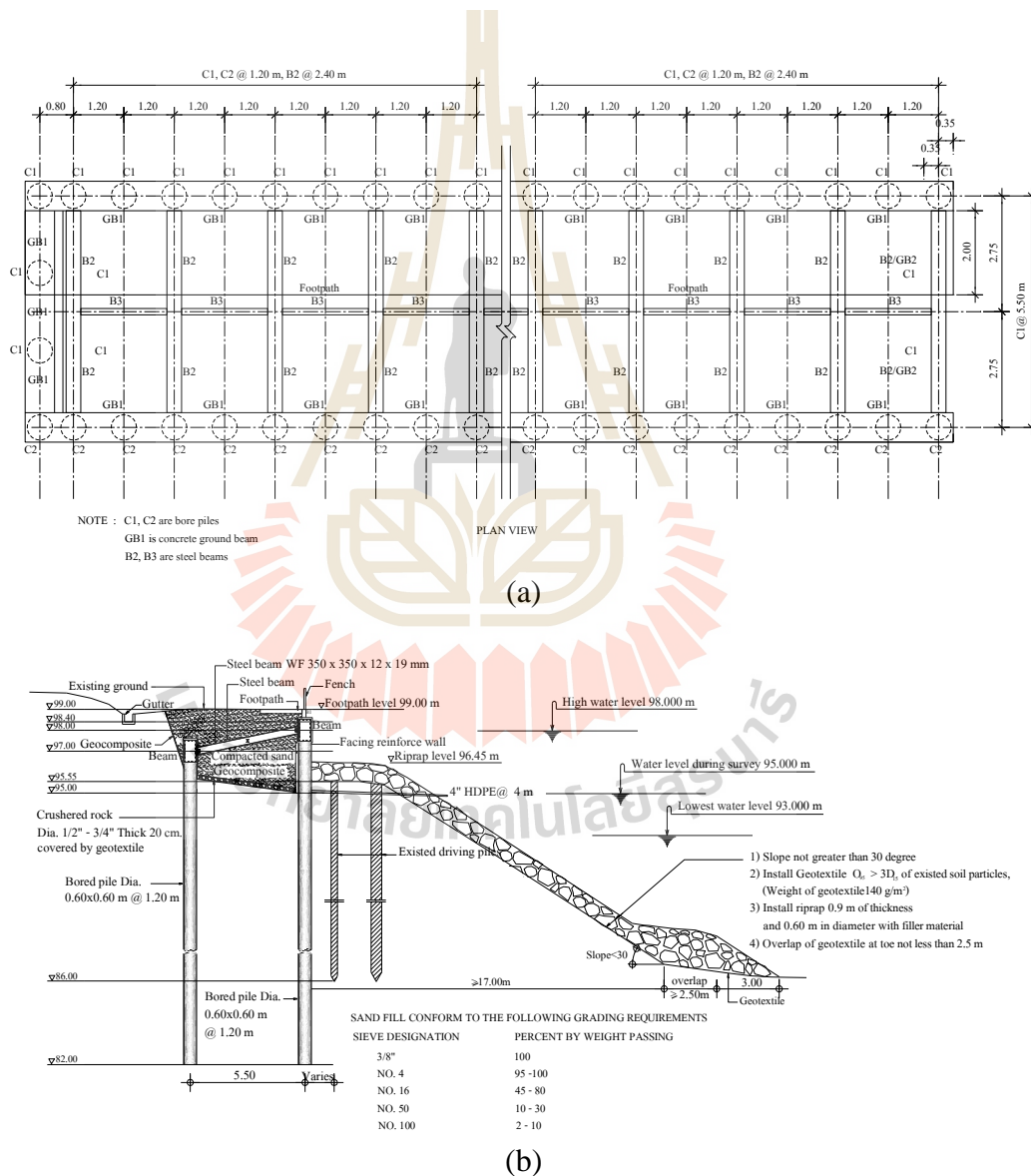
Figure 5.10 Structural detailing of retaining wall: (a) plan view and (b) side view.

5.3　Remedial approach

5.3.1　Design concept

The mitigation and rehabilitation of the collapsed riverbank protection structure were designed to minimize the effect of water seepage and steep slope. The new riverbank protection structure was designed based on the three main approaches as follows:

For the first approach, the river bank protection structure must have an adequate factor of safety against excessive translation, rotation, bearing capacity failure, deep-seated failure, and seepage-induced instability. Hence, the pile-bracing system was proposed. Due to the very dense sandy soil foundation, the bored piles with diameter of 60 cm were selected to have long embedded length (to have high passive lateral resistance) and installed behind the existed driven piles as shown in Figure 5.10 The long piles also increased the stability against deep-seated failure. The new designed length of piles was approximately 18 m, while the spacing between the front and back of bored piles (longitudinal direction) and (cross section direction) was 5.5 m and 1.2 m, respectively. The reinforced concrete pile caps were constructed on the front and the back bored pile heads, while the steel H-beam were used as bracing between the caps.

The geocomposite as a drainage medium to minimize the water level behind the riverbank protection structure was applied for the second approach. Previous researchers have extensively studied on the geocomposite drainage under seepage condition in earth-retaining structure and reported that the geocomposite drainage reduced the water pressure in the reinforced zone, thus increasing the stability of retaining walls (Chinkulkijniwat et al., 2017; Udomchai et al., 2012).

For the third approach, the existing slope was adjusted to be not steeper than 30 degrees. The riprap was designed and installed on the crest and the toe of the adjusted slope in front of the riverbank protection structure in order to protect the erosion problem. The geotextile layer, as a filter medium was installed beneath the riprap layer to separate the natural slope soil and the riprap. The design procedure for the riprap was carried out according to the previous technical paper (Galay et al., 1987; Maynord et al., 1989), which is based on the local average channel velocity and local depth of the river. The riprap design procedure according to the DPT's regulation (DPT, 2006) can be expressed as follows:

Required design diameter of riprap

$$d = \frac{CV^2}{g(s-1)\Omega}$$ (5.1)

where:

V = velocity of the river flow,

C = coefficient of the river flow,

   $C = 0.3$ for low turbulent flow, and

   $C = 0.7$ for high turbulent flow

g = gravity acceleration, ($g = 9.81$)

s = specific gravity of riprap, and

Ω = side slope correction factor

Velocity of the river flow (*V*) can be calculated as:

$$V = \frac{\text{Discharge}}{\text{Area}} = \frac{1500 m^3 / s}{350 m^2} = 4.3 \ m/s \qquad (5.2)$$

Side slope correction factor (Ω) can be calculated by:

$$\Omega = \left[1 - \frac{\sin^2 \alpha}{\sin^2 \phi} \right]^{1/2} = 0.628 \qquad (5.3)$$

where:

Friction angle of soil slope $\phi \geq 40°$

Angle of slope at the front of retaining wall $\alpha \leq 30°$

Hence, the required design diameter of riprap was

$$d = \frac{0.3 \times 4.3^2}{9.81 \times (2.65 - 1) \times 0.628} = 0.55 \ m$$

The required 60 cm diameter of riprap was installed with thickness of 90 cm and 180 cm at the crest and the toe of the slope at the front of the riverbank protection structure, respectively. Figure 5.11 shows the structural detailing and the schematic drawing of the riverbank protection structure.
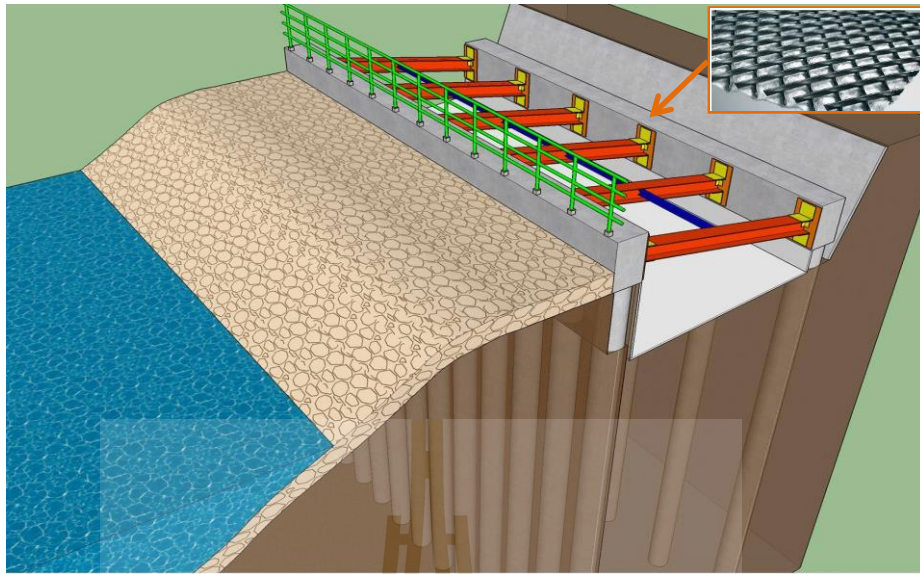
Figure 5.11 Schematic drawing of the retaining wall system.

5.3.2   Finite element verification

The stability of the new riverbank protection structure was verified by FE analysis method using the PLAXIS 2D program. The model parameters used for the backfill soil and for the new riverbank protection structure are summarized in Table 5.1 and Table 5.3, respectively.

Table 5.3. Material properties of the bored pile retaining wall structure.

Parameter	Bored Pile (ϕ = 0.6m)	Strut
Material model	Elastic	Elastic
Young's modulus, E' (kN/m^2)	25.5×10^6	2.04×10^8
Area, A (m^2/m)	0.235	4.99×10^{-3}
Moment of inertia, I (m^4/m)	5.30×10^{-3}	85×10^{-6}
Poisson's ratio, υ'	0.25	0.3
Density, γ (kN/m^3)	23.5	78.5

The effect of water flow in the riverbank protection structure was considered in the simulation by FE analysis. Two cases of water flow condition were considered for FE analysis: the lowest water level in the river at -7 m obtained from the groundwater station (see Figure 5.2, water label = 93 m) and rapid drawdown (water level at the bed of the river, water label = 87 m). Due to the variation of water levels in the river seasonally, the reservoir nearby the riverbank protection structure can be subjected to rapid drawdown phenomenon (Budhu, 2008). In this case the lateral water force is removed and the excess pore water pressure does not have enough time to dissipate. According to AASHTO (2002), FS must be greater than 1.5 and 1.3 for the lowest water level in the river and the rapid drawdown conditions, respectively.
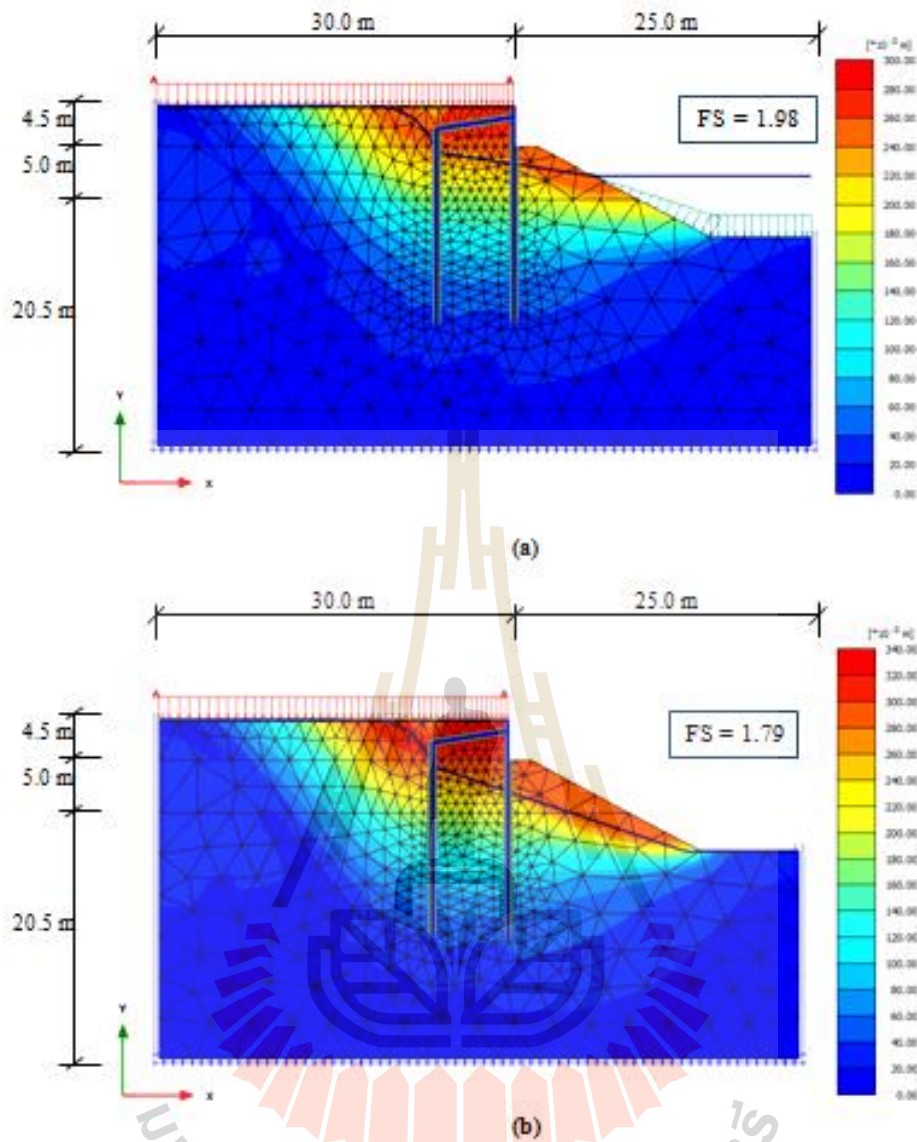
Figure 5.12 FE analysis of new riverbank protection structure: (a) lowest water level, and (b) rapid drawdown.

Figure 5.12a-b presents the simulation results of FE analyses for both case studies. The FE analysis results based on the c-ϕ reduction method (Brinkgreve & Broere, 2015) showed that the FS = 1.98 and 1.79 for case 1(with the lowest water level) and case 2 (rapid drawdown phenomenon), respectively. FS values for both case studies were greater than the required factor of safety, which demonstrated that

the designed riverbank protection structure was stable. The stable new riverbank protection has been constructed in May 2017 and completed in October 2017. Since then, the riverbank protection structure has been serviced without any track of failure.

The cause of failure and its remedial approaches for the riverbank protection structure presented in this paper is helpful for geotechnical engineers, designers, and practitioners alike in terms of assessing suitable site exploration methods and critical analysis methods particularly in tropical regions, where the weather changes seasonally and the serious conditions (flood and drought) may occurred unexpectedly.

5.4 Conclusion

This paper presents a case study of the collapsed riverbank protection structure and the remedial approach used. The riverbank protection structure has been constructed to protect the riverbank along the Pasak river in Suraburi province, Thailand. However, a part of the riverbank protection structure collapsed during the rainy season. The first and second collapsed riverbank protection structures were anchor retaining wall structure and pile driven retaining wall structure, respectively.

Based on the site investigation and the FE analysis on the collapsed retaining wall, the failure of the riverbank protection structure was caused by the water flow entering into the permeable backfill soil layers and directing to the river. The other reason is that the strong streams continuously scour the riverbank and undermine the natural slope in front of the riverbank protection structure. Erosion changes the geometry of the slope in passive zone, which reduces the resistance of passive earth pressure and ultimately resulting in slope failure.

Therefore, three fundamental approaches have been proposed for the new riverbank protection structure. The bored pile-bracing system was constructed as a new riverbank protection structure. The long and stiff bored piles improve the external stability of the riverbank protection structure. The geocomposite was installed behind riverbank protection structure as a drainage to minimize the water level during rainy season. The riprap was applied on the crest and the toe of the slope in front of the riverbank protection structure to protect the erosion.

The finite element analysis results confirmed that the new riverbank protection structure was stable for both lowest water level in the river and rapid drawn down conditions. This case study of the collapsed riverbank protection structure and its remedial approaches in this paper can be considered as the geotechnical documentary and a guideline or information, which is helpful for the application of earth-retaining structure rehabilitation. The new riverbank protection was constructed in a period of 5 months (May 2017 till October 2017) and since then there has been no evidence of any further failures.

5.5 References

AASHTO. (2002). **Standard specifications for highway bridges.** 7th ed. American association of state highway and transportation officials, Inc., Washington (DC).

Abdullahi, M. a. M. (2009). **Evaluation of Causes of Retaining Wall Failure.** Leonardo Electronic Journal of Practices and Technologies (14), 11-18.

Binici, H., Temiz, H., Kayadelen, C., Kaplan, H., & Durgun, M. Y. (2010). **Retaining Wall Failure due to Poor Construction and Design Aspects A Case Study.** Electronic Journal of Construction Technologies/Yapi Teknolojileri Elektronik Dergisi, *6*(1).

Bolton, M. (1986). **The strength and dilatancy of sands.** Géotechnique, 36(1), 65-78.

Brinkgreve, R., & Broere, W. (2015). **PLAXIS 2D Reference Manual 2015.** Delft, Netherlands 2010.

Budhu, M. (2008). **SOIL MECHANICS AND FOUNDATIONS, (With CD):** John Wiley & Sons.

Chai, J.-C., Julfikar Hossain, M., Carter, J., & Shen, S.-L. (2014). **Cone penetration-induced pore pressure distribution and dissipation.** Computers and Geotechnics, 57, 105-113. doi:https://doi.org/10.1016/j.compgeo.2014.01.008

Chai, J.-C., Shen, J. S.-L., Liu, M. D., & Yuan, D.-J. (2018). **Predicting the performance of embankments on PVD-improved subsoils.** Computers and Geotechnics, *93*, 222-231. doi:https://doi.org/10.1016/j.compgeo.2017.05.018

Chinkulkijniwat, A., Horpibulsuk, S., Van, D. B., Udomchai, A., Goodary, R., & Arulrajah, A. (2017). **Influential factors affecting drainage design considerations for mechanical stabilised earth walls using geocomposites.** Geosynthetics International, 24(3), 224-241. doi:10.1680/jgein.16.00027

Dickens, J., & Walker, P. (1996). **Use of distinct element model to simulate behaviour of dry-stone walls.** Structural engineering review, 8(2-3), 187-199.

DPT. (2006). **Dam protection design,** Department of Public Works and Town & Country Planning, Thailand.

Fan, C.-C., & Fang, Y.-S. (2010). **Numerical solution of active earth pressures on rigid retaining walls built near rock faces.** Computers and Geotechnics, 37(7), 1023-1029. doi:http://dx.doi.org/10.1016/j.compgeo.2010.08.004

Galay, V., Yaremko, E., & Quazi, M. (1987). **River bed scour and construction of stone riprap protection.** Sediment Transfer in Gravel-Bed Rivers. John Wiley & Sons New York. 1987. p 353-379, 1 tab, 19 fig, 41 ref.

Harkness, R. M., Powrie, W., Zhang, X., Brady, K. C., & O'Reilly, M. P. (2000). **Numerical modelling of full-scale tests on drystone masonry retaining walls.** Géotechnique, 50(2), 165-179. doi:10.1680/geot.2000.50.2.165

Horpibulsuk, S., Suksiripattanapong, C., Niramitkornburee, A., Chinkulkijniwat, A., & Tangsutthinon, T. (2011). **Performance of an earth wall stabilized with bearing reinforcements.** Geotextiles and Geomembranes, 29(5), 514-524. doi:https://doi.org/10.1016/j.geotexmem.2011.05.002

Huang, C.-C., & Luo, W.-M. (2009). **Behavior of soil retaining walls on deformable foundations.** Engineering Geology, 105(1), 1-10. doi:https://doi.org/10.1016/j.enggeo.2009.01.003

Lyu, H.-M., Shen, J., & Arulrajah, A. (2018). **Assessment of Geohazards and Preventative Countermeasures Using AHP Incorporated with GIS in Lanzhou,** China. Sustainability, 10(2), 304.

Lyu, H.-M., Sun, W.-J., Shen, S.-L., & Arulrajah, A. (2018). **Flood risk assessment in metro systems of mega-cities using a GIS-based modeling approach.** Science of The Total Environment, 626, 1012-1025. doi:https://doi.org/10.1016/j.scitotenv.2018.01.138

Maynord, S. T., Ruff, J. F., & Abt, S. R. (1989). **Riprap Design.** Journal of Hydraulic

    Engineering, 115(7), 937-949.doi:doi:10.1061/(ASCE)0733-

    9429(1989)115:7(937)

Rankine, W. M. (1857). **On the stability of loose earth.** Philosophical transactions of

    the Royal Society of London, 147, 9-27.

Shen, S.-L., Wu, H.-N., Cui, Y.-J., & Yin, Z.-Y. (2014). **Long-term settlement**

    behaviour of metro tunnels in the soft deposits of Shanghai. Tunnelling

    and Underground Space Technology, 40, 309-323.

    doi:https://doi.org/10.1016/j.tust.2013.10.013

Shen, S. L., Wang, Z. F., & Cheng, W. C. (2017). **Estimation of lateral**

    displacement induced by jet grouting in clayey soils. Géotechnique, 67(7),

    621-630. doi:10.1680/jgeot.16.P.159

Sukmak, K., Sukmak, P., Horpibulsuk, S., Chinkulkijniwat, A., Arulrajah, A., &

    Shen, S.-L. (2016). **Pullout resistance of bearing reinforcement embedded**

    in marginal lateritic soil at molding water contents. Geotextiles and

    Geomembranes, 44(3), 475-483.

    doi:https://doi.org/10.1016/j.geotexmem.2015.07.016

Sukmak, K., Sukmak, P., Horpibulsuk, S., Han, J., Shen, S.-L., & Arulrajah, A.

    (2015). **Effect of fine content on the pullout resistance mechanism of**

    bearing reinforcement embedded in cohesive–frictional soils. Geotextiles

    and Geomembranes, 43(2), 107-117.

    doi:https://doi.org/10.1016/j.geotexmem.2014.11.010

Udomchai, A., Chinkulkijniwat, A., & Horpibulsuk, S. (2012). **Physical model tests**

    on Mechanically stabilized earth walls with geocomposite drainage under

seepage condition. Geosynthetics Asia (2012) Proceeeding of the 5th Asian Regio-nal Conference on Geosynthetics, Bangkok, Thailand, pp.613-616.

Vidal, H. (1969). **The principle of reinforced earth.** Highway research record(282).

Vidal, H. (1978). **Stabilized earth structures**: Google Patents.

Villemus, B., Morel, J., & Boutin, C. (2007). **Experimental assessment of dry stone retaining wall stability on a rigid foundation.** Engineering structures, 29(9), 2124-2132.

Won, M.-S., & Kim, Y.-S. (2007). **Internal deformation behavior of geosynthetic-reinforced soil walls.** Geotextiles and Geomembranes, 25(1), 10-22. doi:https://doi.org/10.1016/j.geotexmem.2006.10.001

Yu, Y., Damians, I. P., & Bathurst, R. J. (2015). **Influence of choice of FLAC and PLAXIS interface models on reinforced soil–structure interactions.** Computers and Geotechnics, 65, 164-174. doi:http://dx.doi.org/10.1016/j.compgeo.2014.12.009

Zornberg, J., & Leshchinsky, D. (2003). **Comparison of international design criteria for geosynthetic-reinforced soil structures.** Landmarks in Earth Reinforcement, 2, 1095-1106.

CHAPTER VI

CONCLUSIONS AND RECOMMENDATIONS

6.1 Summary and conclusions

This thesis presents the case studies of the performance of innovative geosynthetic applications as retaining structures for both man-made and natural slope protection. For man-made slope protection, the mechanical stabilized earth (MSE) wall utilizing the bearing reinforcement as earth reinforcement, designated as Bearing Reinforcement Earth (BRE) wall was designed to support the weight of the truck ramp and also to provide a 90-degree slope to allow shorter access for the large mine haul trucks. The laboratory-scale pullout resistance mechanism and predictive equations in terms of vertical stress, dimension, spacing and number of traverse members for cohesive-frictional soils were carried out. A full-scale instrumented BRE wall with claystone backfill in the Mae Moh mine was constructed as a truck ramp support for an on-site crusher plant. The performance of the BRE wall after the completion of construction and during the service period included settlement, bearing stress, lateral movement, lateral earth pressure and tension force in the reinforcements. Therefore, a proposed method of designing the BRE wall is very useful for BRE design using claystone as a backfill in general mining application is then developed.

For the natural slope protection, the case study of a collapsed riverbank protection structure, located in the curvature of the watershed along the Pasak river in

Saraburi Province, Thailand is presented. The Pasak river is located in the central Thailand. It originates in Loei Province and passes through Phetachbun Province and Saraburi Province, until it joints with the Lopburi river in Lopburi Province before flowing into the Chao Phraya river in southeast of Ayutthaya Province, Thailand. To protect against devastation of the riverbank, a 40m-m riverbank protection structure was constructed. This retaining structure; however, was collapsed approximately four months after the complete of the construction. Although efforts have been made to twice rehabilitate this collapsed structure, the rebuilt protection structures were unstable to prevent progressive collapse damage and the cause of their failure remained elusive. The investigation methods and the remedial approaches for the failure of riverbank protection structure are presented in this thesis. It will also report on the positive impacts of the approach used and provide information and guideline on the application of earth-retaining structure in riverbank rehabilitation works. Finally, the conclusions can be drawn as follows:

6.1.1 For Man-Made Slope Protection

The total pullout resistance of the bearing is the sum of friction pullout and bearing pullout resistances. The lower water content resulted in the higher shear strength; hence the higher pullout friction resistance. The peak and residual interaction factors (α_p and α_r) value were dependent upon F, irrespective of water contents. The relationships between α_p and α_r versus F were suggested in this paper. The relationships between α_p and α_r versus F are $\alpha_p = -0.002F + 0.859$ and $\alpha_r = -0.0014F + 0.592$, respectively.

The bearing pullout resistance of transverse members P_{bn} is calculated in terms of the number of transverse members (n), transverse members interference factor (IF) and pullout bearing resistance of a single transverse member P_{b1}. The IF and P_{b1} were found to be primarily controlled by F and w/w_{OWC}. The 3-dimensional plot of β versus w/w_{OWC} and F in the range of $0.67 \le w/w_{owc} \le 1.33$ and $20 < F < 98\%$ were proposed to determine P_{b1}. On the dry side of optimum and at w_{OWC}, the β of $\pi/2$ is recommended for $F < 45\%$. On the wet side of optimum, β reduces significantly with increasing w/w_{OWC} and F until $\beta = \pi/3$ at $w/w_{OWC} = 1.33$.

The 3-dimensional plot of S_2/B versus w/w_{OWC} and F in the range of $0.67 \le w/w_{owc} \le 1.33$ and $20 < F < 98\%$ were proposed to determine IF. The S_2/B value was essentially the same of 13.3 for $w \le w_{OWC}$, whereas the S_2/B value for $w > w_{OWC}$ decreased linearly with increasing water content. Using the relationship between β versus F and w and the relationship between IF versus F and w, the P_{bn} can be calculated.

The lateral movement pattern at the front and lateral sides was found to be similar with approximately the same magnitude at the end of construction but with different magnitudes at the service stage. The maximum lateral movement at the end of construction was small, of less than 10 mm. As such, the lateral movement to height ratio was only 0.12%, which was lower than the allowable value of 0.4% and indicated the high stability of the BRE wall. The maximum lateral movement (wall height of 6.0-9.0 m) at the front was greater than that at the lateral side (58 and 20 mm, for front and lateral sides, respectively at 270 days).

The maximum tension line for BRE wall with claystone backfill can be represented by the coherent gravity structure hypothesis. The coefficients of lateral earth pressure can be divided into three zones for 0 to 2 m, 2 to 4 m and greater than 4 m. The proposed procedure for examination of the internal stability of the BRE wall, which includes factors of safety against rupture and pullout failure, is very useful for BRE design using claystone as a backfill in other mining applications.

The method of predicting pullout resistance of bearing reinforcement embedded in cohesive-frictional soils were proposed in this research. The proposed method is useful for examination of internal stability of BRE wall during construction and at the end of construction. The development of this generalized pullout resistance predictive equations for the bearing reinforcement is based on sound principle. The framework can be extended to develop pullout resistance predictive equations of other reinforcement systems for further study.

6.1.2 For Natural Slope Protection

Based on the site investigation and the FE analysis on the collapsed retaining wall, the failure of the riverbank protection structure was caused by the water flow entering into the permeable backfill soil layers and directing to the river. The other reason is that the strong streams continuously scour the riverbank and undermine the natural slope in front of the riverbank protection structure. Erosion changes the geometry of the slope in passive zone, which reduces the resistance of passive earth pressure and ultimately resulting in slope failure.

Therefore, three fundamental approaches have been proposed for the new riverbank protection structure. The bored pile-bracing system was constructed as a new riverbank protection structure. The long and stiff bored piles improved the

external stability of the riverbank protection structure. The geocomposite was installed behind riverbank protection structure as a drainage to minimize the water level during rainy season. The riprap was applied on the crest and the toe of the slope in front of the riverbank protection structure to protect the erosion. The finite element analysis results confirmed that the new riverbank protection structure was stable for both lowest water level in the river and rapid drawn down conditions.

6.2 Recommendations for future work

The outcomes of this thesis evidently indicate that the retaining structure analysis and design as well as remedial approach based on scientific and appropriate geotechnical methods are significantly important for either natural or man-made slope protections. An appropriate stepwise procedure for assessing pullout bearing resistance and a proposed design method for examination of internal stability of the MSE wall are very important for the new kind of retaining structure. While the cause of failure and its remedial approaches for the natural slope protection structures presented in this thesis are useful for geotechnical engineers, designers, and practitioners alike in terms of assessing suitable site exploration methods and critical analysis methods particular in tropical regions, where the weather changes seasonally and the serious conditions (flood and drought) may occur unexpectedly. Following is the recommendation for further studies:

- The equations for estimating the pullout resistance of bearing reinforcement are proposed and verified for cohesive-frictional soils. The effect of particle size on the mode of failure and the transverse member

interference of the bearing reinforcement embedded in various soils should be further studied.

- The finite element analysis of the retaining wall in this study was performed in 2-D plain strain condition. However, the vertical spacing and shape of pile (3-D) affect the performance of the retaining wall. Consequently, the 3-D finite element analysis of the retaining wall should be performed and compare with the 2-D one.
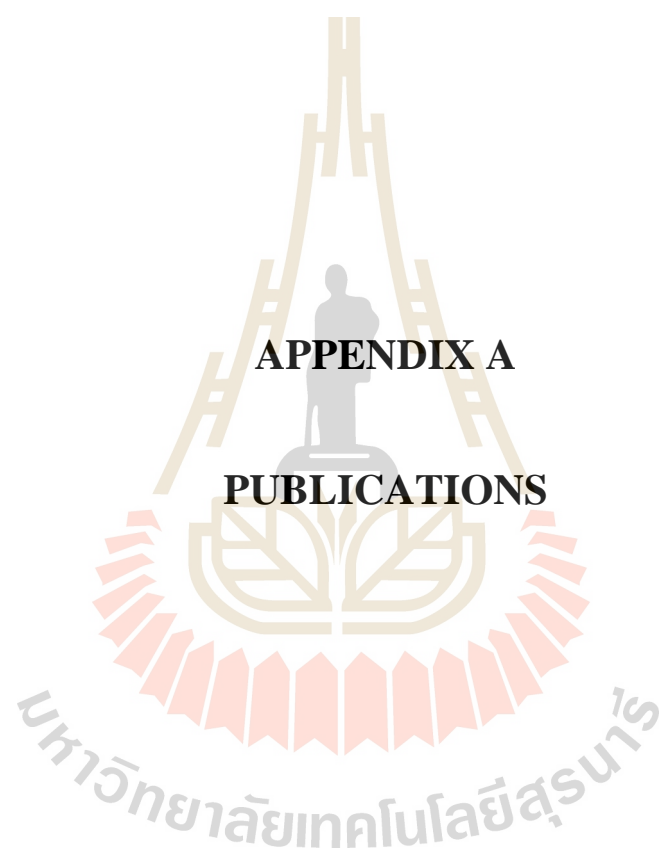
APPENDIX A

PUBLICATIONS

List of Publications

INTERNATIONAL JOURNAL PAPERS

Udomchai, A., Hoy, M., Horpibulsuk, S., Chinkulkijniwat, A., & Arulrajah, A. (2018). **Failure of riverbank protection structure and remedial approach: A case study in Suraburi province, Thailand.** Engineering Failure Analysis, 91, 243-254.

Buritatun, A., Takaikaew, T., Horpibulsuk, S., Udomchai, A., Hoy, M., Vichitcholchai, N., & Arulrajah, A. (2020). **Mechanical Strength Improvement of Cement-Stabilized Soil Using Natural Rubber Latex for Pavement Base Applications.** Journal of Materials in Civil Engineering, 32(12), 04020372.

Sukmak, G., Sukmak, P., Joongklang, A., Udomchai, A., Horpibulsuk, S., Arulrajah, A., & Yeanyong, C. (2020). **Predicting pullout resistance of bearing reinforcement embedded in cohesive-frictional soils.** Journal of Materials in Civil Engineering, 32(3), 04019379.

Buritatum, A., Horpibulsuk, S., Udomchai, A., Suddeepong, A., Takaikaew, T., Vichitcholchai, N., and Arulrajah, A. (2021). **Durability improvement of cement stabilized pavement base using natural rubber latex.** Transportation Geotechnics, 100518.

Ngo, D. H., Horpibulsuk, S., Buritatun, A., Udomchai, A., Samingthong, W., Arulrajah, A., & Kulariyasup, W. (2021). **Hydraulic transmissivity of geocomposite confined with soils.** Measurement, 109106.

Failure of riverbank protection structure and remedial approach: A case study in Suraburi province, Thailand

Artit Udomchai[a], Menglim Hoy[b], Suksun Horpibulsuk[c,*], Avirut Chinkulkijniwat[d], Arul Arulrajah[e]

[a] School of Civil Engineering, Suranaree University of Technology, Nakhon Ratchasima 30000, Thailand
[b] Center of Excellence in Innovation for Sustainable Infrastructure Development, Suranaree University of Technology, Nakhon Ratchasima 30000, Thailand
[c] School of Civil Engineering and Center of Excellence in Innovation for Sustainable Infrastructure Development, Suranaree University of Technology, Thailand
[d] School of Civil Engineering and Center of Excellence in Civil Engineering, Suranaree University of Technology, Thailand
[e] Department of Civil and Construction Engineering, Swinburne University of Technology, Victoria 3122, Australia

ARTICLE INFO

ABSTRACT

This paper presents the case study of a collapsed riverbank protection structure, located in the curvature of the watershed along the Pasak river in Saraburi province, Thailand. Although efforts have been made to twice rehabilitate this collapsed structure, the rebuilt protection structures were unstable to prevent progressive collapse damage and the causes of their failure remained elusive. The project team was engaged to carried out the site investigation and finite element analysis prior to providing the remedial approach on the collapsed structure. The outcome from this study reveals that the natural disaster events were the main causes of the structure failure. During the rainy season, water flowed into the river from upstream farmlands by crossing the backfill of the riverbank protection structure. Seepage forces were thus developed in the direction of inflows, which resulted in reduced stability of the riverbank protection structure. Furthermore, the strong currents in the river continuously scoured the banks, undermining the natural slope in front of the riverbank protection structure, resulting in soil erosion in the passive zone and instability of the protection structure. Based on these two causes of failure, a remedial solution was devised using a new bored pile riverbank protection structure with the usage of geocomposites and ripraps. Geocomposites and ripraps were installed at the back and front of the bored pile walls to relieve the structure from seepage forces and to prevent soil erosion, respectively. An adequate factor of safety against the external and internal failure of the new riverbank protection structure was verified by finite element modeling and the results confirmed that the structure was safe.

1. Introduction

Retaining walls are constructed for protecting and holding back soils from buildings and any other construction structures. Early studies of retaining walls by many researchers and practitioners demonstrated that the main objective of the retaining walls is to

prevent the down slope movement of soil or to resist the lateral earth pressure [10,28]. Retaining walls are classified based on the type of construction material used and are commonly constructed using masonry, stone, brick, and concrete. The gravity retaining wall is a rigid wall that provides functional support for keeping the in-situ soil in place and relies on its mass to resist pressure from behind the wall. Pile retaining walls are built by first assembling a sequence of driven or bored piles, followed by excavating away the excess soil. The pile retaining wall structures comprises driven piles or bored piles and reinforced concrete beam or steel beam bracing elements. Anchor retaining wall or tieback retaining wall, on the other hand, can be constructed in any of the aforementioned styles but also provides additional strength, with the usage of cables or other ties anchored in the rock or soil behind it.

The use of soil reinforcement for retaining wall construction, also known as the Mechanically Stabilized Earth (MSE) wall, was developed in the 1960s [26,27]. MSE walls provide significant advantages compared to conventional reinforced concrete walls, which include the ease of installation, rapid construction, simple construction techniques, cost-effectiveness, and aesthetics [15,23–25,31].

Many retaining walls may fail due to poor design and construction practices, as well as due to the installation of insufficient number of supports to prevent the wall from moving (Jamsawang et al. [32]). Three fundamental criteria are necessary for the design of retaining walls, which include overturning, sliding, and bearing capacity [14]. The other important consideration for the retaining wall design is the elevation of the water table, which has significant effect on the lateral pressure imposed on the retaining wall. The water pressure due to the water table reduces the effective stress and acts as an additional force to the retaining wall, which can cause overturning and sliding failures [16,29]. Furthermore, this phenomenon also caused serious issues of long-term settlement and large lateral displacement of the sub-structure [21,22]. Chai et al. [7,8] also studied the effect of pore water pressure on the sub-structure based on laboratory tests and finite element analyses methods. The laboratory model tests were conducted using a piezocone to measure the pore pressure generated during penetration and its subsequent dissipation, while finite element analyses were performed using the constitutive Modified Cam Clay model. The results clearly confirmed that the pore water pressure as well as its dissipation behavior were very important for theoretical analysis and numerical simulation. Binici et al. [3] investigated the failure of a retaining wall in Kahramanmaras, Turkey and reported that the main reason for the failure was the effect of hydrostatic pressure, which was not taken into consideration for the calculation of lateral pressures. The effective stress decreased as result of an increase in the hydrostatic pressure, which developed due to heavy rainfall and the resulting rise in the water level led to additional forces being imposed on the retaining wall. In addition, the widespread damage or risk of the retaining structures are threatened by natural disaster, including storming, heavy raining, and flooding that can be occurred unexpectedly and abruptly and/or by the geohazards that involve with the changing of geological and environmental conditions as well as short-term or long-term geological processes [17,18].

A case study of the investigation on the collapse of the river protection structure located at Muang Ngam, Sao Hai District, Saraburi Province along the Paksak River in Thailand is presented in this paper. The Paksak River is located in the central Thailand. It originates in Loei Province and passes through Phetchabun Province and Saraburi Province, until it joins with the Lopburi River in Lopburi Province before flowing into the Chao Phraya River in southeast of Ayutthaya Province, Thailand. To protect against devastation of the riverbank, the Department of Public Works and Town & Country Planning (DPT) and Department of Water Resources (DWR) constructed a riverbank protection structure. The construction completed in March 2012. The riverbank protection structure was 400 m long and was constructed using an anchor system. However, the details of the anchor retaining wall construction was not available at the time of the site investigation. An approximately 68 m length of riverbank protection structure constructed by the DWR collapsed in October 2012, whereby 6 m of the wall facing moved laterally toward the river side, as shown in Fig. 1.

The DWR then designed the second riverbank protection structure by using driven piles as a wall facing and reinforced concrete beams as bracings, as shown in Fig. 2. A riprap structure was constructed on the slope in front of riverbank protection structure, in order to prevent erosion on the river bank. The construction of this second riverbank protection structure was completed in June 2014. After about 2 months of the construction in August, lateral movement again occurred along the retaining wall, though major

Fig. 1. Large movement of wall facing of the first riverbank protection structure.
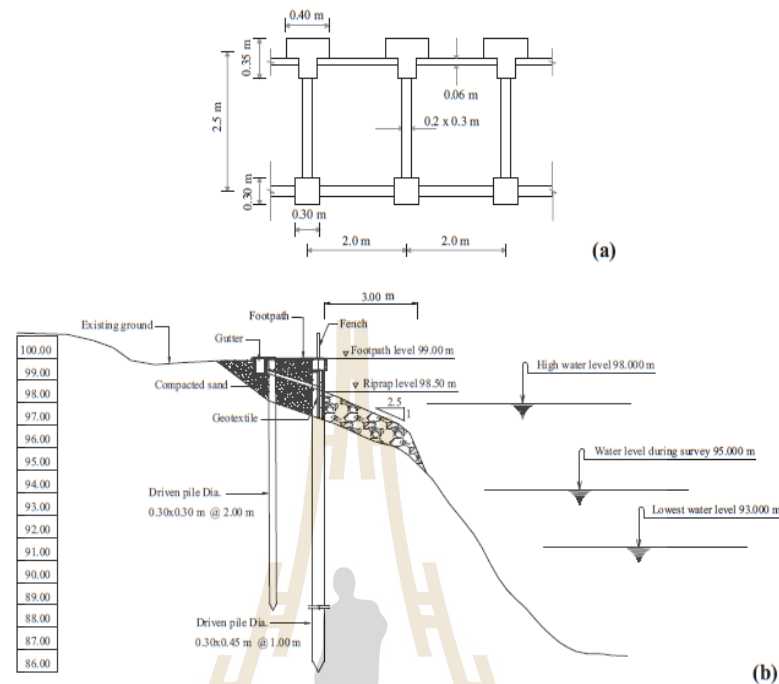
Fig. 2. Details of the driven pile retaining wall structure: (a) Plan view, and (b) side view.

settlement of the embankment was not observed. However, large lateral movement occurred due to heavy rainfall, which resulted in excessive settlement of the backfill and also resulted in failure of the retaining wall in early of November 2014.

The improvement and rehabilitation of this retaining wall structure is critical for the protection and prevention of erosion at the riverbank. The DWR engaged geotechnical engineering experts to design the new (third) stable riverbank protection structure and a geotechnical design and research team from Suranaree University of Technology, Thailand led by the third author was selected to once and for all solve this technical problem. The investigation methods and the remedial approaches for the failure of riverbank protection structure are presented in this research paper. This research study will also report on the positive impacts of the approach used by the research team and provides information and guidelines on the application of earth-retaining structure in riverbank rehabilitation works. The cause of failure and its remedial approaches for the riverbank protection structure presented in this paper is useful for geotechnical engineers, designers, and practitioners alike in terms of assessing suitable site exploration methods and critical analysis methods particularly in tropical regions, where the weather changes seasonally and the serious conditions (flood and drought) may occurred unexpectedly.

2. Causes of failure

2.1. Visual observation

Fig. 3 shows the progress of lateral movement of the wall facing of the second riverbank protection structure in March 2015 and in January 2016. The photos indicated that the large damage occurred after the rainy season (July 2015 to October 2015). This can exacerbate external lateral forces, which exceeded the passive resistance of the retaining wall structure. The passive resistance occured along the embedded length of the piles to prevent the soil movement caused by the backfill and seepage forces. Based on theory, this indicates that the soil was at the point of incipient shear failure due to the lateral force exerted by the lateral earth pressure, in which the retained soil mass was allowed to deform laterally and slide the retaining wall outward toward the riverside. For the rigid retaining structure, it is assumed the active failure wedge in the backfill and the plan with an inclination angle of $(45° + \phi/2)$ from the horizontal may result in interference in the development of the active state behind the wall [12,20]. The longitudinal crack along the wall facing was clearly detected as shown in Fig. 4, which indicates that the retaining wall was unable to resist the sliding forces created by the horizontal soil pressure.

2.2. Stability analysis program

For riverbank improvement and rehabilitation, first and foremost the cause and the mode of failure must be examined for the

(a) Location 1

(b) Location 2

Fig. 3. The retaining walls before and after its failure at: (a) Location 1 and (b) Location 2.

The longitudinal crack

Fig. 4. The longitudinal crack along the wall facing of the riverbank protection structure.

accurate design of new riverbank protection structure. The reliable non-linear finite element program PLAXIS 2D, which is widely used by geotechnical engineers and researchers to solve earth-retaining structure problems [12,30] was used as the design tool to analyze the stability of the retaining wall and to diagnose the cause of failure in this study. The investigated mechanical properties of the retaining wall and geotechnical properties of the backfill and foundation will be used in the finite element analysis.

Soil elements used in this study were six-node triangular isoperimetric elements, with three Gauss points for each element. Mohr-Coulomb model is an elastic-perfectly plastic model, which is often used to model soil behaviors in general and serves as a first-order model for practical design. Thus, the Mohr–Coulomb constitutive model using the effective stress analysis was used to model the stress–strain behavior of soils in this study. This model required five parameters, i.e., Young's modulus (E'), friction angle (ϕ'), Poisson's ratio (v'), cohesion (c'), and dilatancy angle (ψ'). The dilatancy angel (ψ') is approximately equal to $\phi'-30°$ for $\phi' > 30°$ [4]. Interface element between the wall and the soil backfill was also considered in the analysis. Thin rectangular interface elements, six-node elements, were used between the soils and structure elements [5]. Fig. 5 shows the soil profile of the site. The in-situ strength of the subsoil was measured using the standard penetration test (SPT). The soil materials properties used for ths finite element simulations are demonstrated in Table 1.
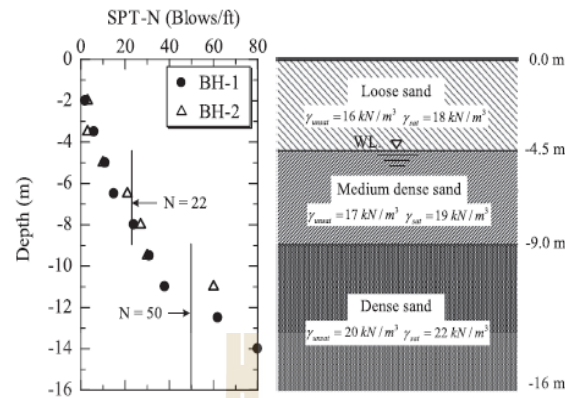
Fig. 5. General soil profile.

Table 1
Soil material properties for finite element analysis.

Parameter	Symbol	Loose sand	Medium dense sand	Dense sand	Unit
Material model	Model	M-C	M-C	M-C	–
Saturate unit weight	γ_{sat} m	18	19	22	kN/m³
Total unit weight	γ_{unsat}	16	17	20	kN/m³
Young's modulus	E' m	30,000	35,000	60,000	kN/m²
Friction angle	ϕ' m	28	33	38	Degree
Cohesion	c' m	1	2	4	kN/m²
Dilatancy	Ψ m	–	3	8	Degree
Poisson's ratio	v' m	0.3	0.3	0.3	–

2.3. Analysis based on available data

The entire riverbank protection structure was 400 m long and located along the Paksak River in Sao Hai District, Saraburi Province. Fig. 2 shows the geometry and structural details of the second riverbank protection structure. The structure was braced double driven pile system with reinforced concrete bracing beams. The rear piles were rectangular in shape (0.3 × 0.3 × 10 m), while the front piles were T-section (0.35 × 0.40 × 14 m). The spacing between the back and the front piles was 2.5 m and the spacing between the T-section piles was 2 m. The rectangular reinforced concrete beams were 0.2 m in width and 0.3 m in height, while the thickness of the pre-cast wall facing between T-section piles was 0.06 m. In addition, the riprap with 0.3 m in diameter was applied in front of the riverbank protection structure to protect the erosion. Material properties of the second riverbank protection structure are presented in Table 2. The soil data collected from the boring log near the collapsed riverbank protection structure was obtained from the worksite and indicated that the soil layers were typical loose to dense sandy materials as shown in Fig. 5. In addition, soil samples were also brought to the laboratory in order to carry out the triaxial test and its results were used for a soil model in the finite element analysis. For very hard soil layers, it was unable to get the samples for triaxial test. Hence, the SPT was undertaken and the ϕ values were estimated from the SPT values conversion.

Finite element (FE) modeling using PLAXIS 2D program was carried out to evaluate the stability of the riverbank protection structure. The material parameters of soil and riverbank protection structure are summarized in Tables 1 and 2, respectively. The lowest water level of 7 m at the front of the riverbank protection structure, measured from the surface of the backfill (at water label = 93 m in Fig. 2), recorded by the Department of Irrigation, was used in the FE analysis. Fig. 6 shows the factor of safety (FS) of

Table 2
Material properties of the driven pile retaining wall structure.

Parameter	Front pile	Back pile	Reinforced beam
	(0.45 × 0.30 m)	(0.30 × 0.30 m)	(d = 0.2 m, h = 0.3 m)
Material model	Elastic	Elastic	Elastic
Young's modulus, E' (kN/m²)	25.5×10^6	25.5×10^6	2.04×10^8
Area, A (m²/m)	0.135	0.09	4.99×10^{-3}
Moment of inertia, I (m⁴/m)	2.27×10^{-3}	0.338×10^{-3}	1.56×10^{-3}
Poisson's ratio, v'	0.25	0.25	0.25
Density, γ (kN/m³)	23.5	23.5	23.5

169

A. Udomchai et al.

Engineering Failure Analysis 91 (2018) 243–254
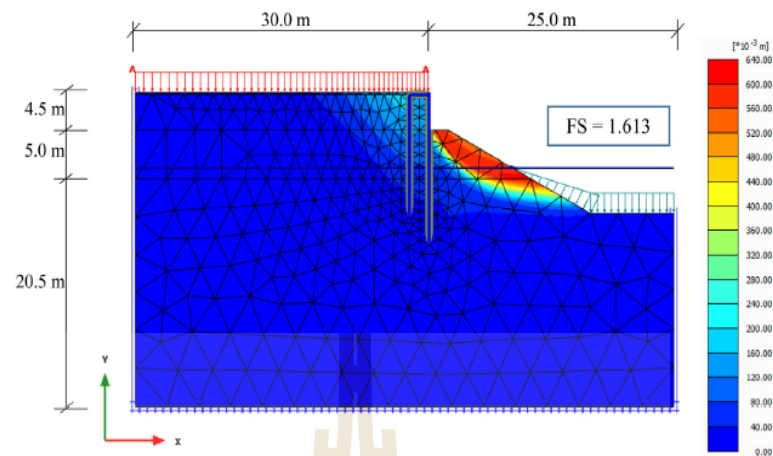
Fig. 6. The simulation of FE analysis with the lowest water level at the front of the retaining wall.

1.613, which is greater than the required design FS = 1.5, commonly used by the geotechnical engineers and researchers [6]. This demonstrates that the riverbank protection structure had a high stability, which was consistent with the visual observation of the stable part of riverbank protection structure as it is clearly evident in Fig. 7. In other words, there might be other natural hazards causing the failure of riverbank protection structure, which were not taken into account in this analysis; hence, further site investigation to obtain primary data was required.

2.4. Analysis based on primary data

The primary data was collected by interviewing residents living close to the riverbank, and whom were affected by the collapse of the earlier riverbank protection structure. It was found that there were farm lands behind the failed riverbank protection structure, inducing water seepage through the backfill, particularly during the rainy season.

Furthermore, the aerial photograph map as shown in Fig. 8 indicated that the riverbank protection structure was located on the curvature of the watershed, which faced to the strong force direction of river flow. It was thus assumed that the current continuously scoured the riverbank, undermining the natural slope (loss of soil mass) in front of the riverbank protection structure. The erosion changed the geometry of the slope in the passive zone, reducing the stability of the collapsed riverbank protection structure. Elevation surveying along the exiting slope in front of the collapsed riverbank protection structure was carried out, which revealed that the existing slope was much steeper than that obtained from the drawing previous designed by the DWR (available data). This supports the assumption of soil erosion due to the attack of strong current at the curvature of watershed.

Based on the primary data, the FE analyses were carried out using the water level measured by piezometers and the measured existing slope in the passive zone. The water level behind riverbank protection structure was 0.5 m below the backfill surface while the water level in the river was 7 m below the backfill surface (Fig. 9). The results showed soil collapse at the end of computation, indicating that FS was lower than 1.0 and the erosion and seepage force significantly induced the instability of the riverbank protection structure. Similar failure of the retaining walls caused by the insufficient base friction and passive resistance in front of the

Fig. 7. The visual observation of the stable retaining wall structure.

248
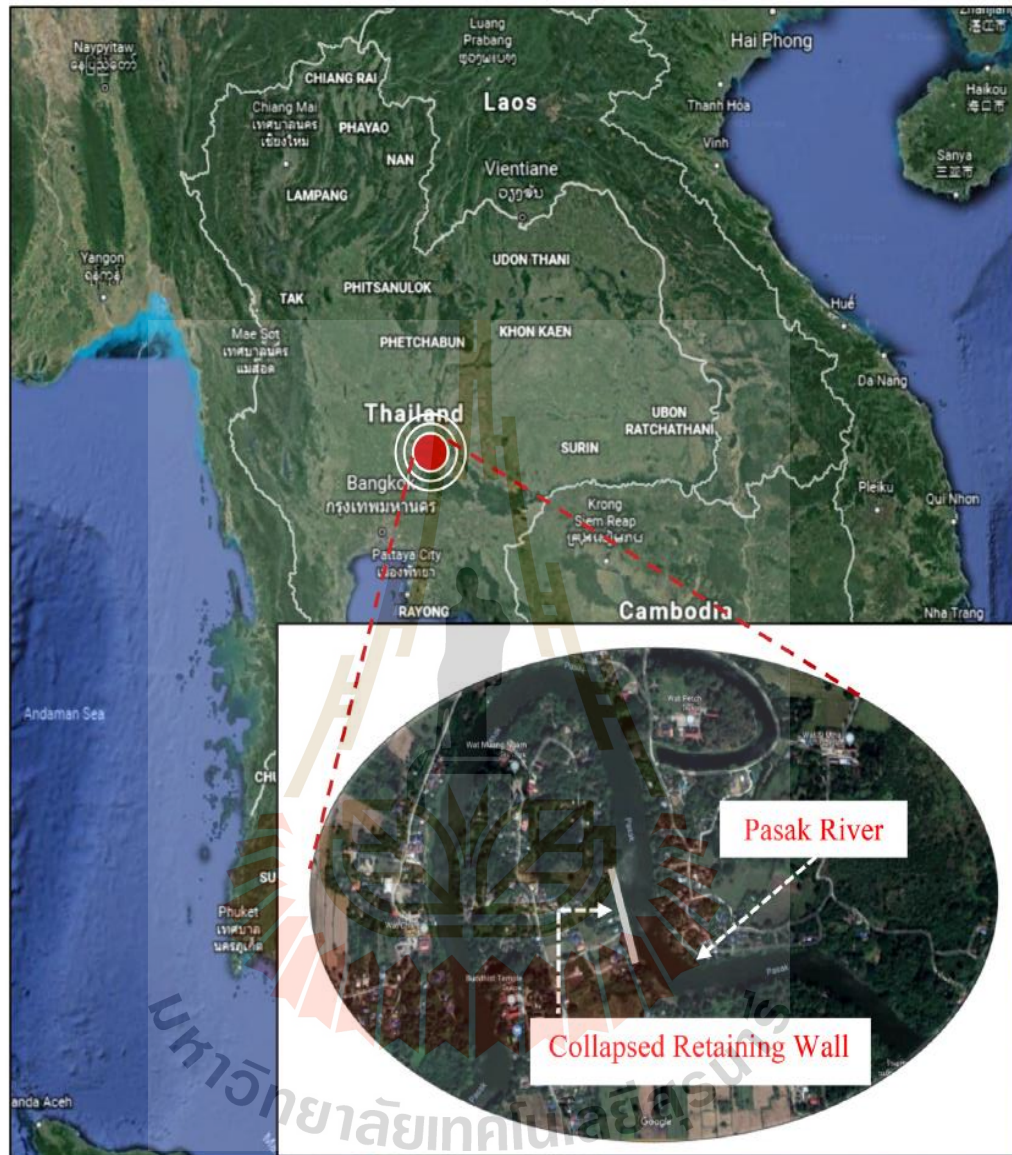
Fig. 8. The location of the collapsed retaining wall.

wall was also found [2,6,20].

3. Remedial approach

3.1. Design concept

The mitigation and rehabilitation of the collapsed riverbank protection structure were designed to minimize the effect of water seepage and steep slope. The new riverbank protection structure was designed based on the three main approaches as follows:

For the first approach, the riverbank protection structure must have an adequate factor of safety against excessive translation, rotation, bearing capacity failure, deep-seated failure, and seepage-induced instability. Hence, the pile-bracing system was proposed. Due to the very dense sandy soil foundation, the bored piles with diameter of 60 cm were selected to have long embedded length (to have high passive lateral resistance) and installed behind the existed driven piles as shown in Fig. 10. The long piles also increased the

Fig. 9. FE analysis of riverbank protection structure with water seepage and eroded slope.

(a)

(b)

Fig. 10. Structural detailing of retaining wall: (a) plan view and (b) side view.

stability against deep-seated failure. The new designed length of piles was approximately 18 m, while the spacing between the front and back of bored piles (longitudinal direction) and (cross section direction) was 5.5 m and 1.2 m, respectively. The reinforced concrete pile caps were constructed on the front and the back bored pile heads, while the steel H-beam were used as bracing between the caps.

The geocomposite as a drainage medium to minimize the water level behind the riverbank protection structure was applied for the second approach. Previous researchers have extensively studied on the geocomposite drainage under seepage condition in earth-retaining structure and reported that the geocomposite drainage reduced the water pressure in the reinforced zone, thus increasing the stability of retaining walls [9,25].

For the third approach, the existing slope was adjusted to be not steeper than 30°. The riprap was designed and installed on the crest and the toe of the adjusted slope in front of the riverbank protection structure in order to protect the erosion problem. The geotextile layer, as a filter medium was installed beneath the riprap layer to separate the natural slope soil and the riprap. The design procedure for the riprap was carried out according to the previous technical paper [13,19], which is based on the local average channel velocity and local depth of the river. The riprap design procedure according to the DPT's regulation [11] can be expressed as follows:

Required design diameter of riprap

$$d = \frac{CV^2}{g(s-1)\Omega} \tag{1}$$

where V = velocity of the river flow, C = coefficient of the river flow, C = 0.3 for low turbulent flow, and C = 0.7 for high turbulent flow; g = gravity acceleration, (g = 9.81), s = specific gravity of riprap, and Ω = side slope correction factor.

Velocity of the river flow (V) can be calculated as:

$$V = \frac{\text{Discharge}}{\text{Area}} = \frac{1500 \, \text{m}^3/\text{s}}{350 \, \text{m}^2} = 4.3 \, \text{m/s} \tag{2}$$

Side slope correction factor (Ω) can be calculated by:

$$\Omega = \left[1 - \frac{\sin^2 \alpha}{\sin^2 \phi} \right]^{1/2} = 0.628 \tag{3}$$

where Friction angle of soil slope $\phi \geq 40°$, angle of slope at the front of retaining wall $\alpha \leq 30°$.

Hence, the required design diameter of riprap was

$$d = \frac{0.3 \times 4.3^2}{9.81 \times (2.65 - 1) \times 0.628} = 0.55 \, \text{m}$$

The required 60 cm diameter of riprap was installed with thickness of 90 cm and 180 cm at the crest and the toe of the slope at the front of the riverbank protection structure, respectively. Fig. 11 shows the structural detailing and the schematic drawing of the riverbank protection structure.

3.2. Finite element verification

The stability of the new riverbank protection structure was verified by FE analysis method using the PLAXIS 2D program. The model parameters used for the backfill soil and for the new riverbank protection structure are summarized in Tables 1 and 3, respectively.
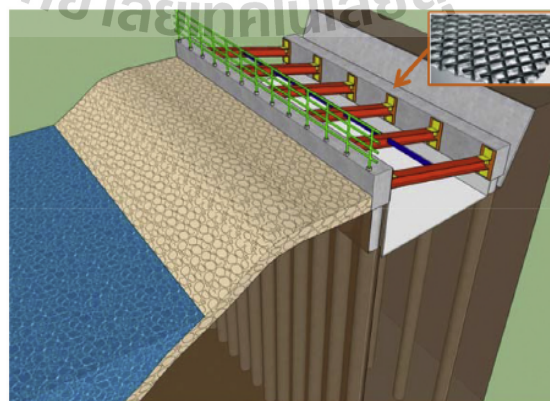
Fig. 11. Schematic drawing of the retaining wall system.

Table 3
Material properties of the bored pile retaining wall structure.

Parameter	Bored pile ($\phi = 0.6$ m)	Strut
Material model	Elastic	Elastic
Young's modulus, E' (kN/m^2)	25.5×10^6	2.04×10^8
Area, A (m^2/m)	0.235	4.99×10^{-3}
Moment of inertia, I (m^4/m)	5.30×10^{-3}	85×10^{-6}
Poisson's ratio, υ'	0.25	0.3
Density, γ (kN/m^3)	23.5	78.5

The effect of water flow in the riverbank protection structure was considered in the simulation by FE analysis. Two cases of water flow condition were considered for FE analysis: the lowest water level in the river at -7 m obtained from the groundwater station (see Fig. 2, water label = 93 m) and rapid drawdown (water level at the bed of the river, water label = 87 m). Due to the variation of water levels in the river seasonally, the reservoir nearby the riverbank protection structure can be subjected to rapid drawdown phenomenon [6]. In this case the lateral water force is removed and the excess pore water pressure does not have enough time to dissipate. According to AASHTO [1], FS must be > 1.5 and 1.3 for the lowest water level in the river and the rapid drawdown conditions, respectively.
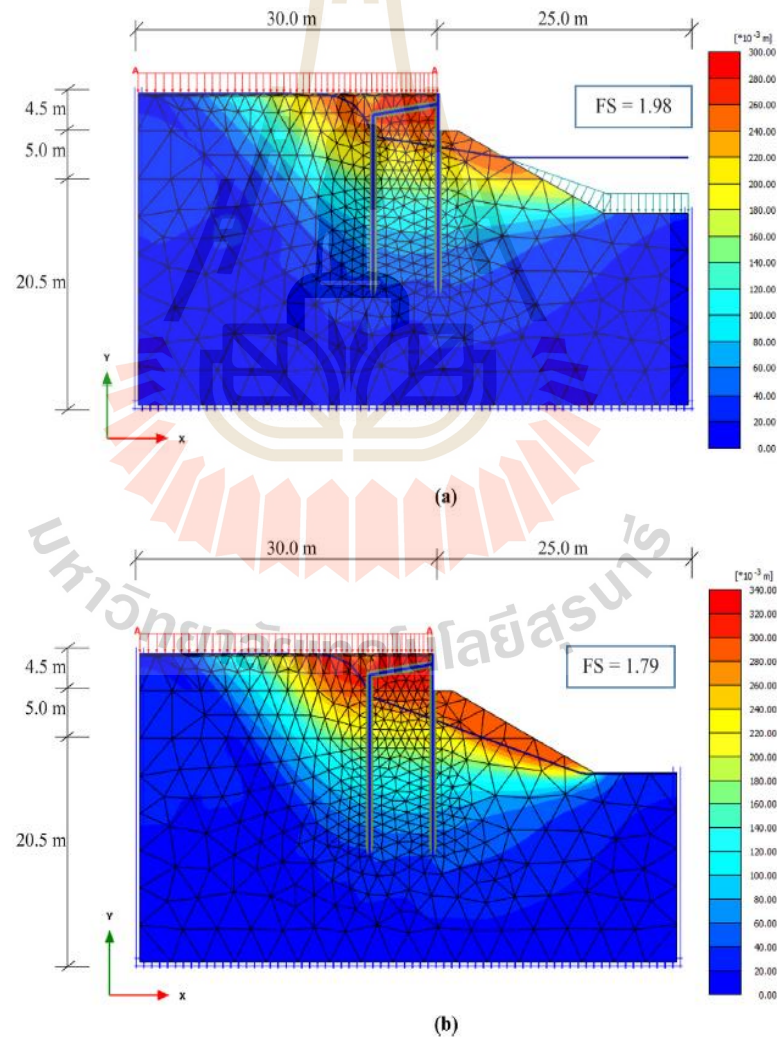
Fig. 12. FE analysis of new riverbank protection structure: (a) lowest water level, and (b) rapid drawdown.

Fig. 12a–b presents the simulation results of FE analyses for both case studies. The FE analysis results based on the c–φ reduction method [5] showed that the FS = 1.98 and 1.79 for case 1 (with the lowest water level) and case 2 (rapid drawdown phenomenon), respectively. FS values for both case studies were greater than the required factor of safety, which demonstrated that the designed riverbank protection structure was stable. The stable new riverbank protection has been constructed in May 2017 and completed in October 2017. Since then, the riverbank protection structure has been serviced without any track of failure.

The cause of failure and its remedial approaches for the riverbank protection structure presented in this paper is helpful for geotechnical engineers, designers, and practitioners alike in terms of assessing suitable site exploration methods and critical analysis methods particularly in tropical regions, where the weather changes seasonally and the serious conditions (flood and drought) may occurred unexpectedly.

4. Conclusions

This paper presents a case study of the collapsed riverbank protection structure and the remedial approach used. The riverbank protection structure has been constructed to protect the riverbank along the Paksak river in Suraburi province, Thailand. However, a part of the riverbank protection structure collapsed during the rainy season. The first and second collapsed riverbank protection structures were anchor retaining wall structure and pile driven retaining wall structure, respectively.

Based on the site investigation and the FE analysis on the collapsed retaining wall, the failure of the riverbank protection structure was caused by the water flow entering into the permeable backfill soil layers and directing to the river. The other reason is that the strong streams continuously scour the riverbank and undermine the natural slope in front of the riverbank protection structure. Erosion changes the geometry of the slope in passive zone, which reduces the resistance of passive earth pressure and ultimately resulting in slope failure.

Therefore, three fundamental approaches have been proposed for the new riverbank protection structure. The bored pile-bracing system was constructed as a new riverbank protection structure. The long and stiff bored piles improve the external stability of the riverbank protection structure. The geocomposite was installed behind riverbank protection structure as a drainage to minimize the water level during rainy season. The riprap was applied on the crest and the toe of the slope in front of the riverbank protection structure to protect the erosion.

The finite element analysis results confirmed that the new riverbank protection structure was stable for both lowest water level in the river and rapid drawn down conditions. This case study of the collapsed riverbank protection structure and its remedial approaches in this paper can be considered as the geotechnical documentary and a guideline or information, which is helpful for the application of earth-retaining structure rehabilitation. The new riverbank protection was constructed in a period of 5 months (May 2017 till October 2017) and since then there has been no evidence of any further failures.

Acknowledgement

References

[1] AASHTO, Standard Specifications for Highway Bridges, 7th ed., American Association of State Highway and Transportation Officials, Inc., Washington (DC), 2002.

[2] M.A.M. Abdullahi, Evaluation of causes of Retaining Wall failure, Leonardo 14 (2009) 11–18.

[3] H. Binici, H. Temiz, C. Kayadelen, H. Kaplan, M.Y. Durgun, Retaining Wall failure due to poor construction and design aspects a case study, Electron. J. Construct. Technol. 6 (1) (2010).

[4] M. Bolton, The strength and dilatancy of sands, Géotechnique 36 (1) (1986) 65–78.

[5] R. Brinkgreve, W. Broere, PLAXIS 2D Reference Manual 2015. *Delft, Netherlands 2010,* (2015).

[6] M. Budhu, Soil Mechanics And Foundations, (With CD), John Wiley & Sons, 2008.

[7] J.-C. Chai, M. Julfikar Hossain, J. Carter, S.-L. Shen, Cone penetration-induced pore pressure distribution and dissipation, Comput. Geotech. 57 (2014) 105–113, http://dx.doi.org/10.1016/j.compgeo.2014.01.008.

[8] J.-C. Chai, J.S.-L. Shen, M.D. Liu, D.-J. Yuan, Predicting the performance of embankments on PVD-improved subsoils, Comput. Geotech. 93 (2018) 222–231, http://dx.doi.org/10.1016/j.compgeo.2017.05.018.

[9] A. Chinkulkijniwat, S. Horpibulsuk, D.B. Van, A. Udomchai, R. Goodary, A. Arulrajah, Influential factors affecting drainage design considerations for mechanical stabilised earth walls using geocomposites, Geosynth. Int. 24 (3) (2017) 224–241, http://dx.doi.org/10.1680/jgein.16.00027.

[10] J. Dickens, P. Walker, Use of distinct element model to simulate behaviour of dry-stone walls, Struct. Eng. Rev. 8 (2–3) (1996) 187–199.

[11] DPT, Dam Protection Design, Department of Public Works and Town & Country Planning, Thailand, 2006.

[12] C.-C. Fan, Y.-S. Fang, Numerical solution of active earth pressures on rigid retaining walls built near rock faces, Comput. Geotech. 37 (7) (2010) 1023–1029, http://dx.doi.org/10.1016/j.compgeo.2010.08.004.

[13] V. Galay, E. Yaremko, M. Quazi, River bed scour and construction of stone riprap protection, Sediment Transfer in Gravel-Bed Rivers, *John Wiley & Sons, New York,* 1987(p 353–379, 1 tab, 19 fig, 41 ref).

[14] R.M. Harkness, W. Powrie, X. Zhang, K.C. Brady, M.P. O'Reilly, Numerical modelling of full-scale tests on drystone masonry retaining walls, Géotechnique 50 (2) (2000) 165–179, http://dx.doi.org/10.1680/geot.2000.50.2.165.

[15] S. Horpibulsuk, C. Suksiripattanapong, A. Niramitkornburee, A. Chinkulkijniwat, T. Tangsutthinon, Performance of an earth wall stabilized with bearing reinforcements, Geotext. Geomembr. 29 (5) (2011) 514–524, http://dx.doi.org/10.1016/j.geotexmem.2011.05.002.

[16] C.-C. Huang, W.-M. Luo, Behavior of soil retaining walls on deformable foundations, Eng. Geol. 105 (2009) 1), 1–10, http://dx.doi.org/10.1016/j.enggeo.2009.01.003.

[17] H.-M. Lyu, J. Shen, A. Arulrajah, Assessment of geohazards and preventative countermeasures using AHP incorporated with GIS in Lanzhou, China, Sustain. For. 10 (2) (2018) 304.

[18] H.-M. Lyu, W.-J. Sun, S.-L. Shen, A. Arulrajah, Flood risk assessment in metro systems of mega-cities using a GIS-based modeling approach, Sci. Total Environ. 626 (2018) 1012–1025, http://dx.doi.org/10.1016/j.scitotenv.2018.01.138.

[19] S.T. Maynord, J.F. Ruff, S.R. Abt, Riprap design, J. Hydraul. Eng. *115* (7) (1989) 937–949, http://dx.doi.org/10.1061/(ASCE)0733-9429(1989)115:7(937).

[20] W.M. Rankine, On the stability of loose earth, Philos. Trans. R. Soc. Lond. 147 (1857) 9–27.

[21] S.-L. Shen, H.-N. Wu, Y.-J. Cui, Z.-Y. Yin, Long-term settlement behaviour of metro tunnels in the soft deposits of Shanghai, Tunn. Undergr. Space Technol. 40 (2014) 309–323, http://dx.doi.org/10.1016/j.tust.2013.10.013.

[22] S.L. Shen, Z.F. Wang, W.C. Cheng, Estimation of lateral displacement induced by jet grouting in clayey soils, Géotechnique 67 (7) (2017) 621–630, http://dx.doi.org/10.1680/jgeot.16.P.159.

[23] K. Sukmak, P. Sukmak, S. Horpibulsuk, A. Chinkulkijniwat, A. Arulrajah, S.-L. Shen, Pullout resistance of bearing reinforcement embedded in marginal lateritic soil at molding water contents, Geotext. Geomembr. 44 (3) (2016) 475–483, http://dx.doi.org/10.1016/j.geotexmem.2015.07.016.

[24] K. Sukmak, P. Sukmak, S. Horpibulsuk, J. Han, S.-L. Shen, A. Arulrajah, Effect of fine content on the pullout resistance mechanism of bearing reinforcement embedded in cohesive–frictional soils, Geotext. Geomembr. 43 (2) (2015) 107–117, http://dx.doi.org/10.1016/j.geotexmem.2014.11.010.

[25] A. Udomchai, A. Chinkulkijniwat, S. Horpibulsuk, Physical model tests on Mechanically stabilized earth walls with geocomposite drainage under seepage condition, *Geosynthetics Asia (2012) Proceeeding of the 5th Asian Regio-nal Conference on Geosynthetics,* Bangkok, Thailand, 2012, pp. 613–616.

[26] H. Vidal, The principle of reinforced earth, Highw. Res. Rec. 282 (1969).

[27] Vidal, H. (1978). Stabilized earth structures: Google Patents.

[28] B. Villemus, J. Morel, C. Boutin, Experimental assessment of dry stone retaining wall stability on a rigid foundation, Eng. Struct. 29 (9) (2007) 2124–2132.

[29] M.-S. Won, Y.-S. Kim, Internal deformation behavior of geosynthetic-reinforced soil walls, Geotext. Geomembr. 25 (1) (2007) 10–22, http://dx.doi.org/10.1016/j.geotexmem.2006.10.001.

[30] Y. Yu, I.P. Damians, R.J. Bathurst, Influence of choice of FLAC and PLAXIS interface models on reinforced soil–structure interactions, Comput. Geotech. 65 (2015) 164–174 https://doi.org/10.1016/j.compgeo.2014.12.009.

[31] J. Zomberg, D. Leshchinsky, Comparison of international design criteria for geosynthetic-reinforced soil structures, Landmarks Earth Reinforce. 2 (2003) 1095–1106.

[32] P. Jamsawang, P. Voottipruex, P. Boathong, W. Mairaing, S. Horpibulsuk, Three-dimensional numerical investigation of lateral movement and factor of safety of slopes stabilized with deep cement mixing column rows, Eng. Geol. 188 (2015) 159–167.
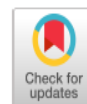
Predicting Pullout Resistance of Bearing Reinforcement Embedded in Cohesive-Frictional Soils

Gampanart Sukmak, Ph.D.[1]; Patimapon Sukmak, Ph.D.[2]; Apichet Joongklang[3]; Artit Udomchai[4]; Suksun Horpibulsuk[5]; Arul Arulrajah[6]; and Chakkrit Yeanyong[7]

Abstract: Bearing reinforcement is an inextensible reinforcement type that is manufactured by welding strongly between a longitudinal member and a set of transverse members. The pullout capacity of the bearing reinforcement comprises both friction and bearing components. In this research study, the test results of residual red clay and previously published test results were analyzed to develop rational pullout predictive equations. The pullout friction resistance can be calculated by utilizing the soil-reinforcement interaction factor, α, which reduces linearly with fines content (F). The bearing pullout resistance is controlled in the failure plane of transverse member (β) and transverse members interference factor (IF). The water content to optimum water content ratio, w/w_{owc} and F, were found to be dominant factors controlling both β and IF. The β reduced from $\pi/2$ to $\pi/3$ with the increase in w/w_{owc} and F. The transverse members interference zone was larger for lower w/w_{owc} and F. Equations for predicting β and IF, in terms of the fines content and water content, are proposed in this paper. **DOI: 10.1061/(ASCE)MT.1943-5533.0003043.** © *2019 American Society of Civil Engineers.*

Author keywords: Pullout resistance; Bearing reinforcement; Cohesive-frictional soil; Fines content; Water content.

Introduction

Mechanical stabilized earth (MSE) walls have been proven to be effective retaining structures in infrastructure applications (Horpibulsuk et al. 2011; Udomchai et al. 2017). The reinforcement types are classified into inextensible (i.e., steel strips and steel grid) and extensible (i.e., geotextile and geogrid) materials. Both types of reinforcement minimize the horizontal movement of the MSE wall (Jiang et al. 2016; Liu 2012; Mohamed et al. 2013; Palmeira 2004; Roodi Gholam and Zornberg Jorge 2017). The reinforcement can also be placed at base of an embankment on soft soil to improve the stability of the foundation (Bonaparte and Christopher 1987; Chai et al. 2002; Jewell 1988; Zhang et al. 2015).

Bearing reinforcement [Fig. 1(a)] developed by Horpibulsuk and Niramitkronburee (2010) is an inextensible reinforcement type. The effectiveness of the bearing reinforcement has been examined based on large-scale pullout testing [Fig. 1(b)], field-scale testing, and numerical simulation testing. Bearing reinforcement earth (BRE) walls have been successfully implemented in many construction projects in Thailand. Based on AASHTO (2002) specification, the design method of MSE walls was proposed for high-quality friction (coarse-grained) backfill, which specifies a fines content (<0.075 mm), F, of less than 15% and a plasticity index of less than 6%.

Due to economic and environmental factors, the marginal cohesive-frictional soil ($F > 15\%$) abundant in Thailand is typically used for infrastructure activities after soil improvement (Sukmak et al. 2013; Phummiphan et al. 2016; Donrak et al. 2018). In practice, the clayey soil can be used as a backfill material if its compacted water content and density are close to the optimum water content and 95% of maximum density, respectively, obtained from the laboratory. Also during service, the MSE wall must be protected from seepage of water such as rain and ground water by providing a geotextile as a drainage layer to minimize the expansion of the backfill. Locally available clay stone has been successfully used in constructing MSE walls (Udomchai et al. 2017). Previous studies (Sukmak et al. 2015; Horpibulsuk et al. 2016) investigated the influence of fines content on the pullout capacity of bearing reinforcement. However, these two research studies apply only to compacted soils at the optimum water content (w_{owc}) and maximum dry unit weight. Sukmak et al. (2016) studied the effect of water content on pullout capacity in compacted clayey sand.

Reanalysis of the available test results, taking into account the effect of fines and water content for developing generalized pullout resistance predictive equations, is innovative. To improve understanding, a pullout test result of red clay from this study is also analyzed. The studied water content of red clay is in the range of $w_{owc} \pm 2.5\%$, specified for field compaction according to the

[1]Lecturer, School of Engineering and Technology, and Center of Excellence in Sustainable Disaster Management, Walailak Univ., 222 Thaiburi, Thasala District, Nakhonsithammarat 80161, Thailand. Email: gampanart.su@wu.ac.th

[2]Assistant Professor, School of Engineering and Technology, and Center of Excellence in Sustainable Disaster Management, Walailak Univ., 222 Thaiburi, Thasala District, Nakhonsithammarat 80161, Thailand. Email: patimapon.su@wu.ac.th

[3]M.Eng. Graduate, School of Civil Engineering, Suranaree Univ. of Technology, Nakhon Ratchasima 30000, Thailand. Email: apichet.joong@gmail.com

[4]Ph.D. Scholar, School of Civil Engineering, Suranaree Univ. of Technology, Nakhon Ratchasima 30000, Thailand. Email: artit.u@sut.ac.th

[5]Professor, School of Civil Engineering and Director, Center of Excellence in Innovation for Sustainable Infrastructure Development, Suranaree Univ. of Technology, Nakhon Ratchasima 30000, Thailand (corresponding author). ORCID: https://orcid.org/0000-0003-1965-8972. Email: suksun@g.sut.ac.th

[6]Professor, Dept. of Civil and Construction Engineering, Swinburne Univ. of Technology, Hawthorn, VIC 3122, Australia. Email: aarulrajah@swin.edu.au

[7]Postgraduate Researcher, Center of Excellence in Innovation for Sustainable Infrastructure Development, Suranaree Univ. of Technology, Nakhon Ratchasima 30000, Thailand. Email: armyjubu@gmail.com

© ASCE   04019379-1   J. Mater. Civ. Eng.

J. Mater. Civ. Eng., 2020, 32(3): 04019379
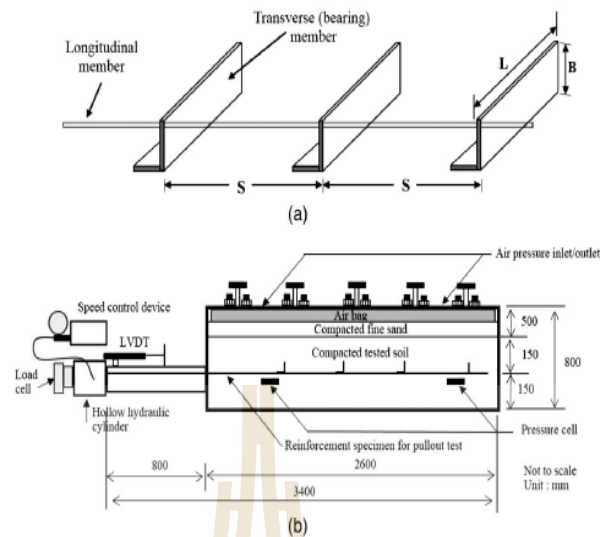
Fig. 1. (a) Typical schematic view of the bearing reinforcement; and (b) pullout test apparatus. (adapted from Horpibulsuk and Niramitkronburee 2010).

specification of Department of Highways (DOH), Thailand. For compacted unsaturated soils, the total stress analysis is reasonable to describe the shear behavior and is acceptable in practice (Bergado et al. 1996; Liu et al. 2009; Sukmak et al. 2016, 2015). The outcome of this research will lead to the use of in situ soil for BRE walls, which can substantially reduce costs associated with long-distance haulage of imported virgin materials.

Theoretical Background

The total pullout capacity of bearing reinforcements is composed of the friction pullout and the bearing pullout capacities. The friction pullout capacity of longitudinal member (without any transverse member), P_f, is expressed in the form of

$$P_f = \pi D L_e \alpha (c + \sigma_n \tan \phi) \quad (1)$$

where α = interaction factor; c and ϕ = total strength parameters; σ_n = applied normal stress; D = diameter of longitudinal member; and L_e = embedded length.

The bearing pullout capacity, P_{bn}, of the transverse members, which are placed at regular intervals, is expressed as

$$P_{bn} = n I F P_{b1} \quad (2)$$

where n = number of transverse members; IF = transverse members interference factor; and P_{b1} = pullout capacity contributed from a transverse member.

Typically, B is smaller than 40 mm, while L is larger than 150 mm (refer to Fig. 1). The L/B value for the transverse members is therefore more than 3.7. During the pullout, the 3-D deformation might happen around the transverse members. Previous studies (Horpibulsuk and Niramitkronburee 2010; Horpibulsuk et al. 2016) reported that within this L/B range, the 3-D effect on the pullout capacity is insignificant. The P_{b1} can be approximated using the following equations:

$$P_{b1} = [c N_c + \sigma_n N_q] \quad (3)$$

$$N_q = \frac{1}{\cos \varphi} \exp[2\beta \tan \phi] \tan \left(\frac{\pi}{4} + \frac{\phi}{2} \right) \quad (4)$$

$$N_c = \frac{1}{\sin \phi} \exp[2\beta \tan \phi] \tan \left(\frac{\pi}{4} + \frac{\phi}{2} \right) - \cot \phi \quad (5)$$

where β = failure angle (radian).

Extensive test results (Suksiripattanapong et al. 2013; Sukmak et al. 2015, 2016) previously reported that β was dependent on F and water content ratio (w/w_{owc}), where w is water content and w_{owc} is the optimum water content. When the β values are $\pi/1.65$ and $\pi/3$, the failure modes are general shear (Perterson and Anderson 1980) and punching shear (Jewell et al. 1984) mechanisms, respectively.

The transverse members interference factor (IF) is strongly governed by the transverse members spacing (S) and B, regardless of L (Horpibulsuk and Niramitkronburee 2010; Sukmak et al. 2016, 2015; Suksiripattanapong et al. 2013). The failure mechanism was classified into three failure characteristics: block, interference, and individual, depending on the S/B value as shown in Fig. 2. The S_1/B is the spacing ratio dividing the block and the interference failure zones. S_2/B is the spacing ratio dividing the interference and individual failure zones.

Based on extensive past test results, S_1/B can be taken as 3.75 for a wide range of fines contents (Sukmak et al. 2015, 2016; Horpibulsuk et al. 2016). Sukmak et al. (2015) reported that a lower shear strength results in a smaller softened region, and hence a lower S_2/B value. The IF is equal to $1/n$ when $S/B < S_1/B$ (block failure) and 1 when $S/B > S_2/B$ (individual failure). When $S_1/B < S/B < S_2/B$, the IF can be determined from the logarithm of S/B as follows:

$$IF = a + b \ln \left(\frac{S_2}{B} \right) \quad (6)$$

© ASCE   04019379-2   J. Mater. Civ. Eng.

J. Mater. Civ. Eng., 2020, 32(3): 04019379
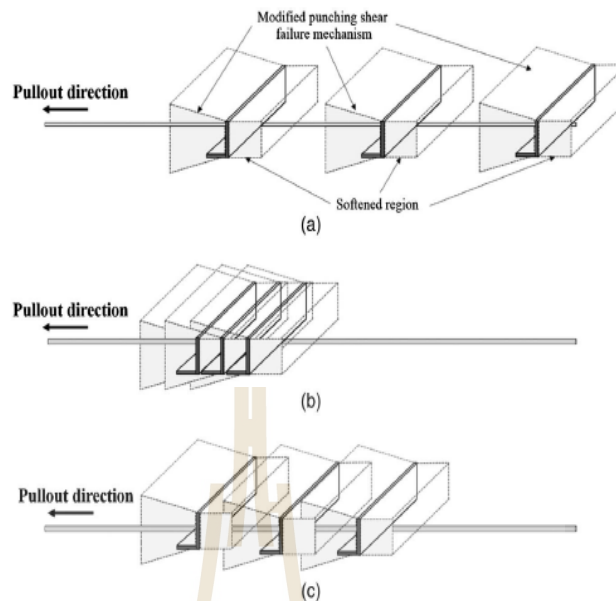
Fig. 2. Transverse members interference: (a) individual failure; (b) block failure; and (c) interference failure. [Reprinted from *Geotextiles and Geomembranes*, Vol. 43 (2), K. Sukmak, P. Sukmak, S. Horpibulsuk, J. Han, S.-L. Shen, and A. Arulrajah, "Effect of Fine Content on the Pullout Resistance Mechanism of Bearing Reinforcement Embedded in Cohesive–Frictional Soils," pp. 107–117, © 2015, with permission from Elsevier.]

$$b = \frac{[1 - \frac{1}{n}]}{[\ln(\frac{S_2}{B}) - 1.322]} \quad (7)$$

$$a = 1 - b\ln\left(\frac{S_2}{B}\right) \quad (8)$$

The dimension (n, B, L, and S) of the transverse members is determined based on the internal stability design method of the BRE wall suggested by Horpibulsuk and Niramitkronburee (2010) for coarse-grained backfill and Udomchai et al. (2017) for fine-grained backfill. The pullout resistance of each reinforcement must provide high enough capacity against pullout failure due to the dead load and live load with a factor of safety >1.5. Typically, the vertical spacing of the MSE wall is 750 mm, as suggested by AASHTO (2002), to provide satisfactory interaction between the backfill and the reinforcements. For the BRE wall, the reinforcement is connected to the wall facing by a locking bar and the vertical spacing is 750 and 350 mm depending upon the height of the BRE wall. The dimension of segmental concrete facing panels is $1.50 \times 1.50 \times 0.14$ m. The reasonable interaction between backfill and reinforcement in the BRE wall has been illustrated by Horpibulsuk et al. (2011) for coarse-grained backfill and Udomchai et al. (2017) for fine-grained backfill.

Materials and Methods

Soil Samples

The tests were conducted on residual red clay soil containing 98% of fines content collected from the Mae Moh mine, Thailand. The grain size distribution curve of red clay is shown in Fig. 3(a). The red clay was a low-quality soil with high plasticity (CH).

The compaction characteristic under standard Proctor energy [ASTM D698-91 (ASTM 1995)] was $w_{owc} = 16\%$ and maximum dry unit weight, $\gamma_{d,max} = 17.61$ kN/m³. The soil samples were prepared according to Sukmak et al. (2016) for both direct shear and pullout tests at different water contents, w, which were $w_1 = 12\%$, $w_2 = 14\%$, w_{owc} ($w_3 = 16\%$), $w_4 = 18\%$, and $w_5 = 20\%$, as shown in Fig. 3(b). The degrees of saturation, S_r, corresponding to w_1, w_2, w_3, w_4, and w_5 were 59%, 70%, 83%, 85%, and 88%, respectively.

A large direct shear test (Sukmak et al. 2015) was performed on red clay samples at w_1, w_2, w_3, w_4, and w_5 and at their corresponding dry unit weight. The physical and engineering properties are summarized in Table 1.

Bearing Reinforcement

The B values were 25, 40, and 50 mm, and the L values were 100, 150, and 200 mm. The S values varied from 150 to 1,500 mm. The n values were 1 to 4, which are typical in practice. The welding strength between longitudinal and transverse members was designed to sustain loads not less than the tensile strength of the longitudinal member.

Methodology

The detail of the pullout test apparatus and the procedure of the pullout testing have been explanted by Horpibulsuk and Niramitkronburee (2010). The soil was compacted to achieve the maximum dry unit weight using a vibratory compactor. A compacted soil of 300-mm thick was kept above and below the reinforcement [Fig. 1(b)]. Three samples were tested at a pullout rate of 1.0 mm/min under the same conditions to ensure consistency of test results. The results under the same testing conditions were reproducible with a low SD/x < 10%, where x is

© ASCE 04019379-3 J. Mater. Civ. Eng.

J. Mater. Civ. Eng., 2020, 32(3): 04019379
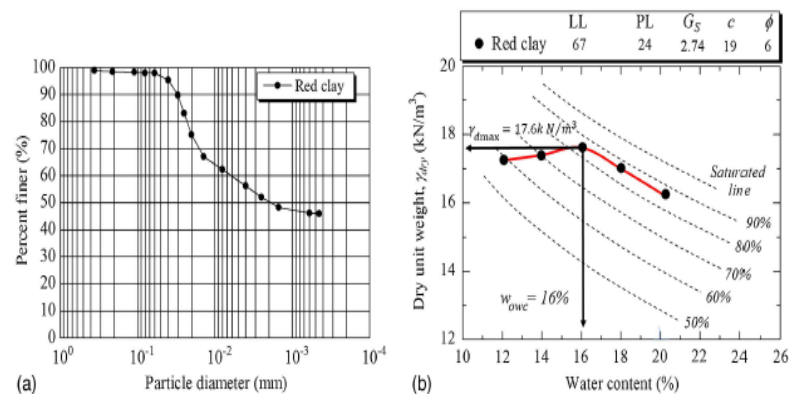
Fig. 3. (a) Compaction curve of red clay; and (b) grain size distribution of red clay.

Table 1. Physical and engineering properties of red clay

Properties of red clay	w_1	w_2	w_3	w_4	w_5
Dry density, γ_{dry} (kN/m³)	17.25	17.40	17.60	17.00	15.85
Water content (%)	12	14	16	18	20
Degree of saturation, S_r (%)	59	70	83	85	88
Relative degree of compaction (%)	96.36	98.63	100	98.63	96.36
Water content ratio	0.75	0.88	1.00	1.13	1.25
Angle of internal friction, ϕ	13	11	6	5	4
Cohesion, c (kPa)	22	21	19	14	8

mean strength value and SD is mean standard deviation. Besides the red clay, the data from previous research (Sukmak et al. 2015, 2016; Horpibulsuk et al. 2016) were taken and reanalyzed to develop the generalized equations for assessing pullout resistance at various water contents and fines contents.

Test Results and Discussion

Shear Strength of Compacted Backfills

Fig. 4 shows the role of w and F on undrained shear strength of red clay compared with other soils. Fig. 4(a) summarizes the change in shear strength and F for clayey sands compacted at their w_{owc}. It was evident that $F = 45\%$ was the threshold limit at which the shear strength sharply decreases with F. The change of shear strength with F was relatively small when $F < 45\%$ but was significantly larger when $F > 45\%$. The large decrease in shear strength was clearly noted with higher normal stress. The sudden change in shear strength when $F > 45\%$ is because, at this condition, the void spaces are filled with fines grains that govern the shear response (Wang et al. 2009). The large amount of fines grains cause the sliding of coarse grains over each other; hence, the decrease in internal friction angle.

Figs. 4(b and c) show the shear strength versus water content ratios (w/w_{owc}) plot for lateritic soil ($F = 20.3\%$) and red clay ($F = 98\%$), respectively. The shear strength of both soils declines with the increment of water content ratio. The reduction in shear strength was small for low F [Fig. 4(b)] but very large for high F [Fig. 4(c)]. The linear relationship between shear strength and w/w_{owc} is observed for red clay. This understanding of shear strength change is essential for BRE wall design, as the shear strength controls the pullout resistance.

Friction Pullout Capacity

Fig. 5 shows the friction force versus displacement plot of a longitudinal member embedded in red clay. The sharp increase in friction force is observed until the peak value, $P_{f,peak}$, and the friction force subsequently level off. The friction pullout force at the end of the test is herein defined as the residual friction pullout force, $P_{f,residual}$. The displacement corresponding to $P_{f,peak}$ was found at 3–5 mm for all tests. The $P_{f,peak}$ and $P_{f,residual}$ at various normal stresses depend on the water content. The $P_{f,peak}$ and $P_{f,residual}$ values significantly decline with the increase in water content because of the significant reduction in shear strength [Fig. 4(c)].

Fig. 6 shows the plots between the interaction factors versus shear strength. From a linear regression analysis, the peak and residual interaction factors (α_p and α_r) of red clay ($F = 98\%$) are 0.66 and 0.47, respectively, for all water content tested. These values are close to those ($\alpha_p = 0.63$ and $\alpha_r = 0.46$) studied by Sukmak et al. (2015) for high plasticity clay (CH and $F = 98\%$). Based on the study presented here and previous research (Sukmak et al. 2015; Horpibulsuk et al. 2016), the α_p and α_r for a particular soil are constant for water contents. Sukmak et al. (2016) have proposed a relationship between α_p and α_r versus F as follows:

$$\alpha_p = -0.002F + 0.859 \quad \text{for } 20 < F < 98\% \quad (9)$$

$$\alpha_r = -0.0014F + 0.592 \quad \text{for } 20 < F < 98\% \quad (10)$$

Both equations are recommended as a quick tool for predicting α_p and α_r at various fines contents and water contents.

© ASCE   04019379-4   J. Mater. Civ. Eng.

J. Mater. Civ. Eng., 2020, 32(3): 04019379
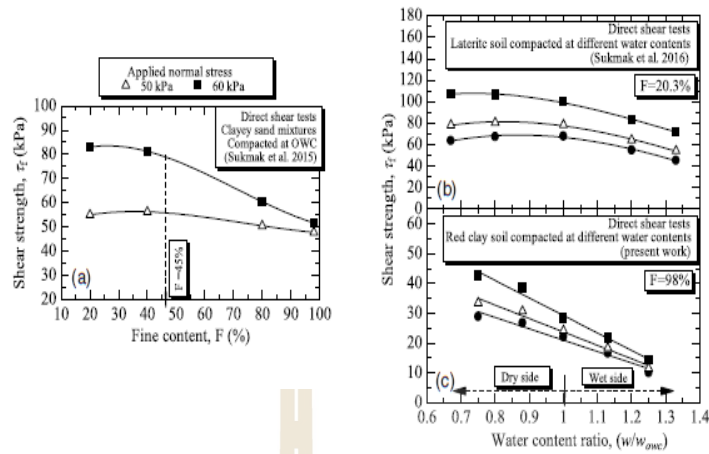
Fig. 4. (a) Relationship between shear strength versus fine content of compacted soils at optimum water content (data from Sukmak et al. 2015); (b) relationships between shear strength and water content ratios (w/w_{owc}) of lateritic soil (data from Sukmak et al. 2016); and (c) relationships between shear strength and water content ratios (w/w_{owc}) of red clay.
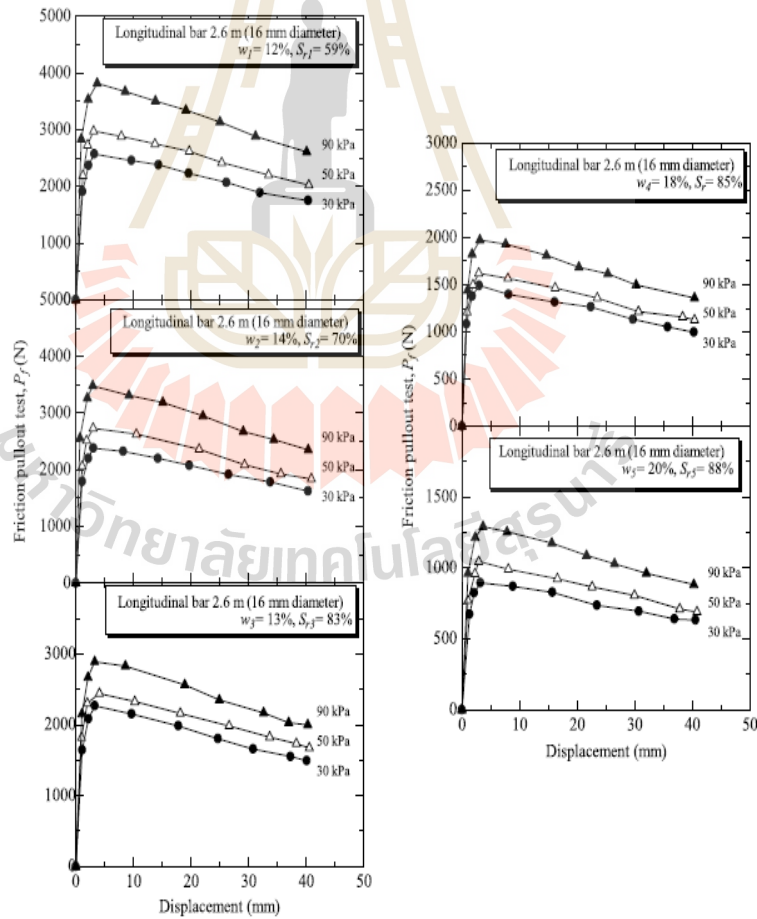
Fig. 5. Pullout test results of a longitudinal member under different normal stresses.

© ASCE   04019379-5   J. Mater. Civ. Eng.

J. Mater. Civ. Eng., 2020, 32(3): 04019379
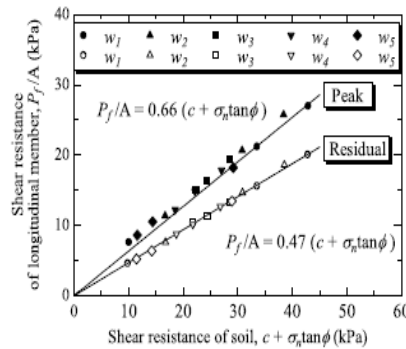
Fig. 6. Relationship between shear interface and shear strength.

Bearing Pullout Capacity

Bearing Pullout Capacity for $n = 1$

The measured bearing capacity, σ_{bmax}, for $n = 1$ for the red clay, with various dimensions (B and L) of transverse member and normal stresses is shown in Fig. 7. By using the generalized equation [Eqs. (3)–(5)] to predict σ_{bmax}, the β value of $\pi/3$ can satisfactorily fit all the test data of compacted red clay. This implies that the failure mechanism for red clay is punching shear for all water contents.

The analysis of the present and previous data (Sukmak et al. 2015, 2016; Horpibulsuk et al. 2016) leads to the 3-D plot of β versus F and w/w_{owc}, as shown in Fig. 8. The plot was made from the following three assumptions:

1. At $w = w_{owc}$, $F = 45\%$ is the threshold limit separating small and large change in bearing pullout resistance with F (Sukmak et al. 2015).

2. On the dry side of optimum and at w_{owc}, the β is identical and can be determined from the following equation (Sukmak et al. 2015):

$$\beta_{(rad)} = [-0.00002F^2 + 0.0002F + 0.505]\pi$$
$$\text{for } 20 < F < 98\% \tag{11}$$

3. On the wet side of optimum, β reduces significantly with increasing w/w_{owc} until $\beta = \pi/3$ (punching shear) at $w/w_{owc} = 1.33$ (Sukmak et al. 2016; Horpibulsuk et al. 2016; present study data). Therefore, the β at any w/w_{owc} can be approximated using interpolation method where the β at $w/w_{owc} = 1$ can be determined from Eq. (11).

With the known β value determined from Fig. 8, the P_{b1} can be determined using Eqs. (3)–(5).

Bearing Pullout Capacity of Bearing Reinforcement ($n > 1$)

Fig. 9 illustrates the relationship between IF and S/B at various w/w_{owc} and n for red clay. It was evident that the S_1/B value was practically the same of 3.75 for all w and n tested, which agrees with previous studies (Sukmak et al. 2015, 2016; Horpibulsuk et al. 2016). The S_2/B value is essentially the same of 13.3 for $w \leq w_{owc}$, whereas the S_2/B value for $w > w_{owc}$ decreases linearly with increasing water content. The analysis of the previous and present studies results in the 3-D plot of S_2/B versus F and w/w_{owc}, as
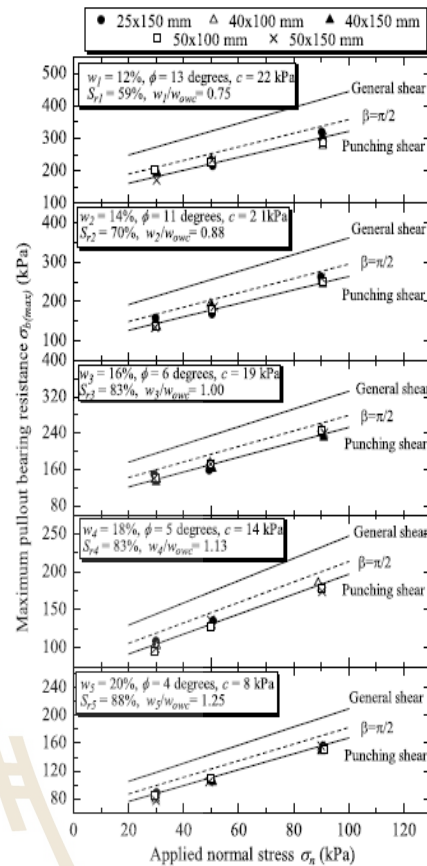
Fig. 7. Maximum pullout bearing resistance of a single isolated transverse member at various water contents.
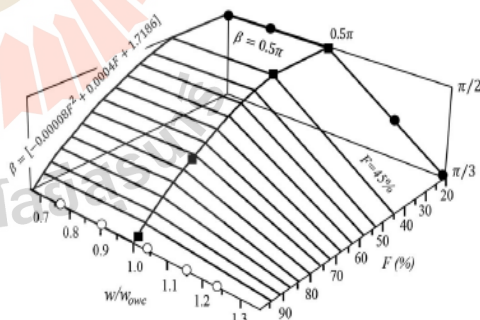
Fig. 8. Plot of β versus F and w/w_{owc}. (Data from Sukmak et al. 2015, 2016.)

shown in Fig. 10. The following assumptions were made for the development of Fig. 10:

1. At $w/w_{owc} = 1$, S_2/B can be determined using the following equation proposed by Sukmak et al. (2015):

© ASCE   04019379-6   J. Mater. Civ. Eng.

J. Mater. Civ. Eng., 2020, 32(3): 04019379
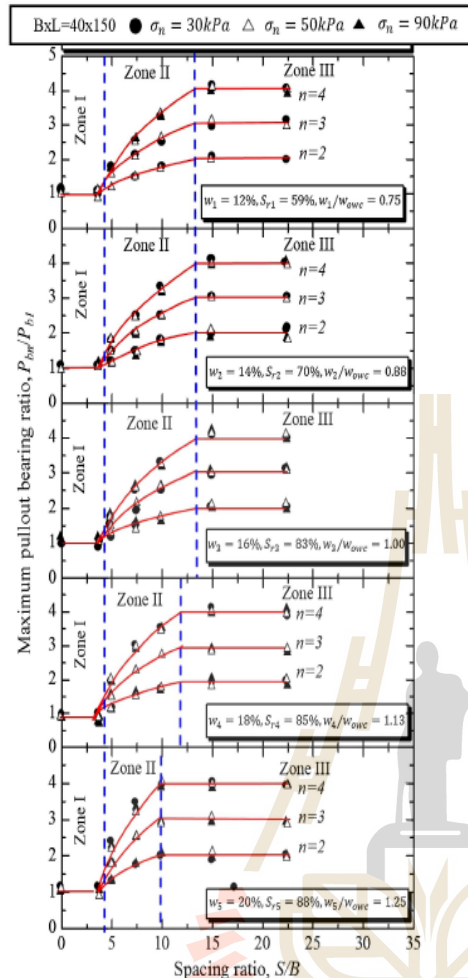
Fig. 9. IF and S/B relationship for 40×150 mm transverse members (Zone I: block failure; Zone II: interference failure; and Zone III: individual failure).

$$(S_2/B)_{owc} = -0.121F + 25.16 \quad (12)$$

2. On the dry side and at w_{owc}, S_2/B is identical and can be approximated using Eq. (12).
3. On the wet side, the relationship between S_2/B and w/w_{owc} at a given F can be determined from

$$(S_2/B)_F = c(w/w_{owc}) + d \quad (13)$$

where c and d are constant. The c values are -30.7 and -12.81 for $F = 20\%$ and 98%, respectively. The c values at various F can thus be approximated from an interpolation using c values at $F = 20\%$ and 98%. The d value can be calculated from the known S_2/B value at $w/w_{owc} = 1$ determined by Eq. (12).

Once S_2/B is known, IF can be determined using Eqs. (6)–(8). Therefore, the P_{bn} at various S/B and n can be determined from Eq. (2).
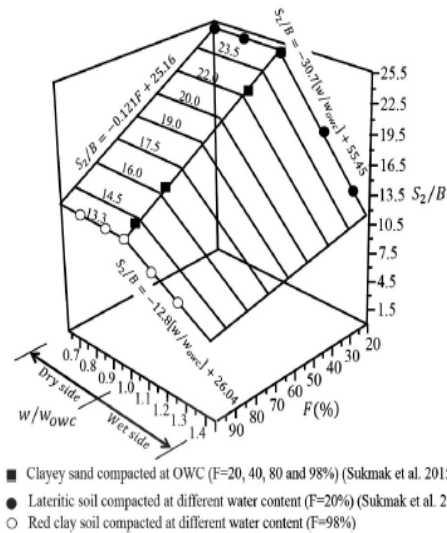
Fig. 10. Plot of S_2/B versus F and w/w_{owc}. (Data from Sukmak et al. 2015, 2016.)

Recommended Method for Predicting Pullout Resistance

A stepwise procedure for assessing pullout bearing resistance for various water contents and fines contents is proposed below.

Calculate Friction Pullout Capacity of Bearing Reinforcement

1. Perform sieve, compaction, and strength tests on the backfill material to determine F, w_{owc}, and shear strength parameters.
2. Calculate α for the friction pullout resistance, which can be directly obtained from a pullout test on a longitudinal member or approximated from Eq. (9).
3. Calculate P_f at required normal stress level from Eq. (1).

Calculate Bearing Pullout Capacity of Bearing Reinforcement

4. Calculate β at required w and F using Fig. 8.
5. Calculate the N_c and N_q values using Eqs. (4) and (5).
6. Calculate P_{b1} from $P_{b1} = N_q \sigma_n BL$.
7. Calculate the S_2/B using Fig. 9.
8. Calculate IF at required n, S, B, and L. Eqs. (6)–(8) are used when $S_1/B < S/B < S_2/B$.
9. Calculate P_{bn} from $P_{bn} = nIFP_{b1}$.

Calculate Pullout Capacity of Bearing Reinforcement

10. Calculate the pullout resistance $= P_f + P_{bn}$.

Conclusions

This research investigated the combined effects of fines and water contents on the pullout capacity of bearing reinforcement. Conclusions are summarized as follows:

1. The total pullout resistance of the bearing is the sum of friction pullout and bearing pullout resistances. Lower water content resulted in higher shear strength; hence, higher P_f. The α_p and

© ASCE   04019379-7   J. Mater. Civ. Eng.

J. Mater. Civ. Eng., 2020, 32(3): 04019379

α_r values were dependent on F, irrespective of water content. The relationships between α_p and α_r versus F were suggested in this paper. The relationships between α_p and α_r versus F are $\alpha_p = -0.002F + 0.859$ and $\alpha_r = -0.0014F + 0.592$, respectively.

2. The bearing pullout resistance of transverse members P_{bn} is calculated in terms of the number of transverse members (n), transverse members interference factor (IF), and pullout bearing resistance of a single transverse member P_{b1}. It was found that IF and P_{b1} were primarily controlled by F and w/w_{owc}. The 3-D plot of β versus w/w_{owc} and F in the range of $0.67 \leq w/w_{owc} \leq 1.33$ and $20 < F < 98\%$ are proposed to determine P_{b1}. On the dry side of optimum and at w_{owc}, the β of $\pi/2$ is recommended for $F < 45\%$. On the wet side of optimum, β declines significantly with increasing w/w_{own} and F until $\beta = \pi/3$ at $w/w_{owc} = 1.33$.

3. The 3-D plot of S_2/B versus w/w_{owc} and F in the range of $0.67 \leq w/w_{owc} \leq 1.33$ and $20 < F < 98\%$ are proposed to determine IF. The S_2/B value was essentially the same of 13.3 for $w \leq w_{owc}$, whereas the S_2/B value for $w > w_{owc}$ decreased linearly with increasing water content. Using the relationship between β versus F and w and the relationship between IF versus F and w, P_{bn} can be calculated.

4. The methodology for predicting pullout capacity of bearing reinforcement was proposed in this research. The proposed method is useful for BRE wall design. The development of these generalized pullout resistance predictive equations for the bearing reinforcement are based on sound principle. Further studies can extend the framework to develop pullout resistance predictive equations for other reinforcement systems.

Acknowledgments

Notation

The following symbols are used in this paper:

B = leg length and length of transverse member (m);
c = cohesion of soil (N/m²);
D = diameter of longitudinal member (m);
F = fines content;
IF = transverse member interference factor;
L = length of transverse member (m);
L_e = embedded length of longitudinal member (m);
n = number of transverse members;
OWC = optimum water content;
P_{b1} = bearing pullout force of a single transverse member (N);
P_{bn} = bearing pullout force of n transverse members (N);
$P_{f,peak}$ = peak friction pullout force (N);
$P_{f,residual}$ = residual friction pullout force (N);
S = spacing of transverse members (m);
S_1/B = spacing ratio, dividing the block failure and interference failure zones;

S_2/B = spacing ratio, dividing the interference failure and individual failure zones;
α_p = peak interaction factor;
α_r = residual interaction factor;
β = failure plane angle (radian); and
ϕ = internal friction angle of soil (degrees).

## References

AASHTO. 2002. *Standard specifications for highway bridges.* 17th ed. Washington, DC: AASHTO.

ASTM. 1995. *Test method for laboratory compaction characteristics of soil using standard effort (12,400 ft-lbf/ft³ (600 kN-m/m³)).* ASTM D698-91. West Conshohocken, PA: ASTM.

Bergado, D. T., J. C. Chai, and H. Marui. 1996. "Prediction of pullout resistance and pullout force displacement relationship for inextensible grid reinforcements." *Soils Found.* 36 (4): 11–22. https://doi.org/10.3208/sandf.36.4_11.

Bonaparte, R., and B. R. Christopher. 1987. "Design and construction of reinforced embankments over weak foundations." *Transp. Res. Rec.* 1153 (1): 26–39.

Chai, J. C., N. Miura, and S. L. Shen. 2002. "Performance of embankments with and without reinforcement on soft subsoil." *Can. Geotech. J.* 39 (4): 838–848. https://doi.org/10.1139/t02-033.

Donrak, J., S. Horpibulsuk, A. Arulrajah, H. Kao, A. Chinkulkijniwat, and M. Hoy. 2018. "Wetting-drying cycles durability of cement stabilised marginal lateritic soil/melamine debris blends for pavement applications." *Road Mater. Pavement Des.* https://doi.org/10.1080/14680629.2018.1506816.

Horpibulsuk, S., and A. Niramitkronburee. 2010. "Pullout resistance of bearing reinforcement embedded in sand." *Soils Found.* 50 (2): 215–226. https://doi.org/10.3208/sandf.50.215.

Horpibulsuk, S., C. Suksiripattanapong, A. Niramitkornburee, A. Chinkulkijniwat, and T. Tangsutthinon. 2011. "Performance of earth wall stabilized with bearing reinforcements." *Geotext. Geomembr.* 29 (5): 514–524. https://doi.org/10.1016/j.geotexmem.2011.05.002.

Horpibulsuk, S., A. Udomchai, A. Joongklang, A. Chinkulkijniwat, N. Mavong, A. Suddeepong, and A. Arulrajah. 2016. "Pullout resistance mechanism of bearing reinforcement embedded in residual clayey soils." *Geosynthetics Int.* 24 (3): 255–263.

Jewell, R. A. 1988. "The mechanics of reinforced embankments on soft soils." *Geotext. Geomembr.* 7 (4): 237–273. https://doi.org/10.1016/0266-1144(88)90001-5.

Jewell, R. A., G. W. E. Milligan, R. W. Sarsby, and D. Dubois. 1984. "Interaction between soil and geogrids." In *Proc., Symp. on Polymer Grid Reinforcement in Civil Engineering,* 11–17. London: Thomas Telford.

Jiang, Y., J. Han, R. L. Parsons, and J. J. Brennan. 2016. "Field instrumentation and evaluation of modular-block MSE walls with secondary geogrid layers." *J. Geotech. Geoenviron. Eng.* 142 (12): 05016002. https://doi.org/10.1061/(ASCE)GT.1943-5606.0001573.

Liu, C. N., Y. H. Ho, and J. W. Huang. 2009. "Large scale direct shear tests of soil/PET-yarn geogrid interfaces." *Geotext. Geomembr.* 27 (1): 19–30. https://doi.org/10.1016/j.geotexmem.2008.03.002.

Liu, H. 2012. "Long-term lateral displacement of geosynthetic-reinforced soil segmental retaining walls." *Geotext. Geomembr.* 32 (Jun): 18–27. https://doi.org/10.1016/j.geotexmem.2011.12.001.

Mohamed, S. B. A., K.-H. Yang, and W.-Y. Hung. 2013. "Limit equilibrium analyses of geosynthetic-reinforced two-tiered walls: Calibration from centrifuge tests." *Geotext. Geomembr.* 41 (Nov): 1–16. https://doi.org/10.1016/j.geotexmem.2013.08.004.

Palmeira, E. M. 2004. "Bearing force mobilisation in pull-out tests in geogrids." *Geosynthetics Int.* 22 (6): 481–509.

Perterson, E. M., and L. R. Anderson. 1980. *Pullout resistance of welded wire mats embedded in soil.* Research Rep. Logan, UT: Dept. of Civil and Environmental Engineering, Utah State Univ.

Phummiphan, I., S. Horpibulsuk, T. Phoo-ngernkham, A. Arulrajah, and S. L. Shen. 2016. "Marginal lateritic soil stabilized with calcium carbide residue and fly ash geopolymers as a sustainable pavement base

© ASCE   04019379-8   J. Mater. Civ. Eng.

J. Mater. Civ. Eng., 2020, 32(3): 04019379

material." *J. Mater. Civ. Eng.* 29 (2): 04016195. https://doi.org/10.1061/(ASCE)MT.1943-5533.0001708.

Roodi, G. H., and J. G. Zornberg. 2017. "Stiffness of soil-geosynthetic composite under small displacements. II: Experimental evaluation." *J. Geotech. Geoenviron. Eng.* 143 (10): 04017076. https://doi.org/10.1061/(ASCE)GT.1943-5606.0001769.

Sukmak, K., P. Sukmak, S. Horpibulsuk, A. Chinkulkijniwat, A. Arulrajah, and S. L. Shen. 2016. "Pullout resistance of bearing reinforcement embedded in marginal lateritic soil at molding water contents." *Geotext. Geomembr.* 44 (3): 475–483. https://doi.org/10.1016/j.geotexmem.2015.07.01.

Sukmak, K., P. Sukmak, S. Horpibulsuk, J. Han, S. L. Shen, and A. Arulrajah. 2015. "Effect of fine content on the pullout resistance mechanism of bearing reinforcement embedded in cohesive-frictional soils." *Geotext. Geomembr.* 43: 107–117. https://doi.org/10.1016/j.geotexmem.2014.11.010.

Sukmak, P., S. Horpibulsuk, and S. L. Shen. 2013. "Strength development in clay-fly ash geopolymer." *Constr. Build. Mater.* 40 (Mar): 566–574. https://doi.org/10.1016/j.conbuildmat.2012.11.015.

Suksiripattanapong, C., S. Horpibulsuk, A. Chinkulkijniwat, and J. C. Chai. 2013. "Pullout resistance of bearing reinforcement embedded in coarse-grained soils." *Geotext. Geomembr.* 36 (Feb): 44–54. https://doi.org/10.1016/j.geotexmem.2012.10.008.

Udomchai, A., S. Horpibulsuk, C. Suksiripattanapong, N. Mavong, R. Rachan, and A. Arulrajah. 2017. "Performance of the bearing reinforcement earth wall as a retaining structure in the Mae Moh mine." *Geotext. Geomembr.* 45 (4): 350–360. https://doi.org/10.1016/j.geotexmem.2017.04.007.

Wang, S., D. Chan, and K. C. Lam. 2009. "Experimental study of the effect of fines content on dynamic compaction grouting decomposed granite of Hong Kong." *Constr. Build. Mater.* 23 (3): 1249–1264. https://doi.org/10.1016/j.conbuildmat.2008.08.002.

Zhang, N., S. L. Shen, H. N. Wu, J. C. Chai, and Z. Y. Yin. 2015. "Evaluation of performance of embankments with reinforcement on PVD-improved marine clay." *Geotext. Geomembr.* 43 (6): 506–514. https://doi.org/10.1016/j.geotexmem.2015.05.005.

© ASCE   04019379-9   J. Mater. Civ. Eng.

J. Mater. Civ. Eng., 2020, 32(3): 04019379

BIOGRAPHY

Mr. Artit Udomchai was born on July 31, 1988, in Maha Sarakham province, Thailand. He obtained his bachelor's degree in civil engineering from the Faculty of Engineering and Architecture, Rajamangala University of Technology Isan, in 2011. He was then awarded the One Research One Graduate (OROG) Scholarship from Suranaree University of Technology, in 2011 and obtained his master's degree in Civil Engineering from the School of Civil Engineering, Suranaree University of Technology, in 2014. Subsequently, he has been awarded a Research and Researcher for Industries (RRI) Ph.D. Program Scholarship from the Thailand Research Fund (TRF) and National Research Council of Thailand (NRCT) in 2018 for his Ph.D. study in the School of Civil Engineering, Suranaree University of Technology. During his Ph.D. study (2017-2020), he has worked as a teaching assistant for Surveying, Surveying Laboratory. He also has worked as a researcher assistant for the Center of Excellence in Innovation for Sustainable Infrastructure Development, Suranaree University of Technology (ISI-SUT). He has joined the research under the supervisor of Univ. Prof Arul Arulrajah at Swinburne University of Technology, Melbourne, Australia from 2017-2021. He has published 5 leading international journal papers. His expertise and research filed are in the area of geotechnical failure and finite element analysis.